MAGNETIC-BASED THERANOSTIC NANOPARTICLES FOR PROSTATE CANCER MANAGEMENT

by

ANIKET SHARADRAO WADAJKAR

Presented to the Faculty of the Graduate School of
The University of Texas at Arlington in Partial Fulfillment
of the Requirements
for the Degree of

DOCTOR OF PHILOSOPHY

THE UNIVERSITY OF TEXAS AT ARLINGTON

August 2012

DEDICATION

I dedicate this doctoral dissertation to my beloved family, especially to my wife for her love, patience, understanding, and motivation; to my parents for their love, support, and encouragement for higher education; and to my brothers for their love, motivation, and teaching importance of hard work.

ACKNOWLEDGEMENTS

It is my immense pleasure to finally present my research in the form of a doctoral dissertation. The work presented in the following pages is the outcome of perseverance and consistent effort through years of academic challenges. Earning the doctoral degree is a dream comes true, and it is possible with the help of a number of wonderful and inspiring people who contributed in shaping my educational experience, my career path, and my life. I would like to take this opportunity to thank them all.

I would like to thank Dr. Kytai T. Nguyen, my advisor and mentor, for her continuous support and belief in my abilities, which motivated me to stretch my limits and achieve excellence in research. Her knowledge, commitment, and wisdom to collaborate across the departments and universities have provided me the opportunity to work on a multitude of projects. Her positive attitude and optimism has inspired me to apply and win the American Heart Association Predoctoral Fellowship, which has been one of the most remarkable achievements of my doctoral studies. I deeply appreciate her suggestions, guidance, and patience throughout this work.

I am also grateful to Dr. Jian Yang for being my co-advisor and for guiding my research in the past several years. His insightful criticism and comments on my manuscripts have always sharpened my writing skills. His mentorship has also pushed me to expand the depth and breadth of my knowledge in the area of nanomedicine and biomaterials. I am also thankful to my dissertation committee members and collaborators, Dr. Jer-Tsong Hsieh, Dr. Liping Tang, and Dr. Baohong Yuan for providing their help with the animal studies and for generously sharing advice that facilitated my research to achieve new heights; to Dr. Masaya Takahashi and Dr. Kim Kangasniemi for their help with MRI studies; and to Dr. Yaowu Hao for his thoughtful criticism and guidance on magnetic characterization studies.

I would like to thank my lab mates and mentees, Zarna Bhavsar, Jyothi Menon, and Nikhil Pandey for participating in the research with interest and enthusiasm; and for working diligently to make it a success. In particular, I thank Tejaswi Kadapure and Sonia Santimano for being my two hands, though I could not decide who the right hand was and who the left was. I am also thankful to the students and technicians of our collaborators for their help with animal and ultrasound studies. I could not have done any of this without all my supportive, forgiving, generous, and loving friends, who made me feel at home while I am away from home during my stay in Arlington. In particular, Uday Tata and Dr. Tre Welch with whom I unwound at the end of the day over coffee and conversations. I appreciate Uday’s constant support and inspiration, despite tremendous work pressures we were facing together; and Tre’s friendship that enlightened and entertained me over the many years.

Most importantly, I owe the deepest gratitude to my family. My parents, Mr. and Mrs. Sharad and Smita Wadajkar for loving me unselfishly, for supporting me in all the endeavors of my life, and for instilling the principles and values of humanity in me. I would also like to express my gratitude to my brothers; to Dr. Shailesh Wadajkar for teaching me how to be strong, for his love, support, and constant faith in me during the ups and downs of my life; and to Vishal Wadajkar for his love, for teaching me lessons on how to deal with reality, how to keep perspective when setting life's priorities, and how to be optimistic from his philosophical standpoint. I am also grateful to my in-laws, especially my father in-law, Mr. Ishvarlal Kanakia, and my grandmother for planting in me the roots of spiritualism, which are reflected in my good Karma. Finally, with the deepest love, respect, and affection, I thank my wife, Shruti Kanakia. Nothing can repay her for her love, patience, and understanding throughout my doctoral research. Although the circumstances have forced us to live apart from one another, she still made a point of travelling the journey with me, through all the ups and downs. Without her love, support, and motivation, this dissertation would never have been written.

July 17, 2012

ABSTRACT

MAGNETIC-BASED THERANOSTIC NANOPARTICLES FOR PROSTATE CANCER MANAGEMENT

Aniket Sharadrao Wadajkar, PhD

The University of Texas at Arlington, 2012

Supervising Professors: Kytai T. Nguyen and Jian Yang

With an increasing rate of cancers, the need for effective cancer management has led to the development of theranostic systems for diagnosis and therapy. Conventional techniques for cancer management have limited success due to inaccurate diagnosis and treatment side effects. Development of magnetic-based theranostic nanoparticles (MBTN) may overcome these limitations with the advantages of magnetic nanoparticles (MNPs) such as magnetic targeting, hyperthermia, and magnetic resonance imaging (MRI) contrast agents; and advantages of polymer coatings for carrying payloads and allowing bioconjugation for active targeting applications. Aim of this research was to develop multifunctional MBTNs for prostate cancer management.

First, biodegradable photoluminescent polymers (BPLP)-coated iron oxide MNPs were developed, which were stable, well dispersed, and exhibited both a bright fluorescence in UV light and dark negative contrast in MRI. Moreover, these cytocompatible nanoparticles released most of the therapeutically effective drugs within 21 days. Prostate cancer cells also showed selective uptake of nanoparticles depending on cell type. Finally, the presence of magnetic field reinforced the uptake of nanoparticles as seen from *in vitro* cellular uptake and *in vivo* biodistribution study.

Second, thermo-responsive polymer-coated MNPs (PMNPs) were formulated and conjugated with prostate cancer-specific R11 peptides for active targeting of drugs to prostate cancer cells only. The cytocompatible PMNPs also generated a dark negative contrast in MRI. Moreover, a higher uptake of R11-PMNPs was noticed compared to non-conjugated PMNPs. Preliminary *in vivo* studies showed that R11-PMNPs accumulated more in the tumor compared to non-conjugated PMNPs.

Finally, novel thermo-responsive fluorescent polymer-coated MNPs (TFP-MNPs) were developed by combining the principles from both BPLP-MNPs and PMNPs. Cytocompatible TFP-MNPs possessed temperature-dependent fluorescence and drug release. TFP-MNPs also exhibited a bright fluorescence in the prostate cancer orthotopic mouse model. Preliminary investigation on these nanoparticles (BPLP-MNPs, PMNPs, and TFP-MNPs) *in vivo* and results from *in vitro* studies demonstrated their potential as multifunctional theranostic nanoparticles for various biological applications, including prostate cancer management.

TABLE OF CONTENTS

LIST OF ILLUSTRATIONS

LIST OF TABLES

CHAPTER 1

INTRODUCTION

1.1 Prostate Cancer

According to the American Cancer Society, prostate cancer is still a commonly diagnosed cancer and the second leading cause of cancer-related deaths in men. In the United States (US), prostate cancer will be accountable for 241,740 new cancer cases and 28,170 deaths in 2012 [1]. Common treatments for prostate cancer such as surgery, hormone therapy, radiation therapy, and chemotherapy have mixed results due to the adverse side effects [2]. The complications associated with surgery are pain, urinary incontinence, and the possibility of permanent impotence. The side effects of hormone therapy include loss of sexual desire, impotence, and hot flashes. Further, radiation therapy causes tiredness, diarrhea, uncomfortable urination, and hair loss in the pelvic area. Whereas, side effects of chemotherapy are dependent on the type of drug used. In general, chemotherapy causes systemic toxicity that is responsible for hair loss, weakness, impotence, urinary retention, and erectile dysfunction, leading to poor qualities of lives for prostate cancer patients. In addition, the average cost for a prostate cancer hospitalization is about $8,100, and hospital costs for the treatment of prostate cancer totaled more than $700 million in the US [3]. Alternative therapeutic modalities such as targeted therapy or local delivery of a therapeutic drug to only the tumor regions or cancer cells would be a better alternative treatment to save costs and lives associated with prostate cancer. Moreover, early diagnosis of cancer is critically important to select effective treatment methods, and targeted therapy would reduce the complications associated with chemotherapeutic agents, leading to improving the quality of life for prostate cancer patients.

1.1.1 Prostate Cancer Diagnosis

To detect prostate cancer, the commonly used detection and screening tools are prostate specific antigen (PSA) screening, digital rectal examination (DRE), transrectal ultrasonography (TRUS) and histological examination of biopsied prostate samples [4]. However, these methods have several serious limitations and complications. For instance, about 25% of men with high PSA levels show benign prostatic hyperplasia only and no cancer; whereas a significant number of prostate cancer patients have very low PSA values (< 4 ng/ml) [5]. In addition, DRE and TRUS demonstrate low sensitivity and specificity; thus, the detection is more likely subjective and less accurate [6]. Although the histological examination of biopsied prostate samples is the current gold standard for prostate cancer diagnosis, it has missed more than 30% of cancers [7]. It also consists of other complications such as biopsy-mediated cancer cell dissemination, inflammation of existing infection, decreased ejaculation and impotency after the procedure. The shortcomings associated with current screening methods highlight the need to develop new modalities that improve the detection of prostate cancer, thereby enabling the early diagnosis of prostate cancer.

1.1.2 Prostate Cancer Imaging

To improve the detection of prostate cancer, imaging approaches using intravenously injected targeting contrast reagents for computed tomography (CT), magnetic resonance imaging (MRI), and positron emission tomography (PET) have been studied [8]. For example, superparamagnetic iron oxide nanoparticles have been used as contrast agents in MRI for lymph node prostate cancer imaging [9]. MRI, with the advantages of exceptional tissue contrast and spatial resolution, has been widely used in clinical settings; however, MRI is insensitive for small lesions and quite expensive. On the other hand, PET using 2-deoxy-2[^{18}F]fluoro-D-glucose has been considered a more sensitive imaging technique, but it is still insensitive for small lesions (< 1 cm) [10]. Optical imaging is relatively inexpensive and a highly sensitive and specific imaging modality when molecularly targeted to the tumor [11]; however, its limitations include limited tissue penetration and a significant background signal due to auto-fluorescence of the tissue. Yet optical imaging has the potential to identify tiny deposits of tumors during cytoreductive surgery [12]. Thus, attempts on combining multiple imaging probes are considered beneficial for prostate cancer imaging and treatment. For example, MRI can be used before surgery to identify tumor location, whereas optical imaging can be used during the cytoreductive surgery to enhance the contrast between tumor and normal tissue and to improve the identification of small lesions [13]. These observations suggest that the combination of MRI and optical imaging techniques has the potential to improve the cancer detection, leading to more effective or better treatments for prostate cancer.

1.1.3 Prostate Cancer Treatment

Several studies have investigated the development of drug carriers since powerful chemotherapeutic reagents designed to kill rapidly dividing tumor cells have also taken their toll on normal healthy cells, causing significant side effects including bone marrow suppression, hair loss, and fatigue. For example, doxorubicin, an anticancer drug, exhibits excellent clinical activity in prostate cancer; however, its use is limited because of the systemic toxicities such as immunosuppression and cardiac toxicity [14]. To overcome limitations of systemic chemotherapy, several carriers such as liposomes, dendrimers, and polymeric nanoparticles have been developed to encapsulate anticancer drugs and deliver them to the tumors. The US Food and Drug Administration (FDA) approved drug delivery nanoparticles are liposomal formulations, PEGylated liposomal doxorubicin (Doxil), liposomal daunorubicin (DaunoXome) and albumin bound paclitaxel nanoparticles (Abraxane) [15]. Yet one of the major limitations of these carriers is that it is not possible to monitor the distribution of drugs and the progress of treatment in real time. Since the knowledge of the biodistribution of drug formulations is a key to their successful development for tumor targeting, drug carriers that can also be used as tracers or contrast reagents are needed for the development of effective alternative cancer therapies. The technical challenges in developing effective nanoparticle systems for cancer detection and treatment are: 1) eliminating the long-term toxicity concerns, 2) achieving high sensitivity and specificity, 3) reaching adequate concentrations of nanoparticles locally, and 4) possessing both imaging agents and therapeutic agents for diagnosis and therapy, respectively, in a single setting. To meet these challenges many researchers are trying to develop metal and polymer-based ‘theranostic’ nanoparticles that have capabilities of cancer diagnosis and treatment.

1.2 Theranostic Nanoparticles

Theranostic nanoparticles that simultaneously deliver both imaging and therapeutic agents have gained significant attention for cancer management in recent years. Cancer management not only includes the highly specific diagnosis and treatment of the cancer cells, but also the monitoring of the drug delivery process and therapeutic efficacy [16]. Conventional nanoparticle systems have been previously used to achieve each aspect of cancer management separately; however, multiple administrations may be required to fulfill all the necessary functions, which bring concerns of patient compliance and safety [17]. To overcome these limitations, theranostic nanoparticle systems that can perform all the aspects of cancer management in a single setting have been developed over the last decade. In particular, magnetic-based theranostic nanoparticles (MBTN) are of great interest in cancer management due to the numerous advantages these materials possess in the presence of a magnetic field, which is summarized in Figure 1.1. Magnetic nanoparticles (MNPs) are multifunctional agents that can be used: 1) for site-specific magnetic targeting [18], 2) as negative contrast agents in MRI [19], 3) for hyperthermia treatment under alternating magnetic fields [20], and 4) in magnetic field-dependent controlled drug delivery applications [18] collectively, rendering MNPs as ideal candidates in the development of advanced theranostic systems.

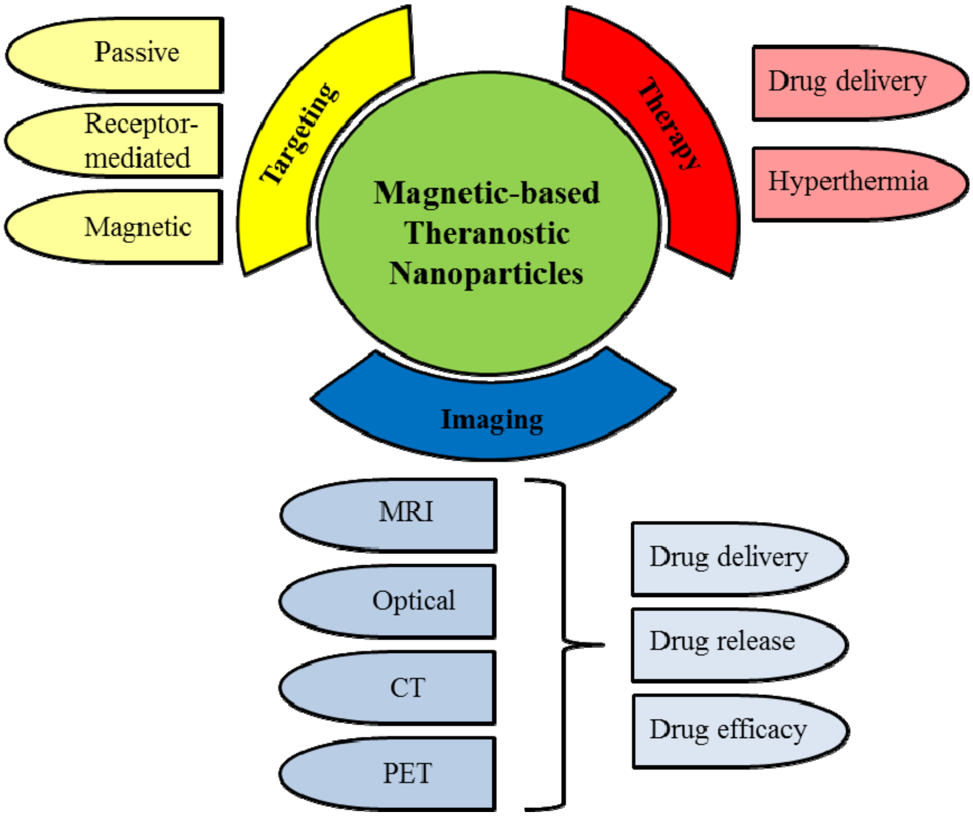

Figure 1.1 Attributes and applications of MBTN in cancer targeting, imaging, and treatment.

1.2.1 MNPs

MNPs are one of the most popular theranostic agents in the field of nanomedicine for targeted and controlled drug delivery. Although the research on MNPs began in the early 19th century, it’s only recently that there has been an increasing interest in MNPs as theranostic agents, due to their therapeutic and diagnostic application potentials [18]. MNPs are composed of ferromagnetic elements such as iron, cobalt, nickel, or their oxides and alloys [21]. MNPs made of iron oxide (magnetite Fe_3O_4 or magnemite Fe_2O_3) and gadolinium (chelated organic gadolinium complexes) [22] have been widely used as contrast agents in MRI for biological applications due to their ability to dissociate into iron and oxygen inside the body, which can safely be eliminated and utilized in metabolic and oxygen transport systems [23]. When fabricated into nanoparticles of approximately 10 nm in diameter, iron oxide nanoparticles begin to exhibit a superparamagnetic behavior leading to improved dispersive properties in the absence of a magnetic field. They can also be guided to accumulate to the site of interest in the presence of a magnetic field, which is of great importance in targeted drug delivery applications [19]. In addition, MNPs possess low cytotoxicity and have been approved by the FDA for clinical MRI applications [23, 24]. Numerous studies have explored the potential of MNPs as therapeutic and diagnostic agents for the cancer management. Recent years have seen an increasing interest in the study of polymers that can be used for coating MNPs.

1.2.2 Polymer Coatings

Recent research has been intensely focused on finding suitable biodegradable and biocompatible polymers that can efficiently be incorporated with drugs, imaging agents such as MRI contrast reagents, and biomolecules for active targeting of the cancer [22]. Hydrophilic natural and synthetic polymers have been used as coating materials due to their ability to prevent particle aggregation, increase solubilization, and improve stability of the particles [16]. Natural polymers such as dextran are gaining prominence in the field since MNPs coated with these polymers have shown improved biocompatibility and tend to stay in circulation for relatively longer periods of time [20]. FDA approved dextran-coated MNPs have already been used to image spleen, liver, and lymph nodes [16]. For instance, dextran-coated MNPs prepared by Tassa et al. [25] imparted both stability and additional functional groups for bioconjugation on the nanoparticle surface. The dextran coating also supported diagnostic imaging of the nanoparticles by MRI, PET and optical imaging. Moreover, chitosan is another natural material gaining importance as a suitable coating for MNPs due to its biocompatibility and the added functional groups, which can be utilized for bioconjugation [26]. However, natural polymers generally have low mechanical strength, low porosity, and non-selective protein adsorption on their surfaces [27].

In addition to natural materials, MNPs have also been coated with synthetic biodegradable or non-degradable polymers including poly(lactic-co-glycolic acid) (PLGA) [28] and poly(*N*-isopropylacrylamide) (PNIPAAm) [29]. PLGA has been widely chosen to coat MNPs by many research groups due to its biocompatibility and ability to provide the sustained release of encapsulated drugs or contrast agents throughout the polymer degradation time to ensure prolonged treatment. For example, PLGA-magnetite particles prepared by Chattopadhyay et al. [28] showed sustained drug release for a prolonged period and could also be used for MRI and drug delivery applications. In contract to biodegradable polymers, many synthetic non-degradable polymers persist in the body after administration; therefore, they are generally not preferred for coating of MNPs.

Besides biodegradable polymers for controlled drug delivery applications, stimuli responsive polymers have been studied extensively due to their ability to respond to external stimuli such as pH, temperature, light, salt concentration, mechanical stress, and electric field [30]. Several joint interactions within the polymer, such as gradual ionization or breakage of hydrogen bonds, result in phase transition of the polymer in response to the changes of stimuli. One of the most commonly studied stimuli-responsive polymers is PNIPAAm [31], which enables drug release when the temperature of the solution is raised above the lower critical solution temperature (LCST, ~ 32^{o}C) of the polymers. The LCST of a polymer can be modified by co-polymerization with hydrophilic or hydrophobic monomers or by the addition of more salts to the polymer solution. For example, copolymerization of PNIPAAm with hydrophilic acrylamide increases the LCST, while copolymerization with hydrophobic n-butyl acrylamide decreases the LCST [32]. PNIPAAm copolymerized with acrylamide (AAm) and allylamine (AH) were developed previously in our laboratory to decorate MNPs [29]. The PNIPAAm-AAm-AH decorated MNPs shrink and release the encapsulated drugs in response to an increase in the surrounding temperature (~39^{o}C or above). Combinations of smart polymers, such as temperature-sensitive PNIPAAm and pH-sensitive chitosan, have also been used to formulate dual-responsive nanoparticles with combined properties from both polymers [33]. As a result, these nanoparticles were shown to release the encapsulated drugs both at temperatures above the LCST and in an acidic environment, which are respectively beneficial attributes for cancer treatment since the tumor environment is characterized by higher temperature and lower pH (< 7.2) when compared to healthy tissues [34].

In order to treat multi-drug resistant tumors, multiple drug loading strategies have been developed using magnetic-based nanoparticles such as magnetic liposomes. The bilayered geometry of magnetic liposomes allows for the encapsulation of multiple therapeutic agents for multi-drug delivery [35]. For instance, hydrophilic drugs are incorporated in the hydrophilic core of the liposome, whereas hydrophobic drugs are loaded in the lipid bilayer of the liposome and amphiphilic molecules can be incorporated at the hydrophilic/hydrophobic interface of the liposome [36]. Amphiphilic poly(2,2,3,4,4,4-hexafluorobutyl methacrylate)-g-PEG monomethacrylate has also been used to prepare magnetic micelles of ~100 nm diameter mainly for diagnosis of liver and spleen diseases. These nanoparticles showed high stability in water for up to 16 days and maintained sustained release of 5-fluorouracil for 40 hours [37]. While polymer coatings play an important role in drug delivery and release kinetics, they also provide valuable functional groups for bioconjugation, which can be utilized to provide targeting moieties for MBTN.

1.2.3 MBTN Structure Types

Surface coating of MNPs using various polymers is an inevitable synthesis process for various applications in nanomedicine and drug delivery field. The surface coating not only reduces particle agglomeration and cytotoxicity, but also increases

MNP circulation time and induces a payload of therapeutic agents to the target site. Depending on the material and synthesis method, polymer coatings on MNPs give rise to various structural designs of nanoparticles (Figure 1.2). Core-shell structures are the most popular nanoparticle designs for biomedical applications (Figure 1.2A), which are mostly comprised of MNPs as a core and materials such as silica and gold as a shell. Biocompatible silica/gold-coated MNPs have attracted attention as MRI contrast agents and magnetic carriers for imaging and therapeutic applications, respectively [38].

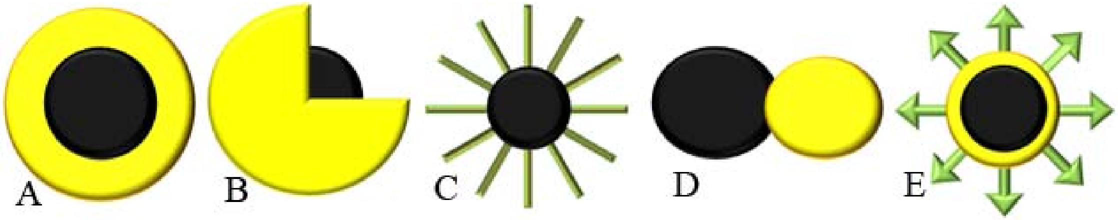

Figure 1.2 MBTN structure types. (A) Core-shell structure, (B) MNPs encapsulated in polymer layers, (C) end-grafted polymer segments on MNPs, (D) heterodimer MNPs, and (E) functional ligands conjugated MNPs.

Commonly used strategies for making polymer-embedded MNPs are: 1) synthesizing MNPs in the presence of a polymer, 2) synthesizing a polymer in the presence of MNPs, or 3) mixing MNPs with polymer solution [39]. These synthesis strategies create two different nanoparticle structures: 1) encapsulated MNPs in polymer layers (Figure 1.2B) and 2) end-grafted polymer segments on MNPs (Figure 1.2C) [40]. Preparation of these structures is easy and quick; however, it might be a disadvantage as MNPs are not tightly held inside the polymer layers, and they may slip off the structure under higher shear forces or blood flow rates. Polymers such as dextran, chitosan, and

PLGA have been used for making polymer-embedded MNPs for MRI and drug delivery applications [41-43]. The second types of structure, where the polymer segments are end-grafted on the surface of MNPs, are very strong because polymer chains are covalently attached to the MNP surface. The MNPs in the polymer segments are stable and well protected from the environment [31]. Polymers such as PNIPAAm and PEG have been used for end grafting on MNPs for MRI and drug delivery [44, 45].

Heterodimers or dumbbell-like structures possess bi-functionality due to the presence of two different functional molecules in the structure (Figure 1.2D). They have shown great potential for target specific imaging and delivery applications. For instance, silver-MNPs and gold-MNPs have been developed with optical and magnetic properties for imaging and hyperthermia applications [46]. Finally, surface modification and linking functional ligands to MNPs is a popular technique to provide functionality to the MNPs for targeting/specific applications. Various types of ligands such as targeting moieties, permeation enhancers, organic dyes, fluorophores, and therapeutic agents can be attached on the MNP surface via bioconjugation chemistry techniques utilizing protein coupling agents, avidin–biotin, hetero-bi-functional linkers, carbodiimide chemistry, and click chemistry [40]. Many researchers have conjugated or incorporated FITC, rhodamine, near-infrared fluorescent dyes, or quantum dots (QDs) for cell labeling, tracking, and imaging applications [47, 48]. Moreover, several researchers have conjugated proteins, antibodies, aptamers, and other molecules to MNPs for targeted delivery of drugs and gene therapy [49, 50].

1.2.4 Targeting Mechanisms

A critical component in achieving an effective drug delivery and imaging tool is the ability to specifically target the diseased site and bypass healthy tissues. Targeting strategies for MBTN are met by various challenges such as selecting the appropriate target, methods to incorporate the specific targeting ligand, and strategies to avoid rapid clearance of the delivery vehicles from the body [51]. The two basic mechanisms of targeting diseases are passive and active targeting, which is summarized in Figure 1.3.

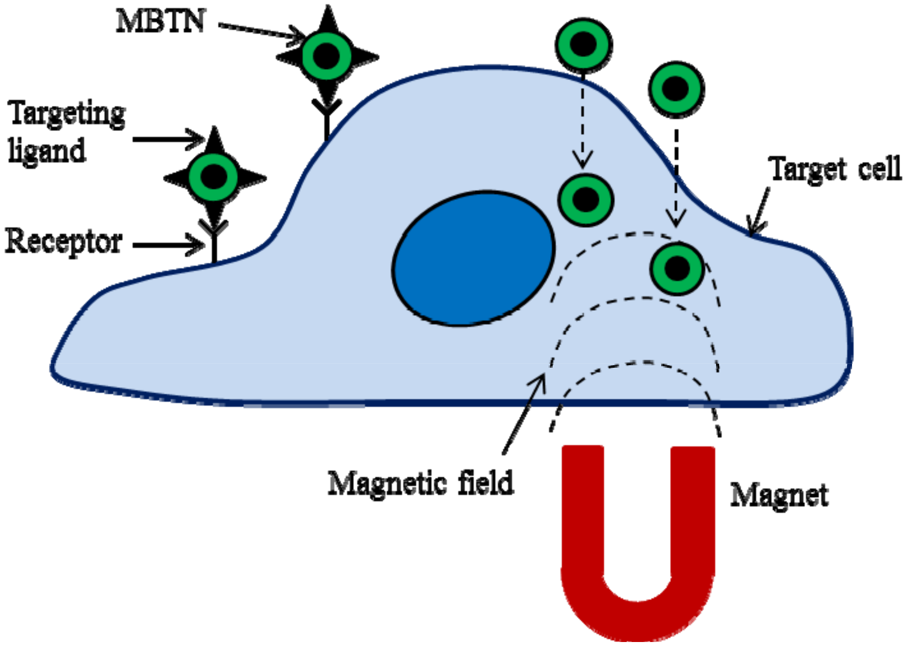

Figure 1.3 Targeting mechanisms of MBTN emphasizing on receptor-mediated and magnetic targeting.

Passive targeting is neither associated with the conjugation of antibodies nor influenced by any external forces. Instead, accumulation of the theranostic vehicle within the tumor site is accomplished by the enhanced permeability and retention (EPR) effect of tumor neovascularization [52]. The highly cluttered vasculature of the tumor tissue leads to a disorganized vasculature, and a defective lymphatic system [53]. When this occurs, nanoparticles in the range of 10 to 500 nm in diameter with hydrophilic surfaces have shown enhanced accumulation within the interstitial space of the tumor [40]. Hydrophilicity is an important factor as it not only increases the circulation time of nanoparticle, but also prevents nanoparticle from being cleared by macrophages and plasma protein adsorption [51]. Passive targeting was employed by Yu et al. [54] using doxorubicin-loaded thermally crosslinked MNPs for cancer treatment and imaging. They observed an increased nanoparticle circulation time and preferential accumulation in the tumor region by the EPR effect in an orthotopic mouse model of lung cancer. Further, dextran-coated MNPs have been used for passive targeting of cancer cells in the human bladder [55]. However, these nanoparticles tend to be removed easily by the reticulo-endothelial system (RES). Although nanoparticles can be used for drug delivery via passive targeting, this process can be both time-consuming and less effective due to their accumulation in other healthy organs in addition to tumor regions [56]. Therefore, alternative and more specific routes of tumor targeting are greatly needed.

Unlike passive targeting, active targeting involves either the conjugation of targeting ligands to nanoparticles or the use of external forces to guide the therapeutic vehicle to the tumor [52]. A wide range of targeting moieties such as hormones, growth factors, proteins, peptides, or monoclonal and polyclonal antibodies have been used to direct MNPs to tumors. The choice of the targeting moiety is of great importance as it should be specific to the receptors over-expressed on the targeted cells. Such ligand-conjugated nanoparticles are engulfed by the receptor-mediated endocytosis process and destroyed intracellularly to release their therapeutic payload [57]. The receptor-mediated targeting is also useful for finding and destroying circulating or metastatic cells that express the receptors of interest [58]. Yao et al. [59] successfully conjugated A10 aptamers to thermally crosslinked MNPs to target prostate specific membrane antigens (PSMA) over-expressed by the prostate cancer cells. They also observed that in media containing physiologic levels of folate, PSMA expression increased folic acid uptake approximately 2-fold over non-expressing cells. Further, Kievit et al. [60] has developed multifunctional MNPs tagged with HER2/neu antibody, which successfully bound to neu-expressing mammary carcinoma cells in mice. These MNPs could also specifically bind to metastatic cells in lung, liver, and bone marrow, thus demonstrating their potential in diagnosis and treatment of metastasized cancer.

In addition to receptor-mediated targeting, active targeting by the use of external forces, such as magnetic fields, has been investigated. Magnetic targeting involves the delivery of MNP locally by guiding them to the diseased site using an external magnetic field. Iron oxide nanoparticles become magnetized upon application of a magnetic field, and are quickly demagnetized when the magnetic field is removed due to superparamagnetic behavior [19]. Magnetic targeting is advantageous and more effective than passive targeting as rapid clearance of nanoparticles by mononuclear macrophages can be avoided [61]. An example for magnetic targeting includes the research developed by Alexious et al. [62], which demonstrated the recruitment of

MNPs in the region of squamous cell carcinoma created in rabbits by using an external magnetic field of strength 1.7 T. Another study conducted by Chertok et al. [63] imaged brain tumors non-invasively with MRI by concentrating MNPs at the tumor site by locally applying an external magnetic field of about 4 T.

Finally, biomaterial-mediated targeting takes advantage of physical and chemical properties of biomaterials for cell-specific targeting or uptake. The physiochemical properties that affect the cell-selective targeting include molecular weight, base polymer composition, surface charge, hydrophilicity/hydrophobicity level, and end-grafting/modification [64]. Moreover, biomaterial-mediated targeting is also dependent on the cell type, cell surface antigen, cell-biomaterial interaction, and so on. Some of the researchers are investigating the effects of biomaterial properties on different cell populations to understand the cell specificity of biomaterial-mediated targeting. For an instance, the Green group at Johns Hopkins University has shown that the biomaterial properties affect cell transfection and cancer cell-specific uptake of DNA-loaded polymeric nanoparticles significantly [64, 65]. Further, combinational targeting can also be achieved by using targeting ligands-conjugated MNPs and an external magnetic field for improved targeting abilities [66]. After effective targeting using MBTN, imaging of the delivery vehicles to highlight the diseased sites could be accomplished.

1.2.5 Imaging Agents

Imaging agents in theranostic nanomedicine play an important role in the diagnosis of a disease [19]. The primary imaging agent used in the MBTN is iron oxide as it has been widely used as T2 negative contrast agents in MRI. Several iron oxide-based nanoparticles were approved by the FDA for human use [67]. Examples include Feridex for liver lesions, Combidex for imaging of ‘hidden’ prostate cancer lymph node metastases and Feraheme for treating iron deficiency anemia in chronic kidney diseases [24]. Further, manganese (Mn) and gadolinium (Gd)-based MRI contrast agents, such as multifunctional MnO and PEG functionalized Gd_2O_3 nanoparticles [68, 69], have also been researched for *in vitro* and *in vivo* imaging applications and further approved by the FDA for human use. Gd-diethylenetriaminepentaacetic acid (Gd-DTPA) complexes with anti-fibrin antibodies have been utilized for MRI, which proved the capability of these nanoparticles to enhance the MRI signal contrast over the clot surface [70].

Contrast agents for optical imaging, PET or CT, have also been incorporated in MBTN to provide multi-modality imaging capabilities for enhanced and more accurate imaging of diseases as summarized in Figure 1.4. A multi-modality imaging approach has several advantages over a single modality system [71]. MRI provides exceptional tissue contrast, penetration depth, and high spatial resolution, whereas fluorescence imaging provides extremely high sensitivity and can be used for molecular imaging [51]. The most popular example of fluorescent agents used in optical imaging is metal semiconductor QDs. QDs have remarkable optical properties compared to other fluorescent dyes [72]. QDs can emit light in the spectrum ranging from visible to near-infrared region, depending on their size or material composition like CdSe, ZnS, and PbSe [51]. When QDs are used with MNPs, they are also called magnetic QDs, which can be either heterodimers or homogeneous dispersion of QDs within MBTN [73]. Polyethyleneimine-capped QD were grafted on magnetite nanorings to develop magneto-fluorescent nanoprobes by Fan et al [74]. In addition, Koole et al. [75] synthesized Gd-based lipid-coated silica nanoparticles with QD core as a new contrast agent platform for multimodality imaging. Moreover, fluorophores such as Alexa Fluor 647 have also been used along with MNPs for the applications in MRI and fluorescent imaging. PET isotopes such as ^{18}F or ^{64}Cu and fluorescent dye VT680 have also been conjugated or encapsulated into the MBTN using click chemistry to enhance the sensitivity and reduce the dose required for clinical use [76].

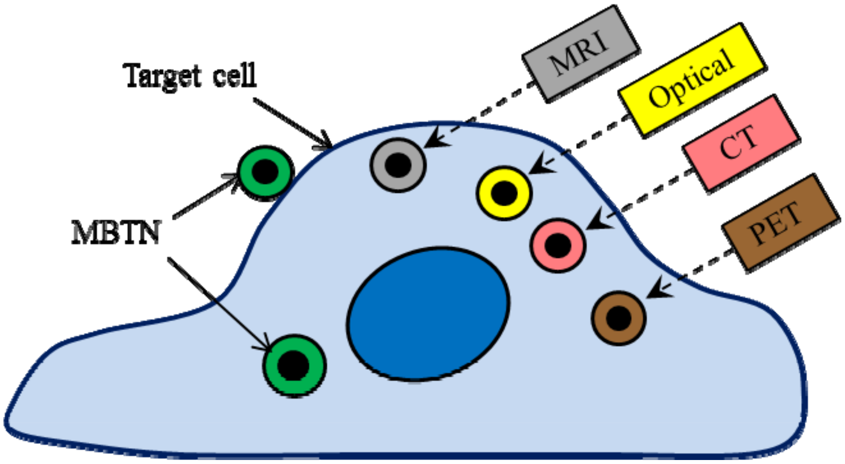

Figure 1.4 Single or multi-modal imaging techniques used for MBTN.

1.2.6 Therapeutic Agents

Following diagnosis, a pivotal role of the MBTN is to treat the cancer by either hyperthermia via alternating magnetic fields or releasing therapeutic agents as shown in Figure 1.5. MBTN can be used without therapeutic agents to kill the heat-susceptible cancer cells by providing heat to the tumor region [20]. This is achieved by applying an external rotating or alternating magnetic field following the nanoparticle injection, which causes the MNPs to vibrate and generate heat to ultimately destroys the cancer cells [77]. In addition, MBTN have been used to deliver a wide variety of therapeutic agents ranging from chemotherapeutic drugs to peptides and genes [78]. Chemotherapeutic agents are more frequently loaded into the MBTN for the treatment of various tumors. For example, anticancer drug doxorubicin was loaded in liposomal nanoparticles containing dextran-coated MNPs as magneto-fluorescent agents for cancer chemotherapy [79]. Other drugs used to date in the MBTN formulations include docetaxel, epirubicin, mitoxantrone, taxol , gemcitabine, and Cisplatin [80, 81].

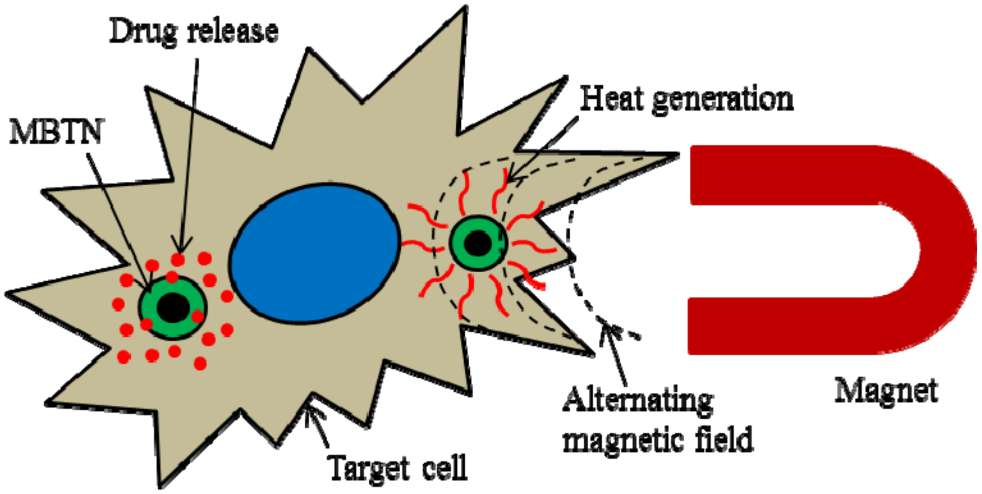

Figure 1.5 Therapeutic action of MBTN showing drug release and hyperthermia treatment.

Besides chemotherapeutic reagents, MBTN have also been used to deliver bioactive molecules including double-stranded DNA (dsDNA), small interfering RNA (siRNA), and proteins. For instance, the MBTN containing both dsDNA and covalently bonded doxorubicin molecules have been prepared for cancer treatment [82]. Such nanoparticles can be used as effective DNA carriers for the transfection of cells and also as agents for vaccination [83]. For gene delivery, stable lentiviral complexes were developed by Mykhaylyk et al. [84] using polyethylenimine (PEI)-capped silica-iron oxide nanoparticles. Moreover, hollow manganese oxide nanoparticles prepared by Bae et al. [68] were surface functionalized using 3,4-dihydroxy-L-phenylalanine and incorporated therapeutic siRNA for simultaneous cancer diagnosis and treatment. In addition, Chertok et al. [85] synthesized β-Galactosidase-loaded heparin-coated MNPs for MRI and protein delivery to diagnose and treat brain tumors. The permeability to biological membranes imparted by the PEI-modified protein, together with magnetic targeting, help in selective accumulation of the nanoparticles at the tumor site.

1.2.7 Controlled Drug Release Mechanisms

Once the nanoparticles are targeted and uptaken by the cells, drugs have to be released from the nanoparticle system for therapeutic effects. The release mechanism of drugs is dependent on the nanoparticle design, properties of the polymer, and surrounding biological parameters such as pH, temperature, ionic strength, and so on. Intracellular drug release is endosomal due to the action of parameters in surrounding cytoplasm. The endosomal drug release can be achieved by various strategies including tailoring of cleavable linkers responsive to pH, temperature, osmolarity, or enzymatic activity [86]. Further, in the drug release via degradation process, the drug is released due to partial or entire degradation of the drug carriers. Degradation mechanism and rate are dependent on the type of polymer [40]. Drug release can be controlled by tailoring polymer coating thickness and degradation rate. Further, sustained release of drugs is mostly controlled by diffusion process. Non-degradable polymers are the choice of interest for designing systems with sustained release of drugs. The drug release rate is affected by the drug solubility, ionic interactions between the drug molecules, and auxiliary ingredients [87]. Finally, a stimuli-controlled drug release is achieved by using stimuli-responsive polymer coatings [44]. The response of these polymers to changes in stimuli is followed by changes in drug release. For example, anticancer drug loaded PNIPAAm and its copolymers have been coated on the surface of silanized MNPs by our group for controlled drug release in responding to changes in temperature [44].

1.3 Applications of MBTNs in Cancer Management

MNPs have been used in numerous applications, which can be categorized in three major fields: 1) imaging (contrast agents for MRI), 2) therapy (chemotherapy via controlled drug release and hyperthermia via heat generation in alternating magnetic fields), and 3) cell separation (cell labeling/tracking and isolation using magnetic force). This research work is focused on the applications of MNPs in imaging and therapy.

1.3.1 Cancer Imaging

With imaging, it is possible to determine if the treatment should be altered or terminated depending on the treatment efficacy [51]. Contrast agents serve as a powerful tool for characterization at the cellular and sub-cellular level. MNPs are used as negative contrast agents in MRI. MNPs such as Fe_3O_4, Gd, and Mn have high molar T2 relaxavities [88]. High spatial resolution of MRI, enhanced negative contrast provided by MNPs, and target specificity of MBTN allow the imaging of tumors as small as 2-3 mm in clinical applications [35]. Branca et al. [89] detected pulmonary micro-metastases with the help of luteinizing hormone-releasing, hormone-conjugated MNPs and MRI in mice bearing breast adenocarcinoma cells. Further, MBTN that have gained significant clinical attention, are iron oxide nanoparticles coated with either dextran or liposomes. Clinical studies on prostate cancer patients by Harisinghani et al.

[90] using lymphotropic MNPs, showed that the lymph node metastases could be accurately identified by high-resolution MRI of the MNPs. A combination of MRI and fluorescence imaging was successfully achieved by Lee et al. [16] for the diagnosis of prostate cancer. Use of QDs and other fluorescent tags along with iron oxide has become a common multi-modal technique.

1.3.2 Cancer Treatment

1.3.2.1 Chemotherapy

Traditional chemotherapies have always shown undesirable side effects on cancer patients due to systemic toxicity of anticancer drugs. As discussed before, a targeted drug delivery can be achieved using MNPs and an external magnetic field. MNPs play an important role in distributing and targeting chemotherapeutic agents to cancer cells, reducing their toxic effects on healthy tissues. The chemotherapeutic drugs are either coated onto MNPs or loaded into the polymer shell. After the administration of drug-loaded MNPs into the living system, an external magnetic field is applied to concentrate the particles at the tumor site. Upon internalization of particles by cancer cells, the drug release is achieved via one of the mechanisms discussed in earlier sections. In the late 1970s, Widder et al. [91] used adriamycin-magnetic albumin microspheres in animal tumor models and observed that these microspheres were significantly more efficient than adriamycin alone in reducing tumor volume and increasing animal survival rate. After these studies, many researchers utilized the potential of MNPs for targeted chemotherapy. For instance, Yu et al. [54] developed doxorubicin-loaded thermally crosslinked MNPs that were administered intravenously into the tumor bearing mice to study the multi-functionality of the particles. The nanoparticles preferentially accumulated in the tumor region within 4.5 hours and showed their therapeutic effect within 12 hours of administration. A significant decrease in tumor size was also noticed within 19 days of the treatment.

1.3.2.2 Hyperthermia

Hyperthermia is a treatment in which high temperatures (> 41°C) are applied to kill cancer cells as they are more sensitive to high temperatures than healthy cells [20]. The metallic and magnetic properties of MNPs make them suitable for hyperthermia treatment [92]. Upon administration and targeting of MBTN to cancer site, an alternating magnetic field can be applied, in which MNPs vibrate and generate thermal energy as a result of absorption of large amounts of magnetic energy by hysteresis loss [20]. Heat generated from the MNPs is affected by several factors, such as magnetic properties, particle size, amplitude and frequency of applied magnetic field, and cooling rate of blood [93]. Thus, by regulating these factors, the heat generation from MNPs can be controlled. However, an optimal hyperthermia effect can be achieved with 10 kA/m amplitude and 400 kHz frequency [20, 93]. In the 1990s, Jordan et al. [94] found the strong heating properties of MNPs and their potential for hyperthermia treatment. Later, Le Renard et al. [95] formulated and implanted poloxamer, chitosan, alginate, and PVA hydrogels loaded with MNPs into human cancer tumors xenografted in mice for hyperthermia treatment. In another study, Tseng et al. [96] used MNPs for hyperthermia treatment and found that the survival rate of cancer cells was significantly reduced when heated above 45°C.

1.3.2.3 Combinational Therapy

Hyperthermia is usually used in conjunction with chemotherapy or radiation therapy to enhance the effectiveness of cancer therapy. At high temperatures, cancer cells become more vulnerable and respond to chemotherapeutic drugs or radiation effectively in an accelerated fashion [20]. Therefore, the combination of two therapies such as hyperthermia and chemotherapy or hyperthermia and radiation therapy would result in better treatment efficacies. For example, Wang et al. [97] synthesized MNPs encapsulated As_2O_3 nanoparticles for treating nude mice bearing xenograft human hepatocarcinoma with both thermal- and chemo-therapies. The combined therapy showed a significant inhibitory effect on the mass and volume of xenograft cervical tumors compared with the controls [98].

1.4 Overview of Research Project

1.4.1 Goal/Objectives

The long term goal of this research project is to develop effective theranostic nanoparticle designs based on polymer-iron oxide complexes for prostate cancer imaging and treatment. Recently, targeted drug delivery via either physical or active targeting strategies have been shown to induce the recruitment of drug carriers at the cancer site effectively, thereby enhancing cancer specificity and reducing severe side effects of chemotherapeutic agents on normal/healthy cells. Medical imaging modalities such as MRI and optical imaging have also demonstrated their effective uses in monitoring of cancer progress during the treatment course, thereby increasing detection and therapeutic efficiency. Targeted imaging modalities and local delivery of therapeutic drugs to only the tumor regions would be the better alternative techniques to save costs and lives associated with prostate cancer. Therefore, the objective of this research was to develop various MBTNs with dual-targeting, dual-imaging, and dual-treatment capabilities to provide better tools/strategies for targeted and controlled release of drugs to the prostate cancer.

1.4.2. Specific Aims

To achieve the research goal, the specific aims proposed for this research are:

Aim 1: Develop theranostic biodegradable photoluminescent polymer-coated MNPs. Nanoparticles were characterized for their physicochemical properties and targeting, imaging and therapeutic efficacies.

Aim 2: Develop theranostic thermo-responsive polymer-coated MNPs. Prostate cancer specific targeting ligand-conjugated nanoparticles were evaluated for their targeting, imaging and therapeutic efficacies.

Aim 3: Develop novel thermo-responsive fluorescent polymer-coated MNPs to combine functionalities of previous designs. A copolymer of fluorescent polymer and thermo-responsive polymer was synthesized and coated on the surface of MNPs. The novel theranostic nanoparticles were characterized for physicochemical and imaging properties.

1.4.3 Innovative Aspects

There are several innovative aspects involved in all the three aims of this research work, which are listed below.

1) The development of novel biodegradable photoluminescent polymer-coated MNPs overcome the drawbacks of long-term toxicity of QDs and poor photostability of organic dyes. The nanoparticles itself are highly cancer cell-selective without the use of any targeting ligands. Moreover, the development of nanoparticles with targeting, imaging, and drug delivery capabilities to allow simultaneous diagnosis and treatment of prostate cancer in a single setting is highly innovative.

2) The combined use of magnetic targeting, thermo-responsive drug delivery, and cancer cell-specific ligands (R11 peptides) will open a new route for targeted drug delivery. Use of R11 peptides for cancer targeting is also highly innovative.

3) Development of the new polymers, which are based on the first two multifunctional designs, is highly innovative. The polymer is biodegradable, thermo-responsive and fluorescent. Coating such multifunctional polymers on the surface of MNPs creates novel theranostic designs with more functionality such as temperature-dependent fluorescence.

1.4.4 Successful Outcome

The successful outcome of this project will provide a means to effectively target, image and treat the prostate cancer in order to reduce complications associated with conventional techniques. In addition, it will reduce the clinical costs, save many lives and improve the quality of life for prostate cancer patients. The knowledge gained from these studies should also advance our understanding of polymer-coated MNPs for cancer management.

CHAPTER 2

BIODEGRADABLE PHOTOLUMINESCENT POLYMER-COATED MNPs

2.1 Introduction

Photoluminescent polymer-coated MNPs act as theranostic systems that deliver both imaging and therapeutic agents so that both diagnosis and treatment of the disease is possible in a single setting. Common diagnostic modalities such as MRI, CT, PET, and optical imaging have mixed results as a stand-alone system due to individual limitations such as low sensitivity, low spatial resolution, toxicity of contrast agents, and inaccurate diagnosis due to non-specific targeting of contrast agents [99]. Dual-/multi-modal imaging systems bearing the advantages from each individual imaging modality may overcome the limitations associated with the stand-alone systems [71]. For instance, MRI provides exceptional tissue contrast, penetration depth, and high spatial resolution, whereas fluorescence imaging provides extremely high sensitivity. Therefore, a dual-imaging modality combining MRI contrast and fluorescent agents will be able to diagnose cancers in early stage pre-operatively and intra-operatively with better accuracy.

To improve the diagnostic accuracy and reduce the significant side effects to normal healthy cells, site-specific targeting of imaging contrast and therapeutic agents is required [14]. Although passive delivery of nanoparticles through leaky tumor vasculature shows some success, active targeting strategies will add more specificity for cancer targeting [100]. Cell-selective nanoparticles specifically target and deliver the payloads to cancer cells, minimizing the side effects due to the non-specific delivery of payloads to healthy cells. Research on the development of cancer targeting nanoparticle systems has been focused mainly on conjugating antibodies, peptides, or aptamers for actively transporting nanoparticles to cancer cells. Other targeting strategies include magnetic targeting that aids in the nanoparticle accumulation at the targeted site under an influence of a magnetic field [40]. Herein, we developed dual-imaging enabled cancer-targeting nanoparticles (DICT-NPs), without using targeting ligands, based on a breakthrough development of biodegradable photoluminescent polymers [101] and superparamagnetic iron oxide (Fe_3O_4) nanoparticles.

Dual-imaging nanoparticles have gained significant attention in recent years. Examples include rhodamine/FITC-labeled paramagnetic nanoparticles [102], DiI/DiR-polyacrylic acid-coated MNPs [103], QD-coated MNPs [104], and Cy5.5-labeled PEG/chitosan-coated MNPs [105]. However, the fluorescent tags used in these systems are known to either be toxic or display photobleaching. Moreover, incorporating imaging agents in nanoparticles may result in increased particle sizes, added complexity, and higher risk of adverse biological reactions. We have recently developed water-soluble and water-insoluble biodegradable photoluminescent polymers (WBPLP and BPLP, respectively), which do not contain photobleaching organic dyes and cytotoxic QDs [101]. The degradability of the polymers and the superior photoluminescent properties such as high quantum yield, photobleaching resistance, and tunable emission up to near infrared area, makes them unique. BPLPs have demonstrated excellent biocompatibility and great potential for imaging both *in vitro* and *in vivo* [101].

Taken together, the aim of this work is to develop DICT-NPs with magnetic targeting capabilities. The rationales behind WBPLP-conjugated MNPs (WBPLP-MNPs) and BPLP-conjugated MNPs (BPLP-MNPs) are that: 1) DICT-NPs provide dual-imaging capability, through which WBPLP/BPLP enables fluorescence imaging while MNPs serve as negative contrast agents for MRI; 2) DICT-NPs could also provide dual-targeting capability, through magnetic targeting and receptor-mediated targeting if active targeting ligands such as antibodies are conjugated; 3) DICT-NPs are fully degradable, thus eliminating long-term toxicity concerns. We have demonstrated the degradability and biocompatibility of BPLP both *in vitro* and *in vivo* [101]. Degradable biocompatible DICT-NPs would address the particle sizes and *in vivo* clearance concerns in the traditional design of tumor-targeting nanoparticles using non-degradable materials where the diameter of nanoparticles should be limited to ~5.5 nm for rapid renal excretion [106]. 4) DICT-NPs act as a drug carrier for controlled drug delivery for many polymer-based nanoparticle drug delivery systems.

2.2 Experimental Section

2.2.1 Materials

All materials were purchased from Sigma-Aldrich (St. Louis, MO), if not specified, and used without further purification. Iron oxide MNPs (Meliorum Technologies, Rochester, NY), acetic acid (EM Science, Gibbstown, NJ), hydrochloric acid (HCl, EMD Chemicals Inc., Gibbstown, NJ), ethanol (Fisher Sci., Fair Lawn, NJ), and epoxy gel (Loctite Corp., Rocky Hill, CT) were purchased and used without further purification.

2.2.2 Surface Functionalization of MNPs

The surface of MNPs was functionalized with (3-aminopropyl)trimethoxysilane (APTMS, template for synthesizing WBPLP-coated MNPs) or vinyltrimethoxysilane (VTMS, template for synthesizing BPLP-coated MNPs) as described elsewhere [107]. In brief, MNPs (10 nm diameter) were dispersed in a mixture of de-ionized (DI) water and ethanol (1:99) by sonication at 50 W. Acetic acid (3 ml) was added after 10 minutes and sonication was continued for another 10 minutes. APTMS or VTMS (0.49 ml) was then added, and the reaction was stirred vigorously for 24 hours at room temperature to get amine-functionalized MNPs (amine-MNPs) or silane-functionalized MNPs (silane-MNPs). The particles were washed thrice with the mixture of water and ethanol.

2.2.3 Synthesis of WBPLP-MNPs and BPLP-MNPs

WBPLP and BPLP were synthesized using PEG or 1,8-octanediol, citric acid, and amino acids such as L-cysteine and serene following our previously developed protocols [101]. Briefly, for synthesizing WBPLP, equimolar amounts of PEG and citric acid were added and stirred with amino acids at molar ratios of amino acid/citric acid 0.2. After melting the mixture at 160°C for 20 min, the temperature was brought down to 140°C stirring continuously for another 75 minutes to obtain the WBPLP oligomers.

Similarly, BPLP was synthesized using 1,8-octanediol, citric acid, and amino acid. The polymers were purified by precipitating the oligomer/1,4-dioxane solution in water followed by freeze drying.

One of the challenges in developing a protocol for DICT-NPs was the surfactant selection. A wide range of surfactants and their two concentrations were chosen for the nanoparticle synthesis and a factorial design was implemented to study the effects of surfactant type and concentration on the nanoparticle formation. As shown in Table 2.1, sodium dodecyl sulfate (SDS, 0.5 and 2% w/v), poly vinyl alcohol (PVA, 1 and 5% w/v), Tween 20 (1 and 5% w/v), Pluronic F127 (0.5 and 2% w/v) and vitamin E (1 and 5% w/v) as surfactants, and BPLP (20 and 200 mg) were chosen as independent factors and nanoparticle size as a dependent factor. Using Design Expert, a design of experiments (DoE) software (Stat-Ease, Minneapolis, MN), various combinations of surfactant type, surfactant concentration, and BPLP concentration were chosen to synthesize nanoparticles as described in the following paragraph. Finally, the optimal surfactant and its concentration were chosen from the factorial analysis for later syntheses, which formed the smallest nanoparticles with high yield.

Table 2.1 Independent factors at two levels and dependent factors for the factorial analysis using DoE

Surfactant	Low Level (% w/v)	High Level (% w/v)	Particle Yield and Size
SDS	0.5	2.0	High, Small
PVA	1.0	5.0	Low, Large
Tween 20	1.0	5.0	No
Pluronic F127	0.5	2.0	Low, Large
Vitamin E	1.0	5.0	No

Note: For each surfactant type, 20 mg (low level) and 200 mg (high level) of BPLP were chosen to prepare nanoparticles.

From factorial analysis results, SDS was chosen as the best surfactant candidate for the nanoparticle formulations. Firstly, to synthesize WBPLP-MNPs, WBPLP was conjugated on the surface of MNPs using carbodiimide chemistry [44]. In brief, two separate solutions of WBPLP (250 mg) and amine-MNPs (20 mg) were prepared in 2-(*N*-morpholino)ethanesulfonic acid (MES) buffer (pH 5.6). *N*-(3-dimethylaminopropyl)-*N′*-ethylcarbodiimide hydrochloride (EDC) and *N*-hydroxysuccinimide (NHS) (1:1) were added to the polymer solution to activate the carboxyl groups on the WBPLP and the reaction was stirred for one hour. The amine-MNPs were then added to this solution and sonicated for five minutes at 40 W. SDS (14 mg) was added to the reaction and sonicated for another two minutes. Finally, the particle suspension was allowed to react while stirring for six hours. The WBPLP-MNPs were then washed multiple times with DI water and collected using a magnet.

To synthesize BPLP-MNPs, single emulsion method was used to physically incorporate silane-MNPs in BPLP shell. Briefly, silane-MNPs (10 mg) and BPLP (125 mg) were dispersed in 1,4-dioxane (2.5 ml) to form oil phase. An aqueous solution of SDS (16 mg/ml, 25 ml) was prepared to form water phase. Oil phase was then added drop-wise to water phase, and the solution was emulsified by sonicating for five minutes at 40 W. The BPLP-MNPs were then washed multiple times with DI water and collected using a magnet.

2.2.4 Characterization of WBPLP-MNPs and BPLP-MNPs

The size of the nanoparticles was determined using transmission electron microscopy (TEM, Tecnai G2 Spirit BioTWIN). In brief, nanoparticles suspended in DI water were placed on a foamvar-coated copper grid (Electron microscopy sciences, Hatfield, PA), dried, and observed in TEM. Hydrodynamic mean diameter, polydispersity index (PDI), and surface charge of the nanoparticles were obtained using zeta potential analyzer with a dynamic light scattering (DLS) detector (ZetaPALS, Brookhaven Instruments, Holtsville, NY). For these measurements, nanoparticles were suspended in DI water, placed in a cuvette that was later inserted in the ZetaPALS machine. Further, the nanoparticle stability was tested by measuring nanoparticles size, PDI, and zeta potential over a period of nine days. Nanoparticles were dispersed in cell culture medium (RPMI, Invitrogen Corp., Carlsbad, CA) containing 10% fetal bovine serum (FBS, Atlanta Biologicals, Lawrence Ville, GA), and particle size measurements were carried out every day.

Chemical characterization of the nanoparticles was performed using energy dispersive spectroscope (EDS, S-3000N, VP-SEM, Hitachi) and Fourier transform infra-red (FTIR) spectroscope (Nicolet-6700, Thermo Fisher Scientific). For EDS, a drop of nanoparticle solution was placed on a glass cover slip, dried, and analyzed for presence of basic elements in the sample. Whereas, for FTIR, dried nanoparticles were used to obtain FTIR spectra. Finally, to study degradation of the polymer shell, nanoparticles were suspended in DI water and incubated at 37°C over a time range. At each time point, particles were collected using a magnet and the dry weight of nanoparticles was recorded. A relative percentage of dry weights of the nanoparticles at all the time points were calculated with respect to the initial dry weight of the nanoparticles.

2.2.5 Magnetic Properties

The amount of iron in the nanoparticles was determined by iron content assays as described elsewhere [108]. Briefly, a nanoparticle sample was incubated in HCl (30% v/v) at 55°C for two hours on an orbital shaker. Ammonium persulfate (APS, 50 μg), an oxidizing agent for ferric ions, was added and shaking was continued for 15 minutes. Potassium thiocyanate (PTC, 0.1 M, 50 μl) was then added and shaking was continued for another 15 minutes. PTC reacts with iron to form an insoluble pigment, which was quantified by absorbance measurement at 520 nm using UV-Vis spectrometer (Tecan Ltd., Durham, NC) and compared against standard concentrations of iron oxide nanoparticles. Moreover, a superconducting quantum interference device

(SQUID, Quantum Design, CA) magnetometer was used to evaluate the magnetic properties of the nanoparticles [107]. The nanoparticles were trapped in epoxy gel (Loctite Corp., Rocky Hill, CT) and allowed to dry for five minutes. The dried sample was then mounted in a transparent drinking straw, and measurement was done to obtain a magnetic hysteresis loop. Similarly, a control sample was prepared using bare MNPs and its magnetic hysteresis loop was compared with that of the polymer-coated MNPs.

2.2.6 Cell Culture

Adult human dermal fibroblasts (HDFs) were purchased from Invitrogen Corp. (Carlsbad, CA), cultured in dulbecco’s modified eagle medium (DMEM) supplemented with 10% FBS and 1% penicillin-streptomycin (PS, Invitrogen Corp., Carlsbad, CA). Whereas prostate cancer cells, PC3 and LNCaP, were purchased from ATCC, Manassas, VA, cultured in RPMI supplemented with 10% FBS and 1% PS. All the cells were cultured in a humid environment at 37°C and 5% CO_2. The primary HDFs up to passage 10 were used for the experiments.

2.2.7 Dual-imaging Properties

Agarose platforms were prepared for MRI by dissolving agarose (1% w/v) in DI water. Two types of samples were prepared by dispersing DICT-NPs only and DICT-NPs uptaken by PC3 cells at different concentrations in agarose phantoms. The control samples were prepared by dispersing bare MNPs, BPLP nanoparticles (without MNPs), and PC3 cells only in agarose phantoms. In brief, to prepare cell based phantoms, PC3 cells were incubated with nanoparticles (300 µg/ml) for two hours. The cells were then washed with PBS and trypsinized to get a cell pellet. The PC3 cells labeled with nanoparticles were added to the agarose solution to get the desired concentrations. MR images and relaxation time of nanoparticles were obtained as previously described [44] using a Varian unity INOVA 4.7T 40-cm horizontal MR system equipped with actively shielded gradients (Varian, Palo Alto, CA) (205 mm with 22G/cm). The sample was put into a 35 mm volume radiofrequency coil. Multislice T2-weighted images (TR = 2000 msec; TE = 15 msec; field of view of 30 mm × 30 mm; matrix = 128 × 128; slice thickness = 2 mm) were acquired with spin echo pulse sequence. Further, the fluorescence of the nanoparticles from the polymer coating on the MNPs was observed under an enhanced optical fluorescent microscope (Cytoviva, Olympus America Inc., Center Valley, PA). Moreover, the fluorescence from the nanoparticles was also observed in UV light and compared against the fluorescence in white light. The control sample contained bare MNPs.

2.2.8 In Vitro Cell Studies

The cytotoxic effects of nanoparticles were tested on HDFs' survival. The cells were seeded at a density of 5,000 cells/well in 96-well plates and allowed to attach and grow for 24 hours at 37°C. Nanoparticles were sterilized in UV light for 30 minutes and then suspended in cell medium to get final concentrations of 50, 100, 200, 300, and 500 µg/ml. Cells were exposed to these nanoparticle concentrations for 24 and 48 hours at 37°C and 5% CO_2. Cells exposed to nanoparticle-free medium served as control. Cell survival was then determined using colorimetric MTS assays (CellTiter 96® AQ$_{ueous}$ One Solution Cell Proliferation Assay, Promega, Madison, WI) following the manufacturer's instructions.

Further, to determine the cellular uptake of nanoparticles, PC3 and LNCaP cells were seeded at a density of 10,000 cells/well in 48-well plates and allowed to attach and grow for 24 hours at 37°C. After UV sterilization, nanoparticles were suspended in cell medium to get final concentrations of 0, 50, 100, 200, 300, and 500 µg/ml. The cells were then incubated with these nanoparticle suspensions for two hours. After incubation, cells were washed thoroughly with phosphate buffer solution (PBS) to wash away nanoparticles that were not engulfed by the cells. Cells were then lysed with 1% Triton X-100 (MP Biomedicals Inc., Solon, OH) in PBS. To determine the amount of iron (Fe) uptake, iron assay was performed as described earlier. A part of the cell lysate was tested for the total DNA content of seeded cells using Picogreen DNA assays (Invitrogen Corp.) following the manufacturer's instructions, and this data was used to normalize the iron content.

Cellular uptake of nanoparticles by PC3 cells was also visualized by TEM. Specimen for TEM were prepared as described elsewhere [109]. Briefly, after cellular uptake of nanoparticles, cells were washed with PBS, fixed with 2.5% glutaraldehyde in 0.1 M cacodylate buffer, and then cells were removed with a scraper. The cells were gently centrifuged to form a pellet that was resuspended in a fresh fixative for one hour. Cells were gently pelleted, resuspended in cacodylate buffer, again pelleted, and enrobed in low-melt agarose. The cell pellets were then placed in 1% osmium tetroxide in cacodylate buffer for one hour at room temperature. Following water washes, the cell pellets were placed in 2% aqueous uranyl acetate overnight at 4°C. Cells were dehydrated through a gradual series of ethanol solutions and a transitional fluid, propylene oxide. Cell pellets were then placed in a 2:1 mixture of propylene oxide:EMbed-812 epoxy resin on a rotator at room temperature for one hour. Then, the cell pellets were placed in 1:2 mixture of propylene oxide:EMbed-812 while rotating overnight. Cells were changed into fresh EMbed-812 at least twice during the day with rotation. Finally, the cells were embedded, using fresh EMbed-812, in labeled embedding molds and polymerized in a 70°C oven overnight.

2.2.9 Drug Loading and Release

Docetaxel (Doc) was chosen as a model anticancer drug to load into the nanoparticles. Doc is a clinical anti-mitotic chemotherapy drug that interferes with cell division [110]. Doc has high affinity to bind to microtubules reversibly, which stabilizes microtubules and prevents depolymerisation/disassembly from calcium ions. This leads to a significant decrease in free tubulin, which is needed for microtubule formation, and results in the inhibition of mitotic cell division between metaphase and anaphase, preventing further cancer cell progeny. Only BPLP-MNPs were chosen for the drug loading and release study as hydrophobic Doc can easily be loaded in the BPLP polymers. For drug loading, Doc (0.5 mg) was mixed with BPLP/1,4-dioxane solution while formulating BPLP-MNPs. After nanoparticle formulation, Doc-loaded BPLP-MNPs (Doc-BPLP-MNPs) were separated and supernatant was collected to analyze the unloaded amount of Doc. This amount was then compared with the initial amount of Doc to determine the loading efficiency of the Doc indirectly, which was calculated using the following equation.

$$\text{Loading efficiency} = \frac{\text{Initial amount of Doc used - Doc present in supernatant}}{\text{Initial amount of Doc used}} \text{ x } 100\%$$

Doc-BPLP-MNPs were then suspended in PBS and incubated at 37°C on a revolving rotator for drug release studies. At predetermined time intervals, Doc-BPLP-MNPs were recruited at the bottom of the tube using a magnet, and the supernatant containing released Doc (1 ml) was collected. Fresh PBS (1 ml) was then added to reconstitute the volume in the tubes. At the end of the study, the Doc released samples at all the time points, unloaded Doc in the supernatant, and the standard (known) concentrations of Doc were read at an absorption wavelength of 230 nm using UV-Vis spectrometer. The Doc concentrations in the release samples were calculated against the Doc standard curve. Percentage cumulative release curve of Doc was then plotted as a function of time.

2.2.10 Pharmacological Activity of Drug-loaded Nanoparticles

The pharmacological activity of Doc-loaded BPLP-MNPs (Doc-BPLP-MNPs) was evaluated in comparison with free Doc and empty BPLP-MNPs. The LNCaP cells were seeded in 96-well plates as described before. The cells were exposed to free Doc,

Doc-BPLP-MNPs, and empty BPLP-MNPs by keeping the Doc concentrations (1, 10 and 50 μg/ml) the same in the first two groups and the BPLP-MNPs concentrations (30, 300 and 1500 μg/ml) the same in the last two groups. The cells exposed to media only served as controls. After 24 hours of incubation, MTS assays were carried out and the cell survival was calculated relative to the control.

2.2.11 Statistical Analysis

The results obtained were analyzed using one-way analysis of variance with $p < 0.05$ and post hoc comparisons (StatView, Version 5.0.1, SAS Institute Inc., Cary, NC). All the experiments were repeated multiple (at least two) times with a sample size of four (n=4). All the results were presented as mean ± standard deviation (SD) if not specified.

2.3 Results and Discussion

2.3.1 Synthesis and Characterization of Nanoparticles

Polymer-coated MNP structures using various types of polymers have been extensively developed and investigated for cancer detection and treatment [107, 111]. Herein, we demonstrated the potential use of the DICT-NPs with WBPLP-/BPLP-MNP structures for prostate cancer imaging and therapy. Firstly, a factorial analysis was performed to select the surfactant type and concentration, which gave the highest yield of smaller particles using SDS as a surfactant. Tween 20 and vitamin E did not form the particles at all; however, PVA and pluronic F127 were successful in forming a low yield of particles with large diameter (Table 2.1). Therefore, SDS was chosen as the surfactant candidate for further nanoparticle formulations because SDS formed a high yield of small diameter particles (about 200 nm). Nanoparticles were then formulated as shown in the schematic representation of WBPLP-MNPs and BPLP-MNPs (Figure 2.1). As shown in Figure 2.2, TEM images (insets) show a spherical morphology of the polymer-coated MNPs with more dispersion and bare MNPs that tend to aggregate in the absence of polymer coating.

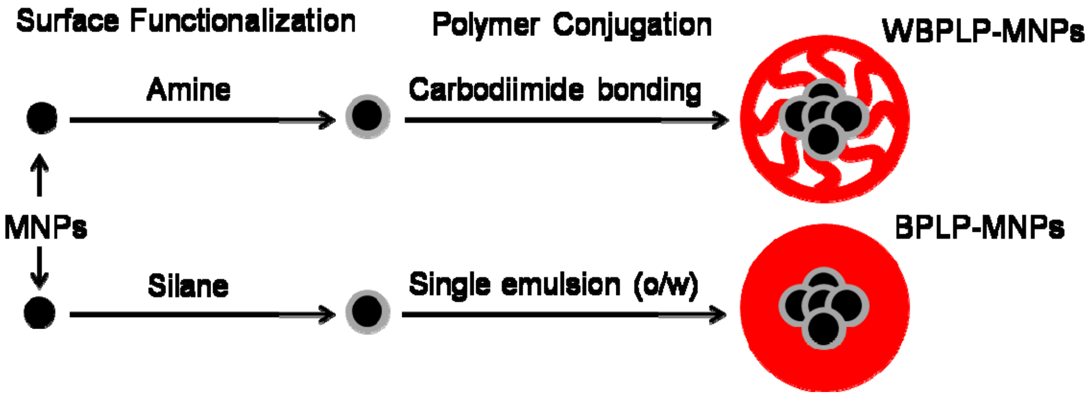

Figure 2.1 Schematics of WBPLP-MNPs and BPLP-MNPs showing formulation process.

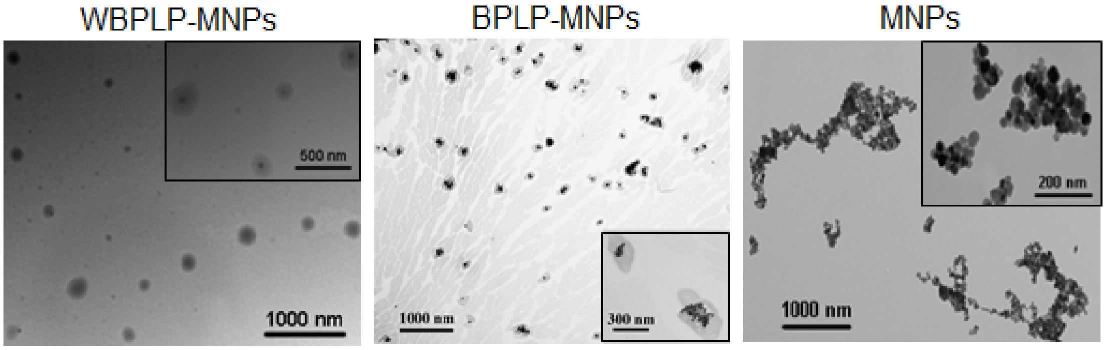

Figure 2.2 TEM image of WBPLP-MNPs (average size: 220 nm), BPLP-MNPs (average size: 212 nm), and bare MNPs (average size: 10 nm).

Approximately, 110 to 130 MNPs were present in the darker area of one nanoparticle. The numbers of MNPs in the core were determined by dividing the volume of the darker area shown in TEM by the volume of a bare MNP, considering 25% void space among MNPs. The presence of Fe_3O_4 in the darker area was also confirmed by EDS analysis (Figure 2.3). EDS analysis showed that the WBPLP-MNPs sample is composed of C (14.65 wt %), O (24.10 wt %) and Fe (61.24 wt %) elements; and the BPLP-MNPs sample is composed of C (12.04 wt %), O (20.18 wt %) and Fe (67.78 wt %) elements.

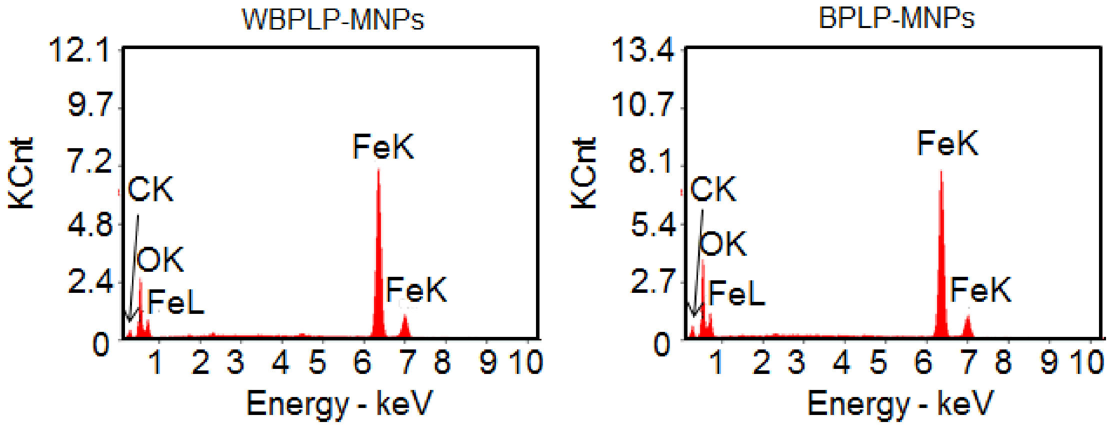

Figure 2.3 EDS spectrum of WBPLP-MNPs and BPLP-MNPs showing peaks associated with major elements such as Fe, O, and C.

As determined by DLS measurements in DI water and cell culture media containing 10% serum, hydrodynamic diameter of WBPLP-MNPs (238 nm and 236 nm) and BPLP-MNPs (235 nm and 229 nm), respectively, did not vary irrespective of the solvent (Table 2.2). The PDI of WBPLP-MNPs and BPLP-MNPs in both the solvents was in mid-range polydispersity (0.08 – 0.7) [112]. The nanoparticle size and PDI were also measured over a period of nine days in the culture medium to study the stability of the nanoparticles. The nanoparticles were stable and did not aggregate as observed from the size and PDI readings (Figure 2.4). However, the larger size of WBPLP-MNPs and BPLP-MNPs might cause an issue for future *in vivo* studies as nanoparticles with large sizes are usually associated with rapid clearance of nanoparticles by RES [113]. To reduce the particle size, after the nanoparticle formulation, DICT-NPs can be filtered using 0.2 micron filter to collect approximately 100 nm sized particles (Table 2.2). In addition, DICT-NPs are fully degradable and can be administered locally, following magnetic targeting to quickly recruit the nanoparticles to the target site.

Table 2.2 Physical and surface properties of DICT-NPs

Sample	Diameter (nm)	PDI	Zeta Potential (mV)
MNPs	10^a	0.30^c	-5.13^c
Silane-MNPs	18^b	0.28^c	-21.00^c
Amine-MNPs	17^b	0.26^c	-21.23^c
WBPLP-MNPs	238^c, 236^d, 113^e	0.21^c, 0.22^d, 0.19^e	-25.85^c, -16.19^d
BPLP-MNPs	235^c, 229^d, 107^e	0.15^c, 0.25^d, 0.14^e	-31.32^c, -12.09^d

[a]Size provided by the supplier. [b]Size obtained from TEM analysis (images not shown). [c]Measured in DI water. [d]Measured in RPMI containing 10% FBS. [e]Measured after filtration (0.2 micron filter).

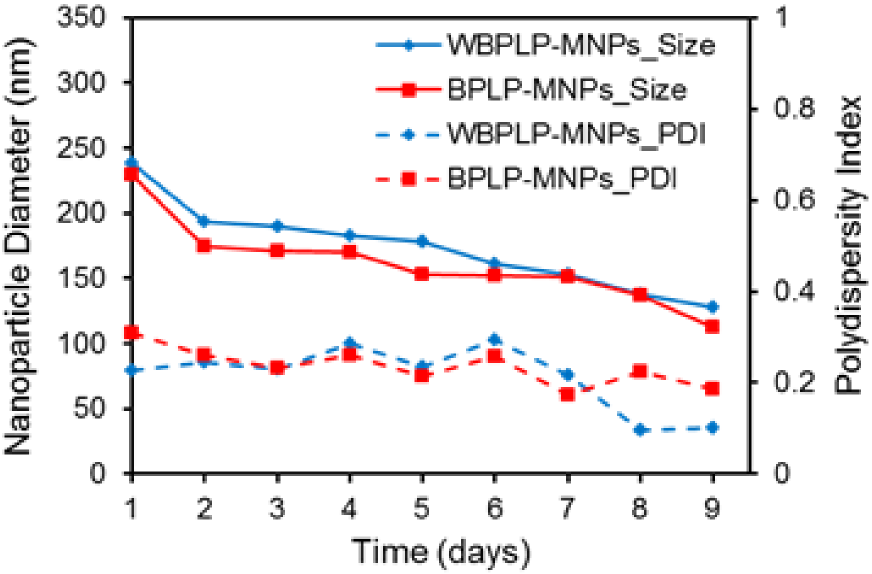

Figure 2.4 Stability of nanoparticles. Hydrodynamic diameters and PDI, measured over a period of nine days in cell culture media containing 10% serum, show WBPLP-MNPs and BPLP-MNPs were stable and did not form aggregates.

Further, surface charge on the WBPLP-MNPs and BPLP-MNPs was –25.85 mV and –31.32 mV, respectively, as determined by zeta potential analyzer (Table 2.2). The nanoparticle surface charge was changed from -5.13 mV for bare MNPs to -25.85 or -31.32 mV for DICT-NPs. The increase in surface charge suggests that the stability of the nanoparticles increased after polymer coating. However, in the cell culture media, the zeta potential of WBPLP-MNPs and BPLP-MNPs reduced to -16.19 mV and -12.09 mV. The change in zeta potential results from the serum present in the media [114]. Although the zeta potential of nanoparticles reduced in culture medium, they were still in a stable range (±10 to ±30 mV) [115], and thereby would not aggregate due to electrostatic repulsion among the negatively charged polymer coatings.

2.3.2 FTIR of Nanoparticles

Chemical structures of the nanoparticles were characterized using FTIR, which showed the characteristic peaks of Fe-O at 550 cm^{-1}, $–CH_2$ from polymer backbone at 2919 cm^{-1}, –C=O from citric acid at 1707 cm^{-1}, and –C(=O)NH between polymer and amino acid at 1550 cm^{-1} (Figure 2.5). These findings were in agreement with our previous observations confirming the presence of MNPs [107] and all the corresponding bonds from WBPLP/BPLP coating [101].

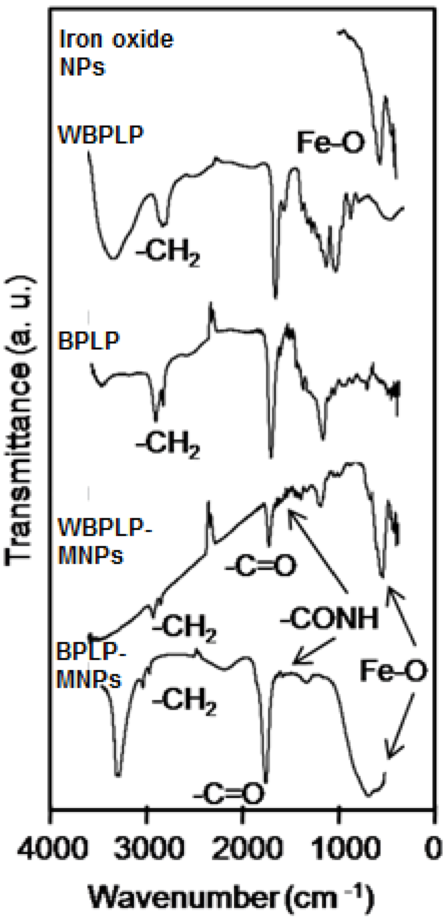

Figure 2.5 FTIR spectra of iron oxide nanoparticles, WBPLP, BPLP, WBPLP-MNPs, and BPLP-MNPs. Arrows point to the essential peaks associated to the bonds in the nanoparticle structures.

2.3.3 Degradation of Nanoparticles

Degradation of the polymer coating on MNPs in DI water was studied over time. It was observed that the WBPLP and BPLP coating was degraded completely within 21 and 24 days (Figure 2.6), respectively, which was in agreement with our previous study on pure BPLP degradation [101]. BPLPs underwent hydrolysis and degraded into their monomeric units including PEG or 1,8-octanediol, citric acid, and amino acids. There was a faster degradation of BPLP than WBPLP within the initial five days, which can be attributed to the loose binding of BPLP over MNP surfaces during the emulsion process, compared to covalent binding of WBPLP to MNPs via carbodiimide binding.

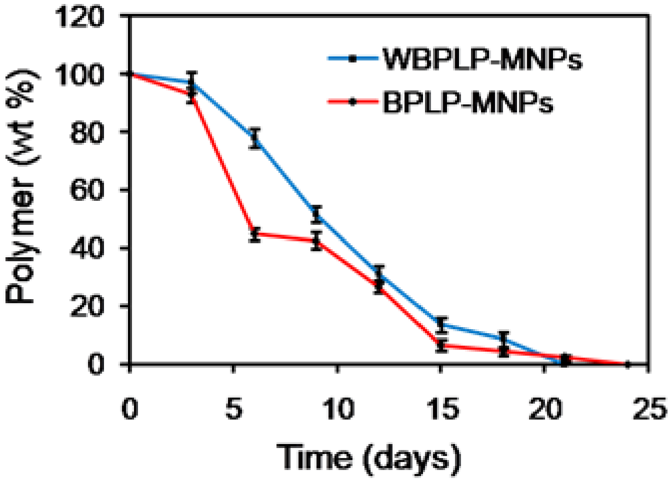

Figure 2.6 Degradation profiles of WBPLP and BPLP coatings on MNPs showing complete degradation in 3 weeks.

2.3.4 Magnetic Characterization of Nanoparticles

The nanoparticles possess strong superparamagnetic properties. WBPLP-MNPs and BPLP-MNPs were comprised of approximately 75% and 80% mass of iron, respectively (Table 2.3). Further, in the absence of an external magnet, nanoparticles were suspended and well-dispersed in water (Figures 2.7A and 2.7B). While in the presence of an external magnet, nanoparticles concentrated toward the magnet, demonstrating the recruitment of nanoparticles via magnetic targeting.

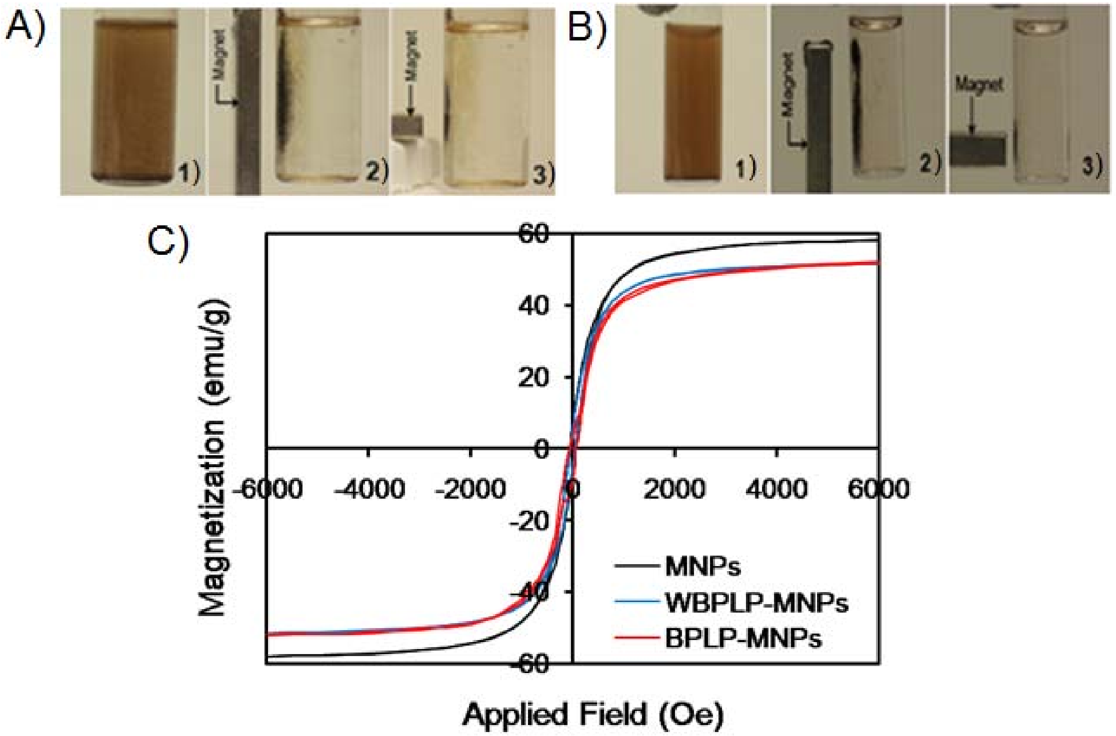

Figure 2.7 Photographs of (A) WBPLP-MNPs and (B) BPLP-MNPs showing 1) nanoparticle suspension and 2, 3) recruitment of nanoparticles in the magnetic field (1.3 T) generated by a magnet. (C) Magnetization hysteresis loops of nanoparticles showing superparamagnetic behavior.

Table 2.3 Iron content and magnetic characterization of DICT-NPs

Sample	Iron (%)	Saturation Magnetization (emu/g or M_s)	Remanence (M_r/M_s)	Coercivity (Oe or H_c)
MNPs	100	57.88	6.73	65.23
WBPLP-MNPs	75	51.42	5.14	50.59
BPLP-MNPs	80	52.04	5.77	59.72

The saturation magnetization of the WBPLP-MNPs and BPLP-MNPs (51.42 and 52.04 emu/g, respectively) was lower than that of bare MNPs (57.88 emu/g) (Figure 2.7C and Table 2.3). This decrease in the saturation magnetization is due to the presence of polymer coating on the surface of MNPs. It was frequently observed that there was a decrease in saturation magnetization when MNPs were coated with various polymers such as polystyrene [116], PNIPAAm [107], PLGA [117], and PEG [111]. The remanence of WBPLP-MNPs and BPLP-MNPs was 5.14 and 5.77 (M_r/M_s), respectively, as compared to 6.73 (M_r/M_s) in the case of bare MNPs. Whereas, the coercivity of WBPLP-MNPs and BPLP-MNPs was 50.59 and 59.72 Oe, respectively, as compared to 65.23 Oe in the case of bare MNPs (Table 2.3). There was an increase in the coercivity of the DICT-NPs due to increased particle size and separation distance as a result of polymer coating on the surface of the MNPs. This data suggest that all the samples contain a fraction of nanoparticles in a blocked magnetic (superparamagnetic) state, which has low coercive forces, small remanent magnetic induction, and long and narrow hysteresis loops [118].

2.3.5 MRI

The DICT-NPs were also tested as contrast agents for MRI using agarose phantoms containing either DICT-NPs alone or DICT-NPs uptaken by PC3 cells. A dark and dispersed negative contrast was observed from the samples containing DICT-NPs, even at a low concentration of 100 μg iron/ml (Figure 2.8D and 2.8J). The negative contrast was nanoparticle dose-dependent (Figure 2.8D-F and 2.8J-L), which was also confirmed from the relative signal intensities of the samples. For example, there was a 12% (Figure 2.8D), 56% (Figure 2.8E), and 92% (Figure 2.8F) drop in the signal intensity compared to the control (Figure 2.8A). Control samples consisting of

BPLP nanoparticles without MNPs (Figure 2.8A) and PC3 cells alone (Figure 2.8B) did not generate a contrast, but bare MNPs produced a very dark negative contrast (Figure 2.8C). These results suggest that the contrast generated in MRI is only due to the presence of MNPs in DICT-NPs. When the nanoparticles were uptaken by the cells, the MRI contrast was dark and even more dispersed than those of DICT-NPs only (Figure 2.8G-I and 2.8M-O). The negative contrast was not only dependent on the concentrations of nanoparticles, but also on the concentrations of cells internalizing these nanoparticles. The nanoparticles produce a dark, well-dispersed MRI contrast even at a low number (10,000) of cells. Pinkernelle et al. [119] observed similar results about the effects of nanoparticle concentration and cell number on MRI signals when iron oxide nanoparticles were incubated with human colon carcinoma cells. The difference between the MRI contrast signal dispersion between samples with and without the cells might be due to a reduction in nanoparticle aggregation because of cellular uptake producing a more dispersed contrast than that of nanoparticles only. We have previously observed a dark and dispersed MRI contrast signal from our thermo-sensitive polymer-coated MNPs uptaken by JHU31 cells [44]. Some other groups have also reported a dark negative MRI contrast signal from their iron oxide-based nanoparticles [112, 119].

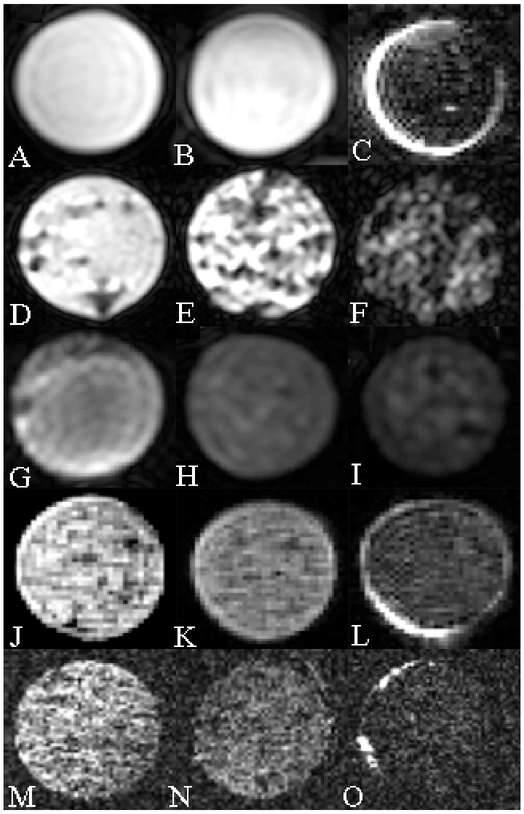

Figure 2.8 MR images of agarose phantoms containing (A) 5 mg/ml BPLP nanoparticles, (B) 10^4 PC3 cells, and (C) 0.1 mg/ml MNPs as control samples. Experimental agarose phantoms contain (D) WBPLP-MNPs of 0.1 mg/ml, (E) 0.3 mg/ml, and (F) 0.6 mg/ml concentrations; (G) 0.3 mg/ml WBPLP-MNPs uptaken by 10^4, (H) 10^6, and (I) 5×10^6 PC3 cells; similarly (J) BPLP-MNPs of 0.1 mg/ml, (K) 0.3 mg/ml, and (L) 0.6 mg/ml concentrations; and (M) 0.3 mg/ml BPLP-MNPs uptaken by 10^4 PC3 cells, (N) 10^6 PC3 cells, and (O) 5×10^6 PC3 cells.

Furthermore, T2 relaxation time of WBPLP-MNPs and BPLP-MNPs was 53 and 14 msec, respectively. T2 is spin-spin relaxation time that is a measure of how fast the spins diphase. The shorter the T2, the faster the signal disappears and hence gives a darker contrast in T2 weighted images. The relaxation time of BPLP-MNPs (14 msec) is comparable to commercially marketed iron oxide-based MRI contrast agents such as Feridex (10 msec), Resovist (6.6 msec) and Ferumoxtran-10 (16.7 msec) [67].

Although, MRI has the advantages of exceptional tissue contrast and spatial resolution and has been widely used in clinical settings [99], similar to CT and PET, the MRI imaging technique is also insensitive for the small lesions [10].

2.3.6 Optical/Fluorescence Imaging

To overcome the limitations of conventional imaging techniques, the optical imaging approach has been investigated. Although optical fluorescence imaging has a potential to detect tiny tumor masses with a high sensitivity [120], its applications *in vivo* are hampered by a limited tissue penetration depth, high (or presence of) tissue auto-fluorescence, and lack of anatomic resolution and spatial information [121]. Therefore, the combination of MRI and optical imaging techniques may improve the identification of small cancer lesions to improve the detection accuracy. In the past, dual-functional imaging nanoparticles have been generated by linking MNPs with quantum dots and/or Cy5.5 dyes, so that they can be detectable by both fluorescence imaging and MRI [51, 71]. The polymer coating of our DICT-NPs itself can act as biodegradable imaging probes for targeted imaging. Moreover, BPLPs can be excited and emitted at different wavelengths ranging from UV to near infra-red. Fluorescence properties of WBPLP and BPLP coatings on MNPs were tested under UV light and an enhanced optical fluorescent microscope. Figure 2.9A shows the samples under white light and Figure 2.9B shows a bright fluorescence from WBPLP-MNPs and BPLP-MNPs under UV light. There was no fluorescence observed from bare MNPs under UV light due to the absence of fluorescent polymer coating on the MNPs. Moreover, the nanoparticles exhibited their bright fluorescence observed by the enhanced optical fluorescent microscope (Figures 2.9C-D). The findings suggest that these nanoparticles could be used as dual-imaging (optical imaging and MRI) agents.

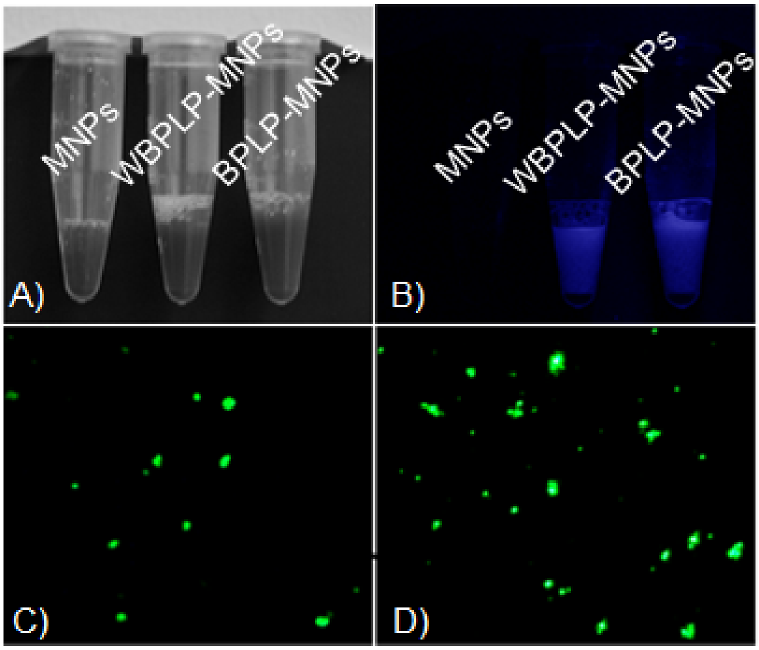

Figure 2.9 Photographs of nanoparticle suspensions in (A) white light and (B) UV light. Fluorescence from WBPLP-MNPs and BPLP-MNPs was observed in UV light only. Photomicrographs of fluorescence observed from (C) WBPLP-MNPs and (D) BPLP-MNPs under an enhanced optical microscope at 40x magnification.

2.3.7 Cytotoxicity of Nanoparticles

The cytotoxicity results of the DICT-NPs are presented in Figure 2.10. The nanoparticles were cytocompatible and did not show a significant decrease in cell survival when HDFs were exposed to nanoparticles with concentrations up to 500 μg/ml after 48 hours of exposure. BPLP-MNPs were more cytocompatible than WBPLP-MNPs, especially at higher concentration and longer incubation periods.

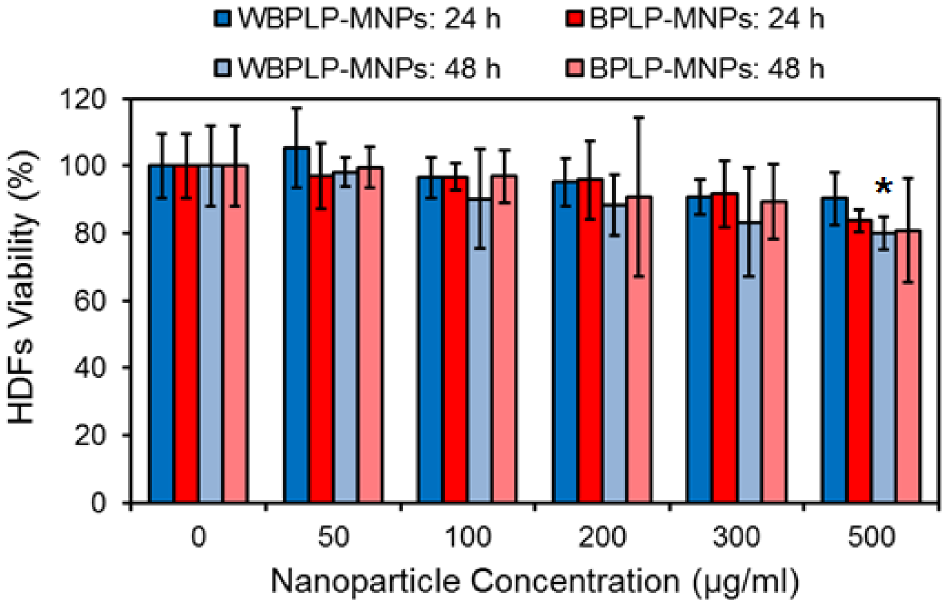

Figure 2.10 Cytotoxicity of nanoparticles on HDFs. BPLP-MNPs were more cytocompatible than WBPLP-MNPs, especially at longer incubation periods (* $p < 0.05$ compared to control).

The DICT-NPs may potentially eliminate the long-term *in vivo* toxicity concern and bypass the size limitation for in vivo clearance as the particles will be degraded and cleared by the body. BPLPs have previously demonstrated their excellent cytocompatibility *in vitro* when cultured with 3T3 fibroblasts and tissue-compatibility when implanted in rats [101]. Other studies have reported that there was a significant increase in the cytocompatibility of MNPs when they were coated with polymers such as Pluronics [112] or PNIPAAm/copolymers [44]. The above cytocompatibility evaluation further supported the potential of these nanoparticles for biomedical uses.

2.3.8 Cellular Uptake of Nanoparticles

The optimal concentration of nanoparticles uptaken by prostate cancer cell lines, PC3 and LNCaP, was determined by cellular uptake studies. A cancer cell-selective, dose- and magnetic field-dependent uptake of DICT-NPs by prostate cancer cells (PC3 and LNCaP cells) are shown in Figures 2.11. The cellular uptake of nanoparticles was saturated at 300 μg/ml, which can be attributed to the exocytosis of nanoparticles at higher concentrations by the cells [122]. Previously, we have reported that the uptake of our thermo-responsive polymer-coated MNPs by JHU31 prostate cancer cells was dose-dependent and reached a plateau at 300 μg/ml concentration of nanoparticles [44]. The uptake is dependent on various factors such as particle size, concentration, incubation time, and surface charge [123, 124]. Moreover, in the presence of an external magnetic field of 1.3 T, the cellular uptake of nanoparticles increased significantly and did not saturate until 500 μg/ml concentration of nanoparticles. These results suggest that the presence of a magnetic field reinforces the cellular uptake of DICT-NPs, which will be useful in delivering higher amounts of imaging or therapeutic agents to cancer cells via magnetic targeting.

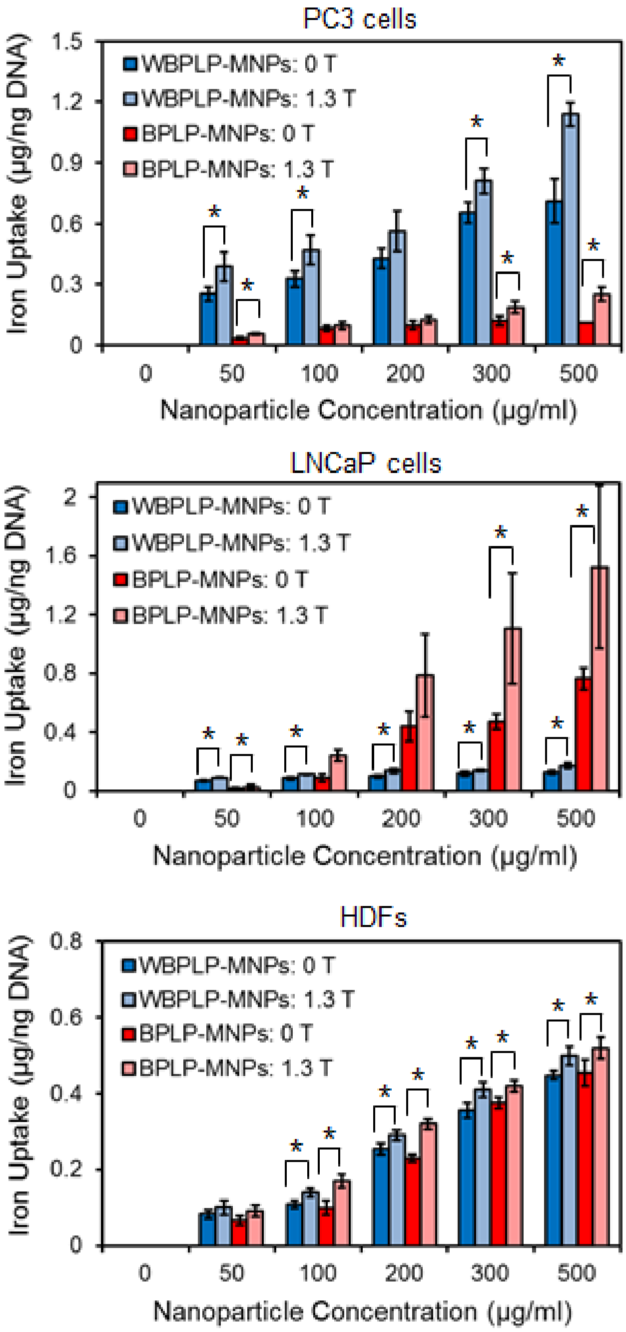

Figure 2.11 Cell-selective, dose-dependent, and magnetic field-dependent cellular uptake of nanoparticles. Higher uptake of WBPLP-MNPs and BPLP-MNPs by PC3 cells and LNCaP cells, respectively. Control experiment of nanoparticle uptake by HDFs with a lower and no significant difference between uptake of WBPLP-MNPs and BPLP-MNPs (* $p < 0.05$).

It is very interesting that WBPLP-MNPs and BPLP-MNPs exhibited cellular uptake selectivity. As observed in Figure 2.11, BPLP-MNPs showed significantly higher uptake by LNCaP cells (PSMA$^+$ and non-metastatic) than WBPLP-MNPs. While in the case of PC3 cells (PSMA$^-$ and metastatic) [125], WBPLP-MNPs were uptaken significantly higher than BPLP-MNPs. Whereas in a control experiment, relatively low and equal amounts of WBPLP-MNPs and BPLP-MNPs were uptaken by healthy HDFs. The results of nanoparticle uptake by PC3 cells were reconfirmed by TEM analysis. It was clearly shown (Figure 2.12) that WBPLP-MNPs (hydrophilic) were present in the cytoplasm of PC3 cells in a greater number (~35 vs. ~15) than BPLP-MNPs (hydrophobic). The numbers of nanoparticles in the cytoplasm were calculated by visual observation on at least 20 cells. Insets in Figure 2.12 show magnified images of the presence of nanoparticles in the cytoplasm.

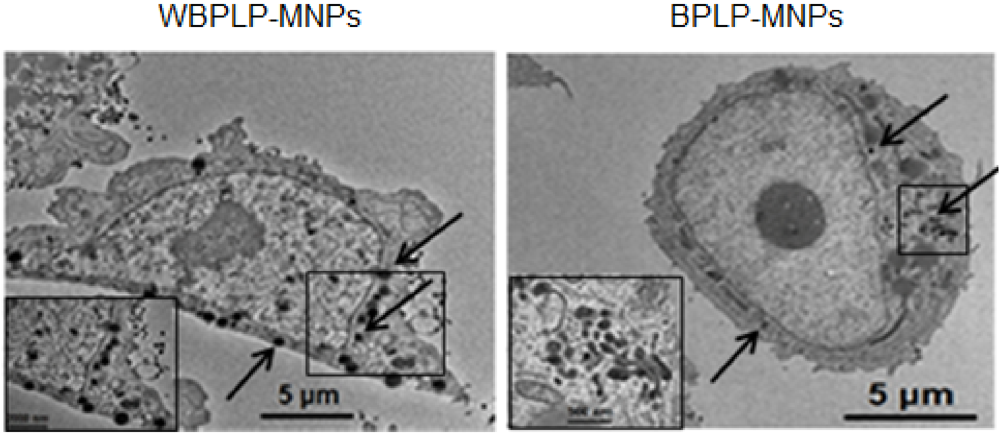

Figure 2.12 TEM images of higher uptake of WBPLP-MNPs, whereas least uptake of BPLP-MNPs by PC3 cells (insets show magnified images of the boxed areas in cells and arrows indicate location of nanoparticles in the cytoplasm).

Therefore, by varying and balancing the hydrophilicity/hydrophobicity of monomers in BPLP syntheses, suitable DICT-NPs can potentially be made for targeting prostate cancer cells at different stages of cancer. Few groups have reported the effects of hydrophilicity levels of biomaterials on cellular uptake. For example, Nam et al. [109] observed an enhanced distribution of hydrophobically modified glycol chitosan nanoparticles in HeLa cells compared to hydrophilic glycol chitosan nanoparticles. Moreover, Sunshine et al. [64] found that polymers containing hydrophobic backbone promoted transfection of COS-7 cells compared to that of hydrophilic backbone. On the contrary, Gaumet et al. [126] observed more hydrophilic chitosan-coated PLGA nanoparticles in cells compared to PLGA nanoparticles alone. These observations reveal that the intracellular fate of nanoparticles is not only dependent on hydrophilicity levels of a polymer, but also on many factors including cell type, cell surface antigens, charge on the biomaterial, chemical functionality of polymers, and so on [65].

2.3.9 Drug Loading and Release

Doc was loaded in the BPLP-MNPs at the time of nanoparticle formulation. The loading efficiency of Doc in the particles was approximately 68%. There was a burst release of Doc (approximately 50%) within the first day, followed by a sustained release until 21 days, which resulted in 100% Doc release (Figure 2.13). These results coincide with the degradation kinetics of BPLP, where BPLP was degraded completely within three weeks (Figure 2.6). The observations indicate that the Doc release was dependent on the degradation of BPLP.

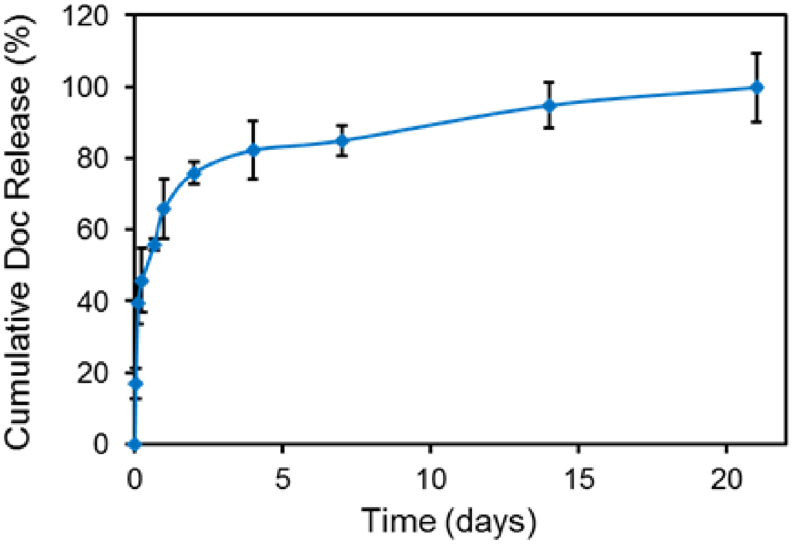

Figure 2.13 Doc loading and release kinetics. A biphasic release of Doc from BPLP-MNPs showing 100% release in 21 days.

2.3.10 Pharmacological Activity of Drug-loaded Nanoparticles

Pharmacological activity of Doc released from the BPLP-MNPs was evaluated on the LNCaP cell survival. As shown in Figure 2.14, free Doc and Doc-BPLP-MNPs were effective in killing the LNCaP cells due to the drug effects, whereas empty BPLP-MNPs were compatible with the LNCaP cells. Cell survival was reduced to 65, 47 and 18% at 1, 10 and 50 µg/ml of free Doc, respectively. In case of Doc-BPLP-MNPs, the released Doc was effective in reducing the cell survival to 69, 50 and 22% at 1, 10 and 50 µg/ml drug-releasing BPLP-MNPs, respectively. Empty BPLP-MNPs were used in the study as controls for Doc-BPLP-MNPs, which showed cell survival of 93, 82 and 71% at 30, 300 and 1500 µg/ml, respectively. These observations can be supported by the Doc release data. The burst release of Doc (approximately 50%) from the BPLP-MNPs within first 24 hours might account for the high toxicity of Doc to LNCaP cells.

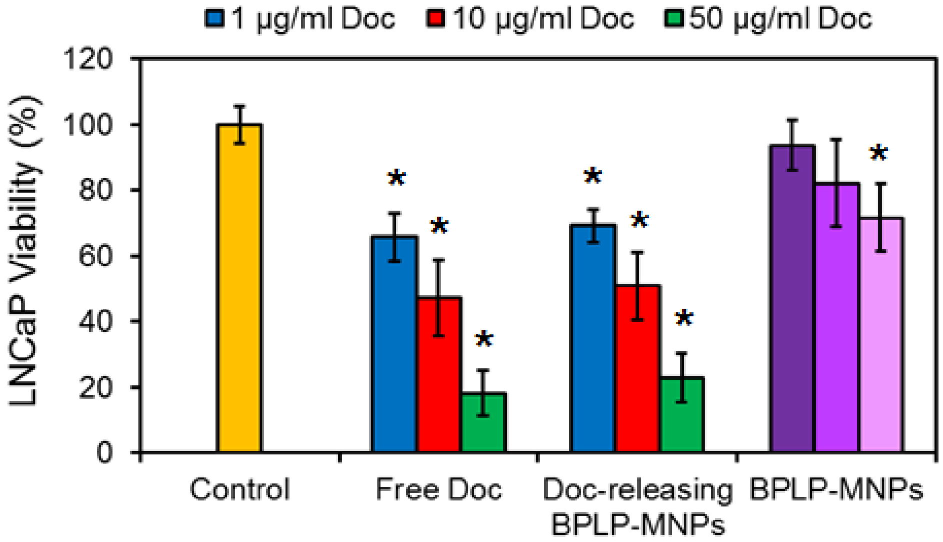

Figure 2.14 Pharmacological effects of Doc-BPLP-MNPs after 24 hours of exposure. Empty BPLP-MNPs showed no cytotoxic effects, whereas free Doc and Doc-BPLP-MNPs showed significant cell mortality at all concentrations (* $p < 0.05$).

2.4 Summary

We successfully synthesized and characterized fully biodegradable DICT-NPs with magnetic targeting, dual-imaging (optical imaging and MRI), and therapeutic capabilities in a single setting without using exogenous fluorescent organic dyes or QDs. DICT-NPs eliminate long-term toxicity concerns and bypass the size limitations for *in vivo* clearance in the traditional nanoparticle designs. The magnetic properties of the MNPs were preserved after WBPLP and BPLP incorporation. Dual-imaging studies revealed that DICT-NPs are capable of both optical imaging and MRI. These cytocompatible nanoparticles exhibited interesting cancer cell selectivity for cellular uptake. The cellular uptake of the nanoparticles was further reinforced by a magnetic field. Finally, the nanoparticles released drugs in biphasic manner, which were therapeutically effective in suppressing cancer cell survival compared. Future work involves *in vivo* biodistribution of the nanoparticles. The difference in the tumor uptake and the biodistribution of the WBPLP-MNPs and BPLP-MNPs will be studied qualitatively using Prussian blue staining and quantitatively using iron assays as explained in chapter 3.

CHAPTER 3

PROSTATE CANCER-SPECIFIC THERMO-RESPONSIVE POLYMER-COATED MNPs

3.1 Introduction

Thermo-responsive polymer coatings have attracted great attention in the field of drug delivery because they release drugs in a controlled and temperature-dependent manner. PNIPAAm and its copolymers are the most commonly used thermo-responsive polymers for such applications [107, 127]. The present study uses poly(*N*-isopropylacrylamide-acrylamide-allylamine) (PNIPAAm-AAm-AH) that exhibits LCST at ~ 39°C and carries amine functional groups on the surface for conjugation of biomolecules including targeting ligands. This polymer is in its swollen state at temperatures below the LCST. As the temperature is increased above the LCST, the transition phase takes place, causing the polymer to collapse, shrink, and release therapeutic agents embedded inside the materials. Coating PNIPAAm-AAm-AH on MNPs makes nanoparticle system theranostic. Polymer can be used for carrying drugs and releasing them in a temperature-dependent manner. Moreover, MNPs can be used not only as contrast agents for an MRI but also for producing heat in hyperthermia therapy for cancer treatments. These characteristics make PNIPAAm-AAm-AH-coated MNPs (PMNPs) a potential candidate as theranostic agents for controlled drug delivery applications.

As discussed in the chapter 1, compared to passive targeting, active targeting mechanisms further enhance the efficacy of drug delivery vehicles. For receptor-mediated targeting, ligands such as RGD and folic acid have been extensively used to target the prostate cancer [128, 129]. RGD is specific for $\alpha_v\beta_3$ integrin molecules in tumor angiogenesis, whereas folic acid is specific to folate receptors over-expressed on tumor cells. However, these targeting ligands can find their targets in other cancer types as well. One strategy to increase the specificity of biological targets is to use a cancer-specific ligand, including cell-penetrating peptides (CPPs), to introduce drug delivery vehicle into the cell [130]. CPPs, also known as cellular delivery vehicles, can cross cell membranes, and have been extensively used for intracellular delivery of various molecules [131]. Of the commonly used CPPs, arginine-rich CPPs including HIV-Tat peptides and oligoarginines have been reported with high internalization efficacy [132]. Zhou et al. [133] has a fascinating discovery of a polyarginine peptide (R11) that showed a preferential uptake in several prostate cancer cell lines. They later compared the cellular uptake of homopolyers of L-arginine R11 peptide with various other CPPs (TAT, PENE, KALA, and L-lysine K11) by different prostate cancer cell lines (LNCaP, C4-2, LAPC4, and PC3) and found that R11 was significantly taken up by prostate cancer cells compared to those of other CPPs. These R11 peptides also demonstrate their specificity in prostates compared to other organs in animal studies [133].

In this study, R11 peptides were conjugated to PMNPs for actively targeted drug delivery for prostate cancer therapy. The nanoparticles were extensively characterized to evaluate their theranostic capabilities. We hypothesize that R11-conjugated PMNPs

(R11-PMNPs) will efficiently target prostate tumors and effectively deliver drugs to prostate cancer in a controlled fashion compared to those of non-conjugated PMNPs.

3.2 Experimental Section

3.2.1 Materials

All the chemicals were purchased from Sigma-Aldrich (St. Louis, MO) and used without further purification, if not specified. The cell lines were purchased from American Type Culture Collection (ATCC, Manassas, VA). Healthy prostate epithelial cells (PZ-HPV-7) were a kind gift from Dr. Jer-Tsong Hsieh, Department of Urology, The University of Texas at Southwestern Medical Center, Dallas, TX. Cell culture media, media supplements, and Picogreen DNA assay were purchased from Invitrogen Corp. (Carlsbad, CA).

3.2.2 Synthesis of PMNPs and R11-PMNPs

Bare MNPs were first coated with a silane-coupling agent, VTMS, by acid catalyst hydrolysis and followed by electrophilic substitution of ferrous oxide on the surface on MNPs as described in chapter 2. Further, PMNPs were synthesized using silane-MNPs as templates for PNIPAAm-AAm-AH coating as described elsewhere [134]. Briefly, silane-MNPs (28 mg) were sonicated in DI water at 50 W for 30 minutes in an ice bath. NIPAAm (100 mg), AAm (13 mg), AH (34.5 µl), *N,N'*-methylenebisacrylamide (BIS, 13 mg) and SDS (41 mg) were added to the solution while sonicating. After sonication, the reaction flask was transferred to a stir plate and

APS (78 mg) and *N,N,N',N'*-tetramethylethylenediamine (TEMED, 101 µl) were added to the reaction with vigorous stirring. The reaction was carried out under nitrogen for four hours at room temperature. The formed nanoparticles were collected by a magnet, and washed several times with DI water to remove surfactants and unreacted chemicals.

R11 peptides were conjugated to PMNPs via carbodiimide chemistry as described elsewhere [44]. In brief, R11 peptides (10 µM) were dispersed in MES buffer (0.5 ml), followed by the addition of EDC and NHS (1:1) to activate the carboxyl end groups of the R11. After one hour of stirring, the PMNPs suspended in MES (0.5 ml) were added to this solution. Finally, the conjugation was allowed to occur at room temperature for 12 hours on a revolving rotator. The R11-PMNPs were then collected using a magnet and the supernatant was collected to calculate conjugation efficiency of R11 to the PMNPs using UV-Vis spectrometer.

3.2.3 Characterization of PMNPs

Nanoparticles were characterized for their size and structure using TEM. Hydrodynamic diameter, PDI, and surface charge on the nanoparticles were characterized using zeta potential analyzer with DLS detector. Further, the iron content in the nanoparticles was evaluated using an iron assay. In addition, magnetic properties of the nanoparticles were studied using SQUID. Moreover, the LCST of the polymer and magnetic recruitment of the PMNPs were observed visually. The PNIPAAm-AAm-AH nanoparticle solution was taken in two glass tubes: one was kept at room temperature and the other was heated above the LCST of the polymer. Change in the color (cloudiness or turbidity) was recorded by taking pictures. All the sample preparations and procedures for the characterization of PMNPs were followed as described in chapter 2.

3.2.4 MRI

To study the PMNPs as contrast agents for MRI, cellular uptake study was performed using PC3 cells as described previously. After the incubation period, the cells were washed with PBS, trypsinized, and centrifuged to get a cell pellet. Nanoparticles taken up by PC3 cells were dispersed in warm agarose solution (1% w/v) and the samples were cooled quickly to 4°C. The control samples were prepared by dispersing PC3 cells only in agarose phantoms as described previously [44]. MRI was then performed as described in chapter 2.

3.2.5 In Vitro Cell Studies

The cytotoxic effects of free R11 peptides were studied on PZ-HPV-7 cells and HDFs. The cells were seeded at a density of 5000 cells/well in 96-well plates. After 24 hours of seeding, the culture medium was replaced with medium containing R11 peptides (0.1, 1, 5 and 10 μM). The cells were incubated for six and 24 hours, followed by the addition of MTS reagent. The absorbance was read at 490 nm and the percentage of relative cell survival to the control (cells exposed to media only) was estimated. Similarly, the cytotoxicity of R11-PMNPs at different concentrations (0, 50, 100, 250 and 500 μg/ml) was evaluated as described above.

To study the cellular uptake of nanoparticles, the prostate cancer cells (PC3 and LNCaP) were seeded in 48-well plates and incubated for 24 hours. The cell medium was then replaced with medium containing nanoparticles at various concentrations (0, 50, 100, 200, 300 and 500 μg/ml). After two hours of incubation, the medium was removed and cells were washed twice with PBS, followed by lysis using 1% Triton X-100 in PBS. The iron contents internalized by cells were analyzed by iron assays and normalized with the total DNA content, assessed using Picogreen DNA assays, as described in chapter 2.

3.2.6 Drug Loading and Ultrasound-mediated Drug Release

Doxorubicin hydrochloride (Dox) was chosen as a model hydrophilic anticancer drug to load into the nanoparticles. Dox is known to interact with DNA by intercalation, inhibiting the progression of topoisomerase II, which unwinds DNA for transcription [135]. Dox stabilizes the topoisomerase II complex after it has broken the DNA chain for replication, preventing the DNA double helix from being resealed, thereby stopping the process of replication. For drug loading, Dox (1 mg) was mixed with PMNPs (5 mg) in PBS (1 ml). The solution was incubated at 4°C on a revolving rotator for three days. The Dox-loaded nanoparticles (Dox-PMNPs) were then collected using a magnet and the supernatant was collected to analyze the unloaded amount of Dox using UV-Vis spectrometer at excitation wavelength of 470 nm and emission wavelength of 585 nm. This amount was then compared with the initial amount of Dox to determine the loading efficiency of the Doc, which was calculated using the equation in chapter 2.

High intensity focused ultrasound (HIFU) was used to generate temperature stimuli for the drug release from PMNPs [136]. HIFU was used in the drug release study to test the feasibility of PMNPs in releasing drugs in hyperthermia or in response to temperature changes. Briefly, after drug loading, the Dox-PMNPs were suspended in PBS (1ml) and divided in two parts, one as experimental and the other as negative control. The experimental nanoparticles (50 µl) were filled in a silicone tube, which was then placed in a piece of chicken breast by cutting it along the length. The entire sample along with chicken breast was wrapped with a parafilm to prevent water from entering the sample. The control samples were prepared in the same way as experimental samples. The HIFU system was custom prepared with the following variables: 2.5MHz fundamental frequency with 1 sec delay interval focused at a distance of 50 mm (focal length of the HIFU); duty cycle of 33% (330 msec ON and 1000 msec OFF) that generated high voltages yielding higher pressures (23 MPa) by HIFU, which is absorbed by the sample as heat (approximately 45°C). The scan area was about 0.8 × 0.2 × 0.2 inch in X, Y and Z directions, respectively, which was focused along the length of the sample. At the end of the study, the sample was taken out, placed on a magnet, and supernatant containing released Dox was collected. The Dox concentrations in the release samples and the control samples (without HIFU exposure) were calculated against the Dox standard curve.

3.2.7 In Vivo Biodistribution of Nanoparticles

Animal studies were performed in compliance with guidelines set by the University of Texas at Arlington and University of Texas Southwestern Institutional Animal Care and Use Committees. Male NOD SCID mice (6–8 weeks of age) were purchased from the University of Texas Southwestern mouse-breeding core (Wakeland Colony). Preliminary *in vivo* biodistribution studies were conducted to evaluate the tumor specificity of R11-PMNPs in comparison with PMNPs. Firstly, to test the time required for maximum accumulation of nanoparticles in prostate, PMNPs (100 µl, 5 mg Fe/kg) were injected intravenously via tail veins of mice. After 1, 4 and 24 hours post injection, the animals were sacrificed and the vital organs (kidney, liver, spleen, lung and prostate) were excised. The tissue sections were stained using Prussian blue staining to detect the presence of iron [137]. Briefly, the sections were deparaffinized and hydrated in DI water. Equal parts of HCl and potassium ferrocyanide were mixed and the sections were immersed in this solution for 20 minutes, followed by three times of washing in DI water. The sections were counterstained with nuclear fast red for five minutes, followed by two times rinsing in DI water and dehydration in the graded series of ethanol solutions. Finally, the sections were cleared in xylene twice for three minutes each, followed by imaging.

In the second step, prostate cancer orthotopic mouse models were created by injecting PC3-KD cell suspension subcutaneously (5×10^5 cells/site, injection volume 100 µl) into both flanks of the animals as described elsewhere [138]. After injection, the animals were monitored three times a week and further studies were performed when the tumors became palpable. To determine the bio-distribution and tissue-specificity of nanoparticles, saline or nanoparticles (100 μl, 5 mg Fe/kg) were injected intravenously via tail veins of the animals as previously described. After 24 hours (estimated from previous time study) of injection, the animals were sacrificed and the vital organs (kidney, liver, spleen, lung, prostate and tumor) were excised. The tissue sections were stained using Prussian blue staining.

In addition, MRI was also performed on animals before nanoparticle injection and at the end of the study using a Varian unity INOVA 7T MR system. The multislice T2-weighted images (TR = 2500 msec; TE = 60 msec; field of view of 40 mm × 40 mm; matrix = 256 × 256; slice thickness = 1 mm) were acquired with spin echo pulse sequence. Moreover, to measure the nanoparticle concentration in the animal blood, blood (15-20 μl) was drawn from the retro-orbital sinus of the animals before nanoparticle injection and at the end of the study as described elsewhere [138]. The iron content in the blood samples was then analyzed using iron assays as described in chapter 2.

3.2.8 Statistical Analysis

The results obtained were analyzed using one-way analysis of variance with $p < 0.05$ and post hoc comparisons. All the experiments were repeated multiple (at least two) times with a sample size of four (n=4). All the results were presented as mean ± SD if not specified.

3.3 Results and Discussion

3.3.1 Synthesis and Characterization of Nanoparticles

Thermo-responsive PMNPs were synthesized by radical emulsion polymerization. Figure 3.1 shows the schematic representation of synthesis of PMNPs, conjugation of R11 peptides, drug loading, and temperature-dependent drug release. TEM analysis of the nanoparticle size and structure shows that the nanoparticles were spherical in shape and approximately 100 nm in diameter (Figure 3.2). The dark core represents MNPs with polymer shell in gray. There were approximately 70 MNPs present in the core of PMNPs. The hydrodynamic diameter and PDI measured by DLS and surface charge on the nanoparticles measured by zeta potential analyzer, are represented in Table 3.1. In DLS measurement, the size of hydrated nanoparticles was larger than dehydrated nanoparticles in TEM. PMNPs had the lowest polydispersity index of 0.28, suggesting that the nanoparticles were well-dispersed and stable in the solution compared to silane-MNPs and bare MNPs. Moreover, the surface charge on the PMNPs was higher negative; thereby the repulsion among these nanoparticles is more than silane-MNPs and bare MNPs.

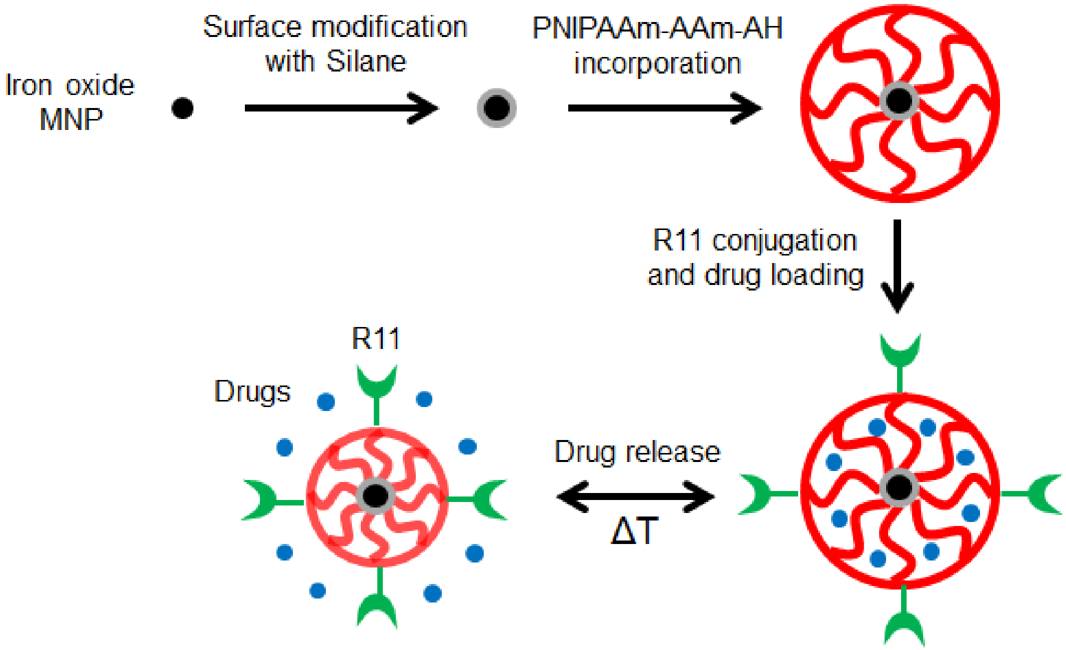

Figure 3.1 Schematic representation of PMNPs formulation with R11 conjugation and temperature-dependent drug release.

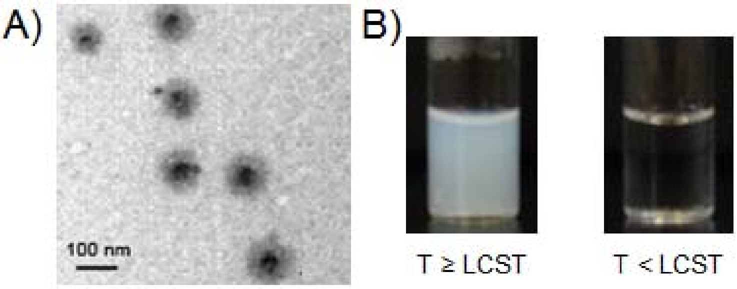

Figure 3.2 Characterization of PMNPs. (A) TEM image of 100 nm diameter sized PMNPs. (B) Phase transition of PNIPAAm-AAm-AH at LCST. The solution is cloudy when polymer is hydrophobic at temperatures above the LCST (left tube). The solution is clear when polymer is hydrophilic at temperatures below the LCST (right tube).

Table 3.1 Physicochemical characterization of PMNPs

Sample	Diameter (nm)	PDI	Zeta Potential (mV)
MNPs	10[a]	0.30	-5.1
Silane-MNPs	18[b]	0.35	-21.0
PMNPs	127	0.28	-27.0
R11-PMNPs	147	0.26	-25.7

[a]Size provided by the supplier. [b]Size obtained from TEM analysis (image not shown).

The LCST of the PNIPAAm-AAm-AH was evaluated in detail by our group previously [134]. Here, we recorded the LCST of the polymer by visual observation only (Figure 3.2). At temperatures below LCST, the polymer was hydrophilic making the solution clear. The solution turned turbid when polymer became hydrophobic at temperatures equal to or greater than the LCST (32^{o}C). The LCST behavior is due to the dehydration of the polymer chain and fluctuations in the refractive index when PNIPAAm-AAm-AH structure collapses and shrinks. Further, the R11 was conjugated to the PMNPs and R11 conjugation efficiency was evaluated. About 20% of R11 (4.2 μg) was conjugated to the PMNPs.

3.3.2 Magnetic Characterization

The iron content in the PMNPs was assessed by iron assays. As shown in Table 3.2, PMNPs had about 85% mass of iron. The PMNPs were also tested for magnetic targeting property. It was observed that the PMNPs were evenly suspended in the solution in the absence of magnetic field; however, in the presence of magnetic field, the PMNPs were recruited and concentrated to one area towards the magnet (Figure 3.3A). Moreover, superparamagnetic properties of the nanoparticles were also determined. Figure 3.3B shows the hysteresis loops of magnetization generated in the nanoparticles under the influence of applied magnetic fields. There was a slight decrease in saturation magnetization of PMNPs (52.6 emu/g) and R11-PMNPs (51.5 emu/g) compared to bare MNPs (57.9 emu/g) due to the surface modification of MNPs (Table 3.2). Nevertheless, the PMNPs and R11-PMNPs possessed strong magnetic properties. Moreover, the remanence and coercivity of PMNPs were 6.6 (M_r/M_s) and 53.9 Oe; and R11-PMNPs were 6.5 (M_r/M_s) and 53.0 Oe as compared to 6.7 (M_r/M_s) and 65.2 Oe, in case of bare MNPs, respectively. These results suggest that the PMNPs and R11-PMNPs could be classified as soft ferromagnetic substances, which have low coercive forces (< 100 Oe), small remanent magnetic induction, and long and narrow hysteresis loops [118]. The results were also consistent with the previous findings where the reduction of magnetic properties was observed when MNPs were coated with polymers such as polystyrene [116], PNIPAAm [134], PLGA [117], and PEG [111].

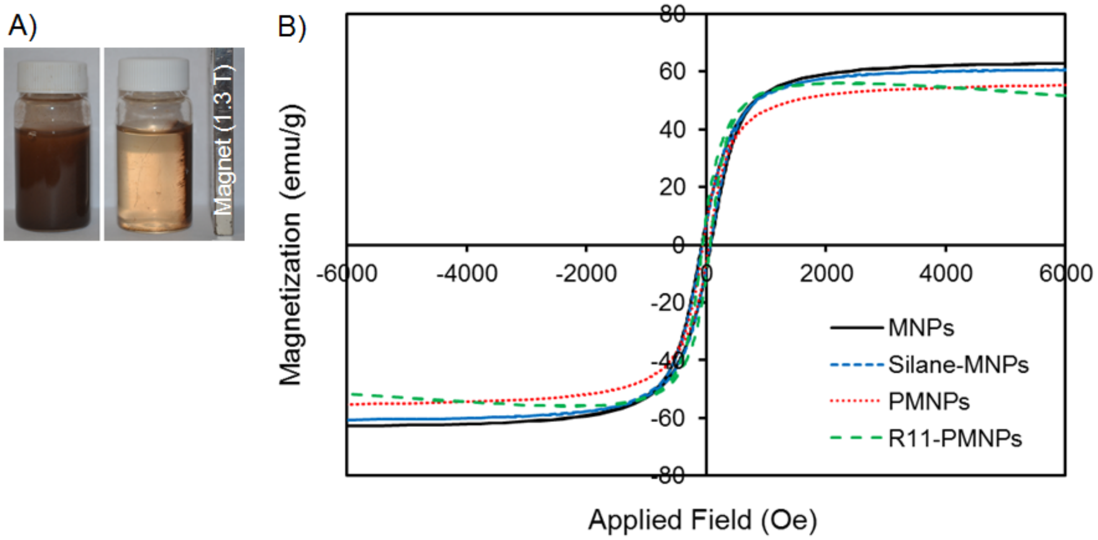

Figure 3.3 Magnetic properties of nanoparticles. (A) Photographs of PMNPs suspension in absence of magnetic field and recruitment in presence of magnetic field (1.3 T). (B) Magnetization hysteresis loops of nanoparticles showing superparamagnetic behaviors.

Table 3.2 Iron content and magnetic characterization of PMNPs

Sample	Iron (%)	Saturation Magnetization (emu/g or M_s)	Remanence (M_r/M_s)	Coercivity (Oe or H_c)
MNPs	100	57.9	6.7	65.2
PMNPs	85	52.6	6.6	53.9
R11-PMNPs	85	51.5	6.5	53.0

3.3.3 MRI

MRI was performed on agarose phantoms containing either PC3 cells alone or PMNPs taken up by PC3 cells. As shown in Figure 3.4, the PMNPs created a dark negative contrast in MRI, while no negative contrast was detected from the control samples containing PC3 cells only (Figure 3.4A). The negative contrast generated from experimental samples was dependent on the number of cells uptaken by the PMNPs. More of the cells and particles were taken up, leading to a darker signal from the samples containing a higher number of cells. The PMNPs produced a dark negative contrast signal even at a low number (1,000) of cells. These observations were in accordance with previous work in which a dark negative and dispersed contrast signal was observed by a member of our group as shown in Rahimi et al. [44] and other groups [112, 119, 139] when cells were labeled with iron oxide-based nanoparticles.

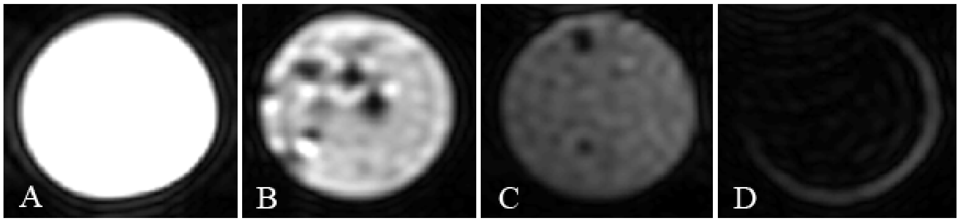

Figure 3.4 MR images of agarose phantoms containing (A) 10^3 PC3 cells, (B) 300 µg/ml PMNPs uptaken by 10^3 PC3 cells, (C) 300 µg/ml PMNPs uptaken by 10^6 PC3 cells, and (D) 300 µg/ml PMNPs uptaken by 5×10^6 PC3 cells.

3.3.4 Cytotoxicity of R11 and R11-PMNPs

Cytotoxicity of free R11 peptides was studied before conjugating it to the PMNPs. The free R11 peptides were cytocompatible at all the tested concentrations on both HDFs (Figure 3.5A) and PZ-HPV-7 cells (Figure 3.5B) even at a longer period (24 hours). There was 86.0% and 83.8% viability of HDFs and PZ-HPV-7 cells, respectively, at 10 µM concentration of R11 after 24 hours of incubation period.

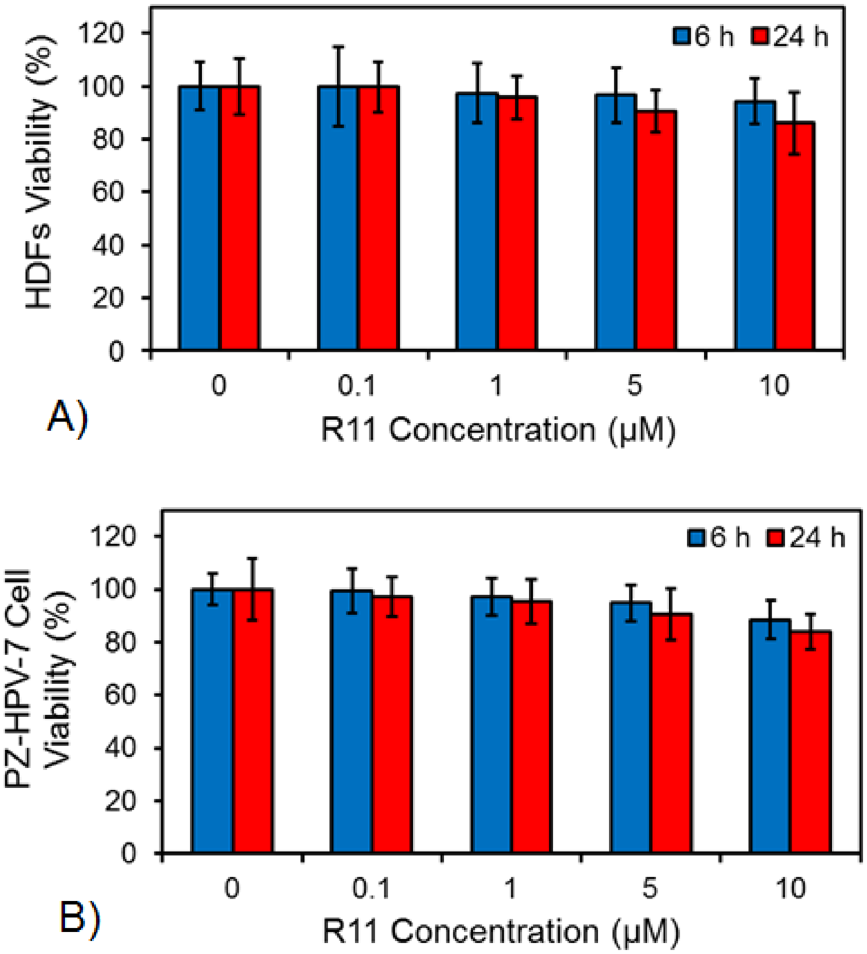

Figure 3.5 Cytotoxicity of free R11 peptides. (A) R11 was cytocompatible on HDFs and (B) PZ-HPV-7 cells after 6 and 24 hours of incubation periods compared to 100% cell viability in controls.

The R11-PMNPs also exhibited cytocompatibility on both HDFs (Figure 3.6A) and PZ-HPV-7 cells (Figure 3.6B) at all the tested concentrations at a shorter incubation time. However, the R11-PMNPs showed some level of toxicity (16% cell death) to PZ-HPV-7 cells at a high concentration of 500 μg/ml after 24 hours incubation period compared to the controls.

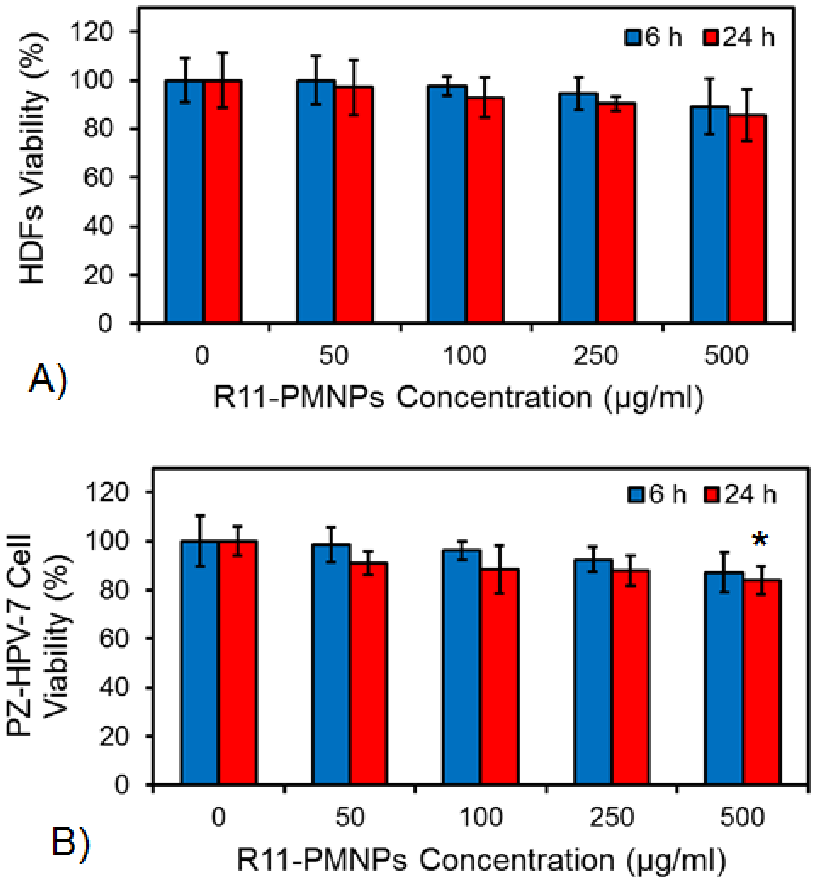

Figure 3.6 Cytotoxicity of R11-PMNPs. (A) R11-PMNPs were cytocompatible on HDFs and (B) PZ-HPV-7 cells after 6 and 24 hours of incubation periods (* $p < 0.05$).

3.3.5 Cellular Uptake of R11-PMNPs

Cellular uptake of the PMNPs and R11-PMNPs by two types of prostate cancer cells (PC3 and LNCaP) was performed to determine the optimal concentration of the nanoparticles and the difference in the nanoparticle uptake by different cell lines. As shown in Figure 3.7, the cellular uptake was nanoparticle dose-dependent as well as cell type-dependent. Compared to the PMNPs, the R11-PMNPs were taken up by both the cell types in higher amount. In general, there was a higher uptake of nanoparticles by

PSMA$^+$ LNCaP cells compared to PSMA$^-$ PC3 cells. There are many factors affecting cellular uptake of nanoparticles by various cancer cell lines and causing such differences in cellular uptake of these cancer cell lines. These factors have been discussed in chapter 2.

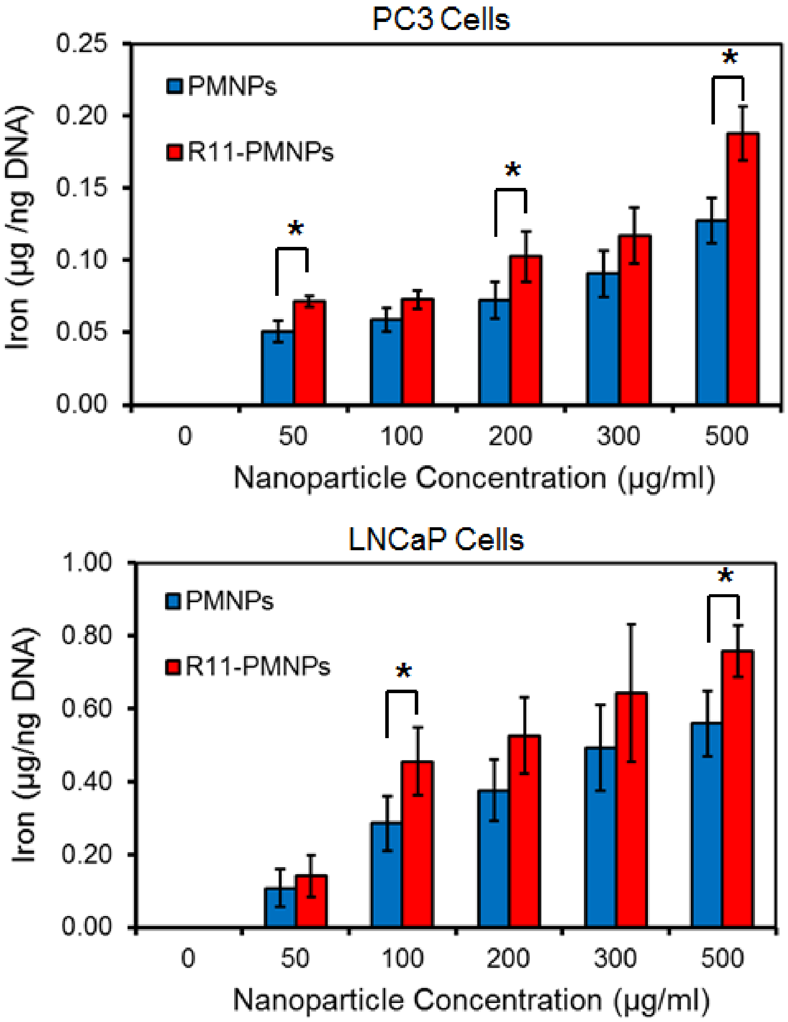

Figure 3.7 Cellular uptake of nanoparticles. Higher uptake of R11-PMNPs than PMNPs. Higher nanoparticle uptake by LNCaP cells compared to PC3 cells (* $p < 0.05$).

3.3.6 Drug Loading and Ultrasound-mediated Drug Release

HIFU was used in the drug release study because ultrasound can generate hyperthermia effect, which can be exploited in thermo-responsive drug release. The experimental set-up of ultrasound-mediated drug release is shown in Figure 3.8A. The loading efficiency of Dox in the PMNPs was about 82%. This high loading efficiency of Dox may be due to hydrophilic nature of Doxorubicin hydrochloride, which helps PMNPs retain the drugs in the polymer shell at temperatures below LCST. Further, the HIFU treatment generated temperatures till 45°C, which caused higher Dox release from the PMNPs compared to the Dox released from control samples (Figure 3.8B). About 55% Dox was released after HIFU treatment of 15 minutes, whereas only 41% Dox was released from untreated samples. Although the difference of released drugs with and without HIFU treatment is significant, the difference between two samples is only 14%. This small difference might be due to a short-time treatment with large area of HIFU scan. Due to larger scanning area compared to the area of sample may have contributed to in-effective heating of the samples. Yet we have previously found that prostate cancer cells were effectively killed even with a small difference of drug release from temperature-sensitive polymer-coated MNPs [44].

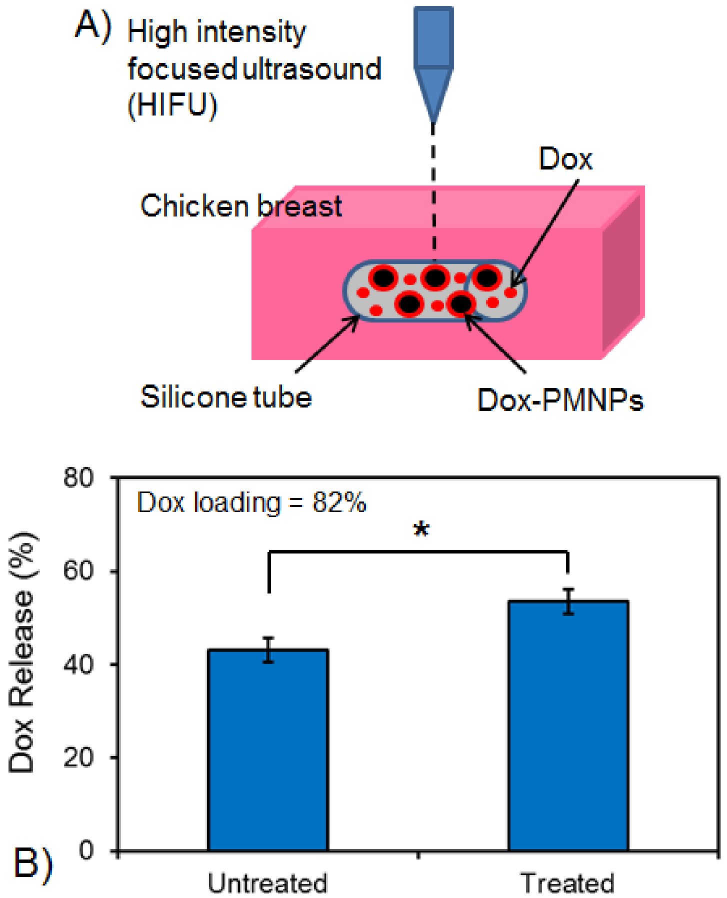

Figure 3.8 Ultrasound-mediated drug release. (A) Experiment set-up showing HIFU and placement of sample in chicken breast. (B) Higher release of Dox in HIFU treated (15 minutes) samples compared to untreated samples (* $p < 0.05$).

HIFU was chosen in the experiment because it can be used for hyperthermia treatment *in vivo* as well. Moreover, ultrasound can enhance the intercellular uptake of drugs not only by breaking the tight junction between cells, but also by acoustically enhancing the permeability of the cell membrane [140], thereby making induced endocytosis of Dox-PMNPs possible.

3.3.7 In Vivo Biodistribution of Nanoparticles

Biodistribution of PMNPs was performed on animals without tumors to evaluate time-dependent accumulation of PMNPs in prostate. Figure 3.9A shows PMNPs accumulation in the prostate. From the blue iron staining, it was observed that the PMNPs were accumulated in prostate even after one hour post i.v. injection, which was then increased to 24 hours. Therefore, in the later studies, the duration of 24 hours post i.v. injection was kept constant. Further, biodistribution and tumor targeting of R11-PMNPs was studied in comparison with PMNPs and saline. As shown in Figure 3.9B, the R11-PMNPs accumulated in tumors in a significantly higher amount compared to that of other vital organs such as the spleen, liver, prostate, and kidney. Most of the PMNPs were taken up by the spleen and very few by the tumor. The amount of R11-PMNPs in tumors was significantly higher than that of PMNPs.

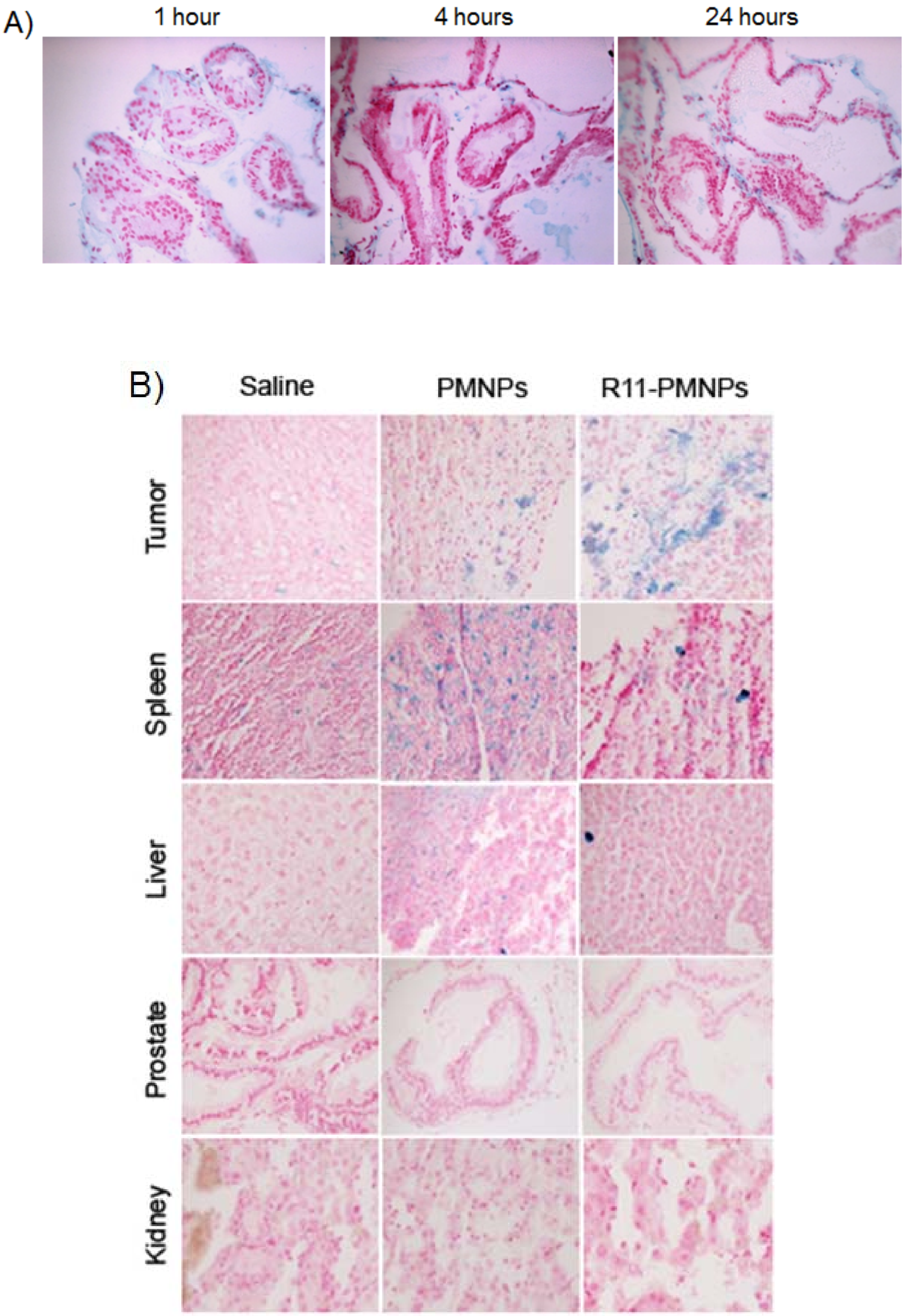

Figure 3.9 Prussian blue staining of tissue sections showing biodistribution of nanoparticles. (A) PMNPs taken up by prostate after 1, 4 and 24 hours. (B) Higher accumulation of R11-PMNPs in tumor compared to PMNPs and saline after 24 hours i.v. injection.

MRI on animals was also performed before and after 24 hours of nanoparticle adminstration. It was clearly observed that R11-PMNPs created a dark negative contrast in the tumor regions after 24 hours, confirming their accumulation in the tumor (Figure 3.10A). Moreover, in case of R11-PMNPs, T2 signal intensity in tumor regions was dropped by 30% compared to 0% in case of PMNPs (Figure 3.10B). These results confirm the tumor specificity of R11-PMNPs by showing a significantly darker negative contrast in tumor regions compared to that of PMNPs. Moreover, the blood samples, collected from the retro-orbital sinus of the animals before nanoparticle injection and at the end of the study, were analyzed to measure the blood iron content. The blood iron content before nanoparticle injection was subtracted from the blood iron content after 24 hours of injection. About 32% and 14% iron was observed in the blood in case of PMNPs and R11-PMNPs, respectively. This result might support the tumor-specificity of R11-PMNPs that more of R11-PMNPs were recruited at the tumor site, thereby less of R11-PMNPs in the blood circulation compared to those of PMNPs.

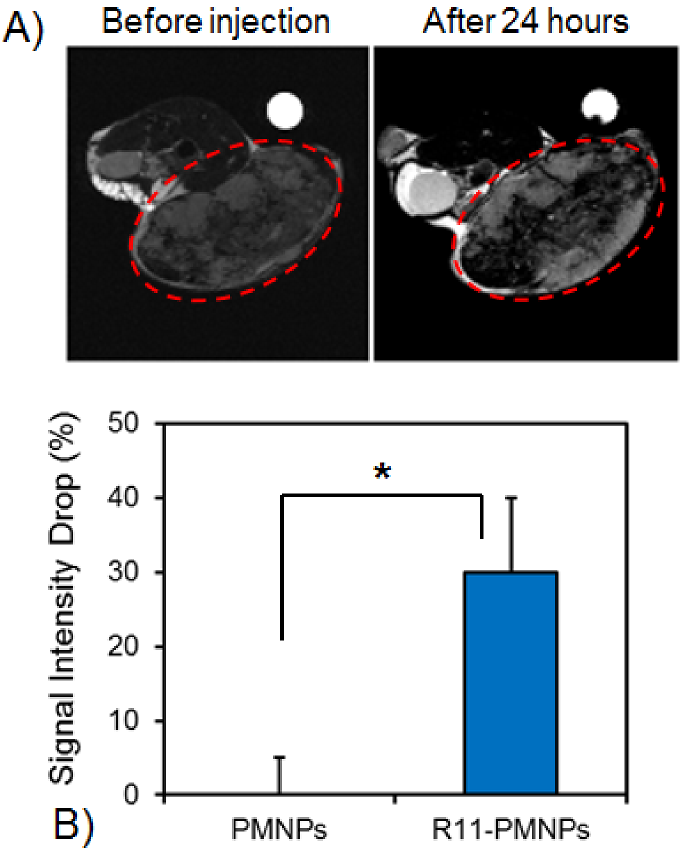

Figure 3.10 MR imaging of tumors. (A) A dark negative contrast in tumor regions generated from accumulation of R11-PMNPs. (B) Significant drop in MRI signal intensity with R11-PMNPs compared to PMNPs (*$p < 0.05$).

3.4 Summary

In summary, we successfully evaluated the efficacy of thermo-responsive R11-PMNPs for tumor-specific targeting, MRI and temperature-dependent drug release. The superparamagnetic properties of bare MNPs were preserved even after polymer coatings and R11 conjugation. R11 and R11-PMNPs were highly cytocompatible with the normal healthy cells and were efficiently taken up by the cancer cells. HIFU was capable of producing heat that caused higher release of Dox from R11-PMNPs compared to the controls. Moreover, *in vivo* biodistribution and tumor-specific targeting studies revealed that R11-PMNPs accumulated specifically in tumor regions and generated a dark negative contrast in MRI. Future work involves *in vivo* prostate cancer treatment using hyperthermia and temperature-dependent drug release.

CHAPTER 4

THERMO-RESPONSIVE FLUORESCENT POLYMER-COATED MNPs

4.1 Introduction

Despite the numerous advantages of nanoparticles, their applications in imaging and drug delivery are affected by not only their size-dependent properties but also their surface modification. Recently developed multifunctional DICT-NPs are degradable, but suffer reduced fluorescence intensity compared to pure BPLP nanoparticles. This problem was associated with the two possible reasons: 1) the dark MNPs absorb excited/emitted light, decreasing the fluorescence from BPLP; and 2) BPLP coating on MNPs is not strong enough due to the emulsion process. On the other hand, the thermo-responsive PMNPs suffer clearance problems due to non-degradable nature of the PNIPAAm-AAm-AH, but the binding of the polymer to MNPs is very strong due to the covalent attachment of the polymer to the MNPs surface.

We hypothesized that a copolymer of BPLPs and PNIPAAm-AAm-AH would be degradable and enhance the fluorescence from BPLP. Moreover, this copolymer will have characteristics of both polymers such as fluorescent and thermo-responsive. As discussed in chapter 3, PNIPAAm-AAm-AH is hydrophilic and clear at temperatures below LCST, thus the fluorescence property of BPLP will be maintained, whereas PNIPAAm-AAm-AH becomes cloudy at temperatures higher than the LCST, when the fluorescence from this copolymer may be hampered. This phenomenon of temperature-dependent fluorescence can also be of great interest in the biomedical and non-biomedical fields.

The aim of this work was to synthesize a novel thermo-responsive fluorescent polymeric (TFP) and decorate it on the surface of MNPs to formulate TFP-MNPs for prostate cancer imaging and therapy. Most surface modifications of nanoparticles for imaging applications are based on chemical incorporation since it offers a stronger and more robust bond and a more stable surface ligand, compared with physical adsorption. Appropriate encapsulation of nanoparticles results in better stability and preservation of optical properties. Therefore, we performed several pilot studies to optimize the chemicals and the protocol. From the pilot studies, we eliminated AAm and used WBPLP instead of BPLP. The role of hydrophilic AAm was to increase the LCST of PNIPAAm, which was fulfilled by hydrophilic WBPLP.

4.2 Experiment Section

4.2.1 Synthesis of TFP Nanoparticles and TFP-MNPs

Firstly, WBPLP was conjugated with AH using carbodiimide chemistry. In brief, WBPLP (45 mg) was dissolved in MES buffer (5 ml), followed by the addition of EDC and NHS (1:1). After 30 minutes of mixing on a rotary revolver, AH (18.75 µl) was added and the reaction was continued for 12 hours at room temperature. The WBPLP-AH copolymer was then dialyzed using 500 Da molecular weight cut-off dialysis membranes for 24 hours to remove the unreacted chemicals.

TFP nanoparticles were synthesized by a free radical polymerization reaction. Briefly, the purified WBPLP-AH solution (5 ml) and NIPAAm (45 mg) were dissolved in DI water (25 ml). BIS (5.85 mg) and SDS (17.4 mg) were added to the mixture while continuously stirring under nitrogen for 30 minutes. APS (52.48 mg) and TEMED (69 µl) were then added and the reaction was stirred for four hours under nitrogen at room temperature. After four hours, the nanoparticle solution was dialyzed using 3500 Da molecular weight cut-off dialysis membranes for 24 hours to remove free surfactants and unreacted chemicals.

Finally, TFP-MNPs were synthesized using silane-MNPs as templates for TFP coating as described in chapter 3. Briefly, silane-MNPs (10 mg) were sonicated in DI water (25 ml) at 50 W for 30 minutes in an ice bath. The purified TFP (WBPLP-AH, 5 ml) from first step, NIPAAm (45 mg), BIS (5.85 mg) and SDS (17.4 mg) were added to the solution while sonicating. After sonication, the reaction flask was transferred to a stir plate, and APS (52.48 mg) and TEMED (69 µl) were added to the reaction with vigorous stirring. The reaction was carried out under nitrogen for four hours at room temperature. The TFP-MNPs were collected by a magnet, and washed several times with DI water to remove surfactants and unreacted chemicals.

4.2.2 Characterization of TFP Nanoparticles and TFP-MNPs

Nanoparticles were characterized for their size and structure using TEM. Hydrodynamic diameter, PDI, and surface charge on the nanoparticles were characterized using zeta potential analyzer with DLS detector. The LCST of the TFP nanoparticles and magnetic recruitment of the TFP-MNPs were characterized. Chemical characterization of the nanoparticles was performed using FTIR. Further, the iron content in the nanoparticles was evaluated using iron assays. The cytotoxicity effects of TFP-MNPs were studied on HDFs for 12 and 24 hours using MTS assays. All the sample preparations and procedures for the characterization of TFP nanoparticles and TFP-MNPs were followed as described in chapters 2 and 3.

4.2.3 Fluorescence and Temperature-dependent Fluorescence

The fluorescence from the nanoparticles was observed in UV light and compared against the fluorescence in white light. The positive control sample contained WBPLP solution and negative control sample contained PNIPAAm-AH solution. Further, temperature-dependent fluorescence was also estimated to investigate the effect of temperature on the fluorescence intensity of the nanoparticles. Briefly, the TFP nanoparticles (3 mg/ml) in a tube were immersed in a water tank that was heated using a temperature controller. The sample was excited with a blue laser (473 nm) and the emitted light was passed through a 532 nm long pass filter. The fluorescence intensity was recorded as voltage read out from a high-speed digital oscilloscope. The measurements were taken at temperatures ranging from 25°C to 45°C with a step of 0.5°C. The fluorescence intensities of these measurements were then converted to the percentage loss in the fluorescence intensity as a function of temperature.

4.2.4 Degradation, Drug Loading and Release

To study the degradation of the TFP shell, TFP-MNPs were suspended in DI water and incubated at 37°C over a time range. At each time point, nanoparticles were collected by a magnet, and dry weight of the nanoparticles was recorded. A relative percentage of dry weights of the nanoparticles at all the time points were calculated with respect to the initial dry weight of the nanoparticles. For drug loading and release studies, the Dox was loaded in the TFP-MNPs as described in chapter 3. The Dox-TFP-MNPs were then suspended in PBS and incubated at 25°C, 37°C, and 41°C on a rotating revolver. At each predetermined time point, the sample was taken out and placed on a magnet so that supernatant containing released Dox was collected. The Dox concentrations in the release samples were calculated against the Dox standard curve.

4.2.5 In Vivo Fluorescence Imaging

Animal models were prepared as described in chapter 2. BPLP-MNPs (100 µl of 5 mg Fe/kg), TFP-MNPs (100 µl of 5 mg Fe/kg), and TFP nanoparticles (100 µl of 3 mg/ml) were injected in tumors by intra-tumoral injections. BPLP-MNPs were used as control nanoparticles. The animals were then sacrificed immediately after nanoparticle injections and imaged using an in vivo Kodak imaging system (Carestream Health Inc., Rochester, NY). The relative fluorescence intensity from the tumors injected with nanoparticles was calculated by subtracting the fluorescence intensity of ഌ梛□嗥脈砒 醸 鞀 鞅 ഌ桨□嗥脈砒 醸 鞀 鞅 ڂ ☐ ٦ȣ 梛□嗥脈砒 醸 鞀 鞅 ∀es.

4.2.6 Statistical Analysis

The results obtained were analyzed using one-way analysis of variance with $p < 0.05$ and post hoc comparisons. All the experiments were repeated multiple (at least two) times with a sample size of four (n=4). All the results were presented as mean ± SD if not specified.

4.3 Results and Discussion

4.3.1 Characterization of TFP Nanoparticles

TFP nanoparticles were synthesized by radical emulsion polymerization. Figure 4.1 shows the TEM and LCST of the TFP nanoparticles. The spherical TFP nanoparticles (Figure 4.1A) were approximately 150 nm in diameter as measured by DLS (Table 4.1). The PDI and surface charge on the TFP nanoparticles was 0.28 and -13.4 mV, respectively. The LCST of the TFP nanoparticles was evaluated using UV-Vis spectrometer and visual observation (Figure 4.1B), which was about 39°C. At temperatures below LCST, the polymer was hydrophilic, making the solution clear. The solution turned turbid when polymer became hydrophobic at temperatures equal to or greater than the LCST. This result confirms the thermo-responsive behavior of TFP nanoparticles even after copolymerization of the temperature-sensitive polymer PNIPAAm-AH with the biodegradable fluorescent polymer WBPLP.

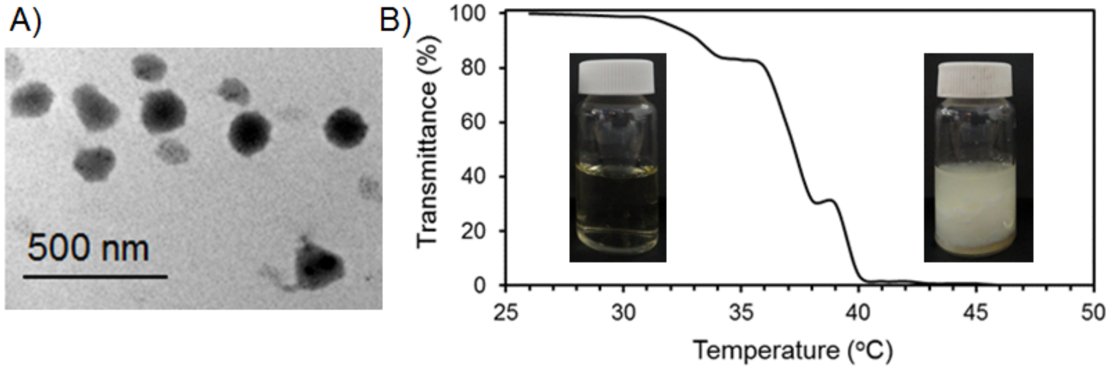

Figure 4.1 Characterization of TFP nanoparticles. (A) TEM image of TFP nanoparticles. (B) Phase transition of TFP nanoparticles at LCST (39°C).

Table 4.1 Physicochemical characterization of TFP NPs and TFP-MNPs

Sample	Diameter (nm)	PDI	Zeta Potential (mV)	Iron (%)
MNPs	10[a]	0.30	-5.1	100
Silane-MNPs	18[b]	0.35	-21.0	__
TFP NPs	150	0.28	-13.4	__
TFP-MNPs	135	0.07	-31.0	75

[a] Size provided by the supplier. [b] Size obtained from TEM analysis (image not shown).

4.3.2 Fluorescence Properties of TFP Nanoparticles

Fluorescence properties of TFP nanoparticles were tested under UV light. Figure 4.2A shows that there was no fluorescence from the samples under white light. However, there was a bright fluorescence observed from WBPLP and TFP nanoparticles under UV light. The control sample containing PNIPAAm-AH did not show the fluorescent property in any condition, whereas the TFP nanoparticles demonstrate the fluorescence under UV light, suggesting that the TFP nanoparticle fluorescence was solely due to the presence of WBPLP.

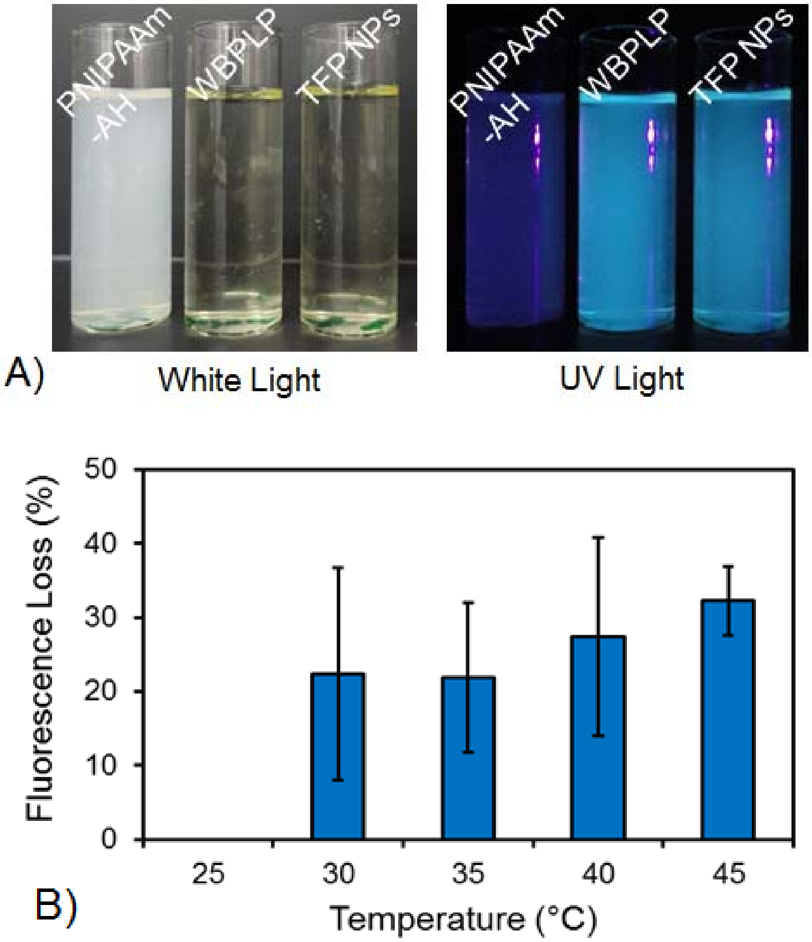

Figure 4.2 Fluorescence characterization of TFP nanoparticles. (A) Photographs of samples in white light and UV light. Fluorescence from WBPLP and TFP nanoparticles was observed in UV light only. (B) Temperature-dependent fluorescence of TFP nanoparticles showing fluorescence loss at increasing temperatures.

Moreover, a temperature-dependent fluorescence was also tested. It was observed that the mean fluorescence intensity of TFP nanoparticles decreased gradually as the temperature increased; however, there was no statistically significant difference among the fluorescence intensities at increasing temperatures (Figure 4.2B). The fluorescence photobleaching effect was also tested at 23.5°C and 41.5°C. Even after more than 10 minutes of continuous laser excitation, no photobleaching was observed and the fluorescence intensity remained stable.

4.3.3 Characterization of TFP-MNPs

The hydrodynamic diameter, PDI and surface charge on the TFP-MNPs were 135 nm, 0.07 and -31.0 mV, respectively (Table 4.1). TFP-MNPs were well-dispersed and stable in the solution. The formation of TFP-MNPs was also confirmed by FTIR, which showed the characteristic peaks of Fe-O at 700 cm^{-1}, $–CH_2$ from polymer backbone at 2919 cm^{-1}, –C=O from citric acid at 1900 cm^{-1}, –C(=O)NH between WBPLP and amino acid at 1550 cm^{-1}, and N-H from primary and secondary amines of PNIPAAm and AH (Figure 4.3). These findings were in agreement with our previous observations confirming the presence of MNPs [107] and all the corresponding bonds from WBPLP and PNIPAAm coatings [101, 134]. Further, degradation of the TFP coating on MNPs in DI water was studied over time. It was observed that the TFP coating started degrading with 31% polymer weight loss in first four days (Figure 4.4). The degradation rate was then reduced, which resulted in 37% polymer weight loss after 13 days. The reduction in the degradation rate was due to the presence of PNIPAAm and AH, slowing down the hydrolysis of the WBPLP. It is speculated that the TFP degradation will take longer than that of WBPLP alone.

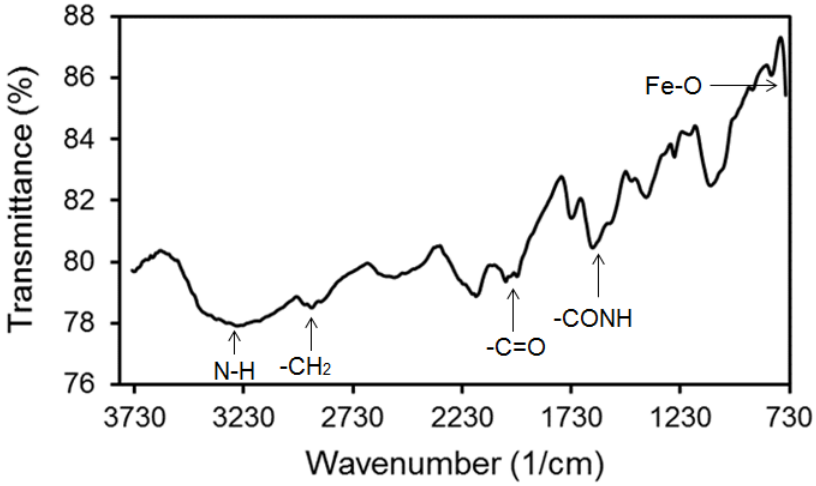

Figure 4.3 FTIR spectrum of TFP-MNPs with arrows pointing the peaks associated to the bonds in polymer backbone and MNPs.

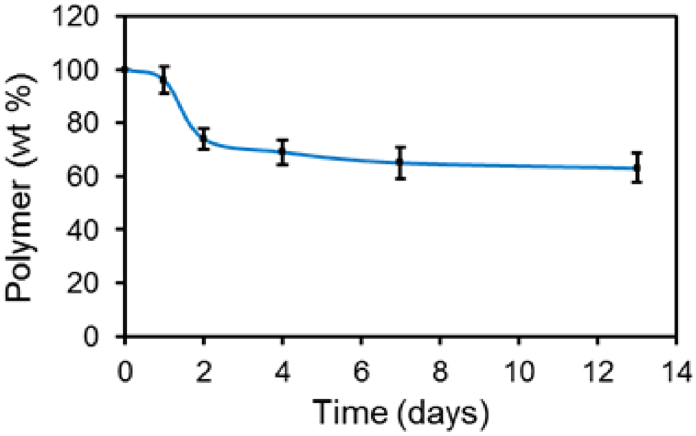

Figure 4.4 Degradation profile of TFP coatings on MNPs showing 37% polymer weight loss in 13 days.

The nanoparticles possess strong magnetic properties. The TFP-MNPs were comprised of approximately 75% mass of iron (Table 4.1). Moreover, in the absence of a magnet, nanoparticles were suspended and well-dispersed in DI water (Figures 4.5A). In the presence of a magnet, nanoparticles concentrated toward the magnet, demonstrating the recruitment of nanoparticles via magnetic targeting. Cytotoxicity of the TFP-MNPs was tested on HDFs for their survival. It was observed that TFP-MNPs were cytocompatible at all the tested concentrations on HDFs after 12 hours of incubation (Figure 4.5B). However, after 24 hours of exposure, the TFP-MNPs showed some level of toxicity, 27% cell death at a high concentration of 500 µg/ml compared to the controls.

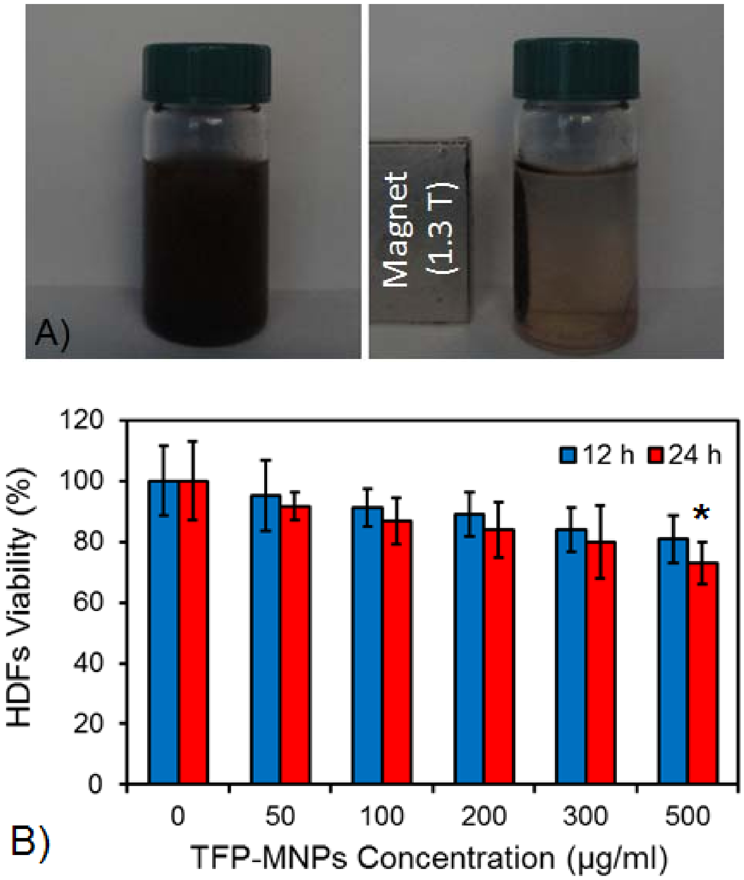

Figure 4.5 Magnetic recruitment and cytotoxicity of TFP-MNPs. (A) Photographs showing nanoparticle suspension in absence of magnetic field and recruitment of nanoparticles in the magnetic field (1.3 T) generated by a magnet. (B) Cytotoxicity of TFP-MNPs on HDFs after 12 and 24 hours of incubation periods (* $p < 0.05$).

4.3.4 Drug Loading and Release

The loading efficiency of Dox in the TFP-MNPs was approximately 90%, which was higher than Dox loading in PMNPs (82%). The higher loading of Dox in TFP-MNPs might be due to either the interaction between Dox and TFP or more swelling of TFP at temperature below the LCST while drug loading. A temperature-dependent biphasic Dox release was observed (Figure 4.6). Dox was released in a significantly higher amount at 41°C (temperature < LCST of TFP) compared to that of 37°C and 25°C. There was no difference between Dox release at 37°C and 25°C, both temperatures were below the LCST of TFP. These observations indicate that the Doc release of the TFP-MNPs was temperature-dependent.

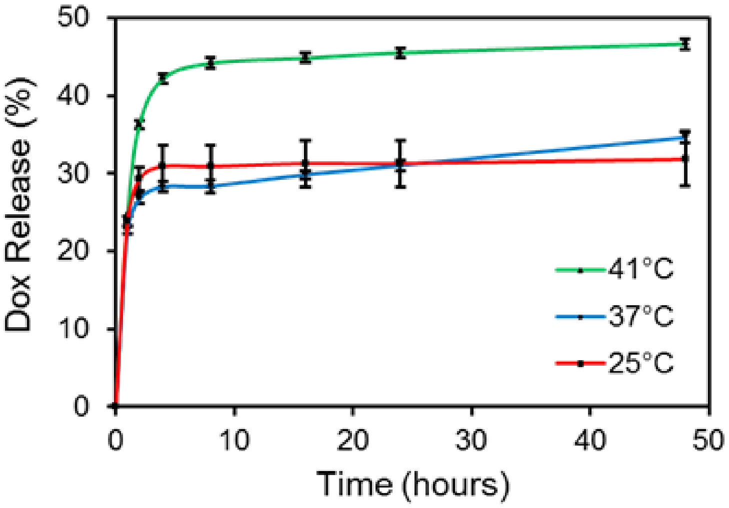

Figure 4.6 Temperature-dependent Dox release kinetics showing higher release of Dox at 41°C compared to 37°C and 25°C.

4.3.5 In Vivo Fluorescence Imaging

In vivo fluorescence imaging was performed after intra-tumoral injections of nanoparticles. As shown in Figure 4.7A, no fluorescence was observed from the control tumors (without nanoparticle injections). A bright fluorescence was detectable from the experimental tumors after intra-tumoral injections of the nanoparticles. Moreover, TFP nanoparticles generated the fluorescence with the highest intensity, which was then reduced significantly for TFP-MNPs due to the presence of dark MNPs (Figure 4.7B). However, the fluorescence intensity from TFP-MNPs was significantly higher than that of BPLP-MNPs, which may be due to the covalent bonding of TFP to the MNP surface compared to physical adsorption of BPLP on the MNP surface. These results show that the TFP-MNPs can overcome the limitation of reduced fluorescence from BPLP-MNPs.

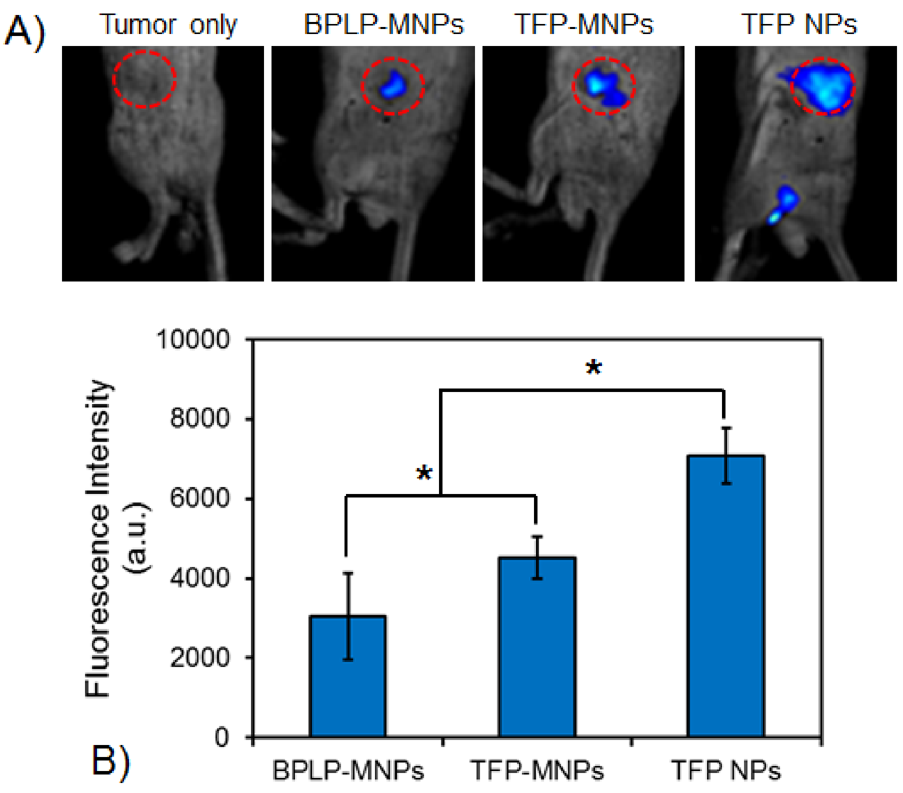

Figure 4.7 In vivo fluorescence imaging. (A) Fluorescence from nanoparticles injected in tumors. (B) Relative fluorescence intensities from the nanoparticles injected in tumors (* $p < 0.05$).

4.4 Summary

In summary, we successfully developed novel thermo-responsive fluorescent polymeric nanoparticles and coated MNPs surface with this polymer. The TFP-MNPs had the multifunctional capabilities, the fluorescent and temperature-sensitive properties of both DICT-NPs and PMNPs. TFP-MNPs were degradable that eliminate long-term toxicity concerns and bypass the size limitations for *in vivo* clearance in the traditional nanoparticle designs. The thermo-responsiveness of the PNIPAAm-AH was preserved after copolymerization with WBPLP. The fluorescence imaging studies revealed that

TFP and TFP-MNPs are capable of optical imaging and releasing drugs in biphasic manner. Finally, these cytocompatible nanoparticles also exhibited bright fluorescence *in vivo* compared to that of BPLP-MNPs developed in chapter 2.

CHAPTER 5

CONCLUSION AND FUTURE OUTLOOK

5.1 Summary

The aim of this research project was to develop magnetic-based multifunctional theranostic nanoparticle designs for prostate cancer imaging and treatment. We developed three nanoparticle designs with dual-targeting, dual-imaging, and dual-treatment capabilities to provide better tools and carriers for targeted and controlled release of drugs to the prostate cancer. Firstly, we developed cancer cell-selective biodegradable photoluminescent polymer-coated MNPs that overcome the drawbacks of long-term toxicity of QDs and poor photostability of organic dyes. Secondly, we developed prostate cancer-specific thermo-responsive polymer-coated MNPs by conjugating R11 peptides to open a new route for prostate cancer targeted therapy. Finally, we developed novel thermo-responsive fluorescent polymer-coated MNPs by combining functionalities/advantages of the earlier two designs. Such biodegradable, thermo-responsive, and fluorescent polymers will fill gaps in the biological and non-biological applications of the materials. These multifunctional theranostic nanoparticles will effectively target, image and treat the prostate cancer by reducing complications associated with conventional techniques and saving many lives of prostate cancer patients. However, while developing novel and effective nanoparticle systems, certain design considerations and critical issues need to be taken into account.

All of our three designs of MBTN have dual-imaging capabilities. Dual- or multi-modal imaging systems bearing the advantages of specific individual imaging modalities may overcome the limitations associated with the stand-alone systems. For instance, MRI provides exceptional tissue contrast, penetration depth, and high spatial resolution, whereas fluorescence imaging provides extremely high sensitivity. A dual-imaging modality combining MRI contrast and fluorescent agents will be able to diagnose cancers in early stages pre-operatively and intra-operatively with better accuracy. Our MBTN can be used before surgery for MRI to locate the tumors as well as during the surgery for optical imaging to confirm the complete removal of the tumors. The optical imaging will have to be used during the surgery due to the limitations associated with the deep tissue fluorescence imaging. Therefore, we foresee the applications of our MBTN as supplementary tools to the existing technologies for prostate cancer management.

5.2 Limitations and Future Work

For the successful implementation of our MBTN, some of the limitations need to be overcome and some of the hypotheses need to be tested. In case of DICT-NPs, we observed an interesting cell-selective cellular uptake of the nanoparticles. The difference in the nanoparticle uptake by two different cancer cell lines may be due to the effects of hydrophilicity levels of polymers and different metabolic mechanisms of different cells. It can also be attributed to the different cell surface antigens on different cells and their interactions with biomaterials. Hydrophobic BPLP-MNPs have been uptaken more by PSMA$^+$ LNCaP cells while hydrophilic WBPLP-MNPs by PSMA$^-$ PC3 cells, making both types of nanoparticles relatively specific for a particular prostate cancer cell line. One of the hypotheses is that the PSMA marker might be involved in the cell-selective uptake of the nanoparticles. The hypothesis of PSMA markers being responsible for the difference in the cellular uptake of nanoparticles can be studied by cleaving, suppressing, or blocking the PSMA markers on the cells. The PSMA markers on the LNCaP cells can be cleaved using certain enzymes, suppressed using siRNA transfection, or blocked using anti-PSMA antibodies. Later, the nanoparticles uptake by active PSMA$^+$ LNCaP cells and inactive PSMA$^+$ LNCaP cells can be studied to see if there is any difference in the extent of nanoparticles uptake by these two cell lines. Testing this hypothesis, however, is our future goal.

Our PMNPs are not completely degradable. We are copolymerizing PNIPAAm with other degradable polymers to make a degradable polymer shell. As an effort to achieve this aim, we have copolymerized PNIPAAm with acrylic acid, chitosan, or WBPLP. The copolymer of PNIPAAm and WBPLP was discussed as part of aim 3 of this research. Further, we tested the *in vivo* biodistribution of PMNPs and R11-PMNPs and observed that R11-PMNPs were accumulated in the tumor region in higher amount than that of PMNPs. We plan to quantify the iron uptake by the tumor and other tissues using iron assays. Briefly, iron can be isolated from the tissues after the enzymatic digestion of the organs. Iron assays can be performed on these samples and compared against the iron standards to quantify the amount of iron present in each organ tissue. Moreover, we plan to study the *in vivo* therapeutic efficacy of drug-loaded PMNPs.

Briefly, the drug-loaded nanoparticles will be injected in the tumors of mice and HIFU will be exposed to cause hyperthermia and the drug release from the nanoparticles. The tumor weights and volumes will be measured to assess the effectiveness of the treatment.

Additionally, we plan to perform a factorial analysis study on TFP-MNPs to evaluate the effects of factors such as concentrations of WBPLP and PNIPAAm on the LCST and fluorescence intensity. Extensive magnetic characterization and *in vitro* cell studies will also be performed before testing the nanoparticles in small animals. Finally, *in vivo* theranostic effectiveness of the TFP-MNPs will be studied in comparison with DICT-NPs and PMNPs.

Although MBTN have gained increased attention for biological applications, it is critical to obtain more understanding on particle size control, *in vivo* particle toxicity, degradation, distribution, and intracellular trafficking before it can move to clinical applications. The FDA had approved the use of MNPs as MRI contrast agents in humans due to their benign nature *in vivo*. The MNPs can be made more biocompatible by coating them with FDA-approved biocompatible polymers like PEG, PLA, dextran, and silica. However, the approval of superparamagnetic iron oxide nanoparticle (SPION)-based agents have been withdrawn due to their allergic or hypersensitivity reactions to parenteral iron, toxic polymer coating, or iron-polymer preparations (Table 5.1). Further, manganese (Mn) and gadolinium (Gd)-based MRI contrast agents, such as multifunctional MnO and PEG functionalized Gd_2O_3 nanoparticles, have also been researched for *in vitro* and *in vivo* imaging applications. Several of Gd-based MRI contrast agents have been approved by the FDA for human use. Therefore, we plan to test Gd-based agents for our applications and replace iron oxide MNPs with Gd-based agents.

Table 5.1 Current status of MRI contrast agents

Material	Commercial name	Application	Status
SPION	Feridex IV	Liver MRI	Withdrawn
SPION	Resovist	Liver MRI	Withdrawn
SPION	Combidex	Prostate cancer lymph node metastases MRI	Withdrawn
SPION	Feraheme	Iron deficiency anemia treatment	Pending
SPION	Lumirem	MRI of Gastrointestinal lumen	Withdrawn
SPION	Clariscan	MR angiography, tumor microvasculature MRI	Development discontinued
Gd	Omniscan	Cranial and spinal MRI	Approved
Gd	Multihance	MRI contrast agent	Approved
Gd	Magnevist	MRI of blood vessels and intracranial lesions	Approved
Gd	Prohance	MRI of central nervous system	Approved
Gd	Vasovist	MR angiography agent	Approved
Gd	OptiMARK	Brain, spine, liver MRI	Approved
Gd	Eovist	Liver MRI	Approved

Furthermore, magnetic properties of MBTN are associated with the chemical composition, size, and morphology of the particles. For the efficient use of MBTN in targeting, imaging, and therapy, the particle size should be appropriate to allow attraction by magnetic field, and the strength of magnetic field should be considerably strong in order to localize particles in the desired area. *In vivo* degradation of MBTN is mainly dependent on the dissociation of MNPs and the degradation of polymer coatings. Therefore, the polymer of choice should be highly biocompatible and biodegradable to avoid toxic effects to the other healthy organs. The chosen polymer should also provide functional groups for conjugation of targeting ligands to make MBTN cancer-specific. Further, understanding of the relaxivity of MBTN is highly essential for MRI and hyperthermia applications. Relaxivity is dependent not only on magnetic properties but also on the applied magnetic field strength, temperature, and the medium in which the measurements are carried out. Equally as important, advances in imaging and diagnostic tools are also critical to realize the full potential of MBTN for disease management. Impressive developments in the nanotechnology and biomaterials fields have provided numerous tools and techniques to manipulate the nanoparticle properties. With the increasing rate of advances in these fields and the success of MNP-based nanoparticles in biomedical field, the clinical use of MBTN can be foreseen.

REFERENCES

[1] American Cancer Society: Prostate cancer. 2012 [cited; Available from: www.cancer.org/Cancer/ProstateCancer/DetailedGuide/prostate-cancer-key-statistics

[2] Jani AB, Hellman S. Early prostate cancer: clinical decision-making. Lancet. 2003 Mar 22;361(9362):1045-53.

[3] National Cancer Institute: Prostate cancer. 2012 [cited; Available from: www.cancer.gov/cancertopics/types/prostate

[4] Smart R. PSA testing and DRE, TRUS scanning with sector biopsy, improved histology, curative treatments, and active surveillance for prostate cancer: a success story for men's health. The New Zealand medical journal. 2008 Dec 12;121(1287):57-68.

[5] Hochreiter WW. The issue of prostate cancer evaluation in men with elevated prostate-specific antigen and chronic prostatitis. Andrologia. 2008 Apr;40(2):130-3.

[6] Pinthus JH, Pacik D, Ramon J. Diagnosis of prostate cancer. Recent results in cancer research Fortschritte der Krebsforschung. 2007;175:83-99.

[7] Patel AR, Jones JS. Optimal biopsy strategies for the diagnosis and staging of prostate cancer. Current opinion in urology. 2009 May;19(3):232-7.

[8] Hillier SM, Maresca KP, Femia FJ, Marquis JC, Foss CA, Nguyen N, et al. Preclinical evaluation of novel glutamate-urea-lysine analogues that target prostate-

specific membrane antigen as molecular imaging pharmaceuticals for prostate cancer. Cancer research. 2009 Sep 1;69(17):6932-40.

[9] Harisinghani MG, Barentsz J, Hahn PF, Deserno WM, Tabatabaei S, van de Kaa CH, et al. Noninvasive detection of clinically occult lymph-node metastases in prostate cancer. New England Journal of Medicine. 2003 Jun 19;348(25):2491-U5.

[10] Zhang Y, Saylor M, Wen S, Silva MD, Rolfe M, Bolen J, et al. Longitudinally quantitative 2-deoxy-2-[18F]fluoro-D-glucose micro positron emission tomography imaging for efficacy of new anticancer drugs: a case study with bortezomib in prostate cancer murine model. Mol Imaging Biol. 2006 Sep-Oct;8(5):300-8.

[11] Gao X, Cui Y, Levenson RM, Chung LW, Nie S. In vivo cancer targeting and imaging with semiconductor quantum dots. Nature biotechnology. 2004 Aug;22(8):969-76.

[12] Liu L, Zhang J, Su X, Mason RP. In Vitro and In Vivo Assessment of CdTe and CdHgTe Toxicity and Clearance. Journal of Biomedical Nanotechnology. 2008 Dec;4(4):524-8.

[13] Choi JH, Nguyen FT, Barone PW, Heller DA, Moll AE, Patel D, et al. Multimodal biomedical imaging with asymmetric single-walled carbon nanotube/iron oxide nanoparticle complexes. Nano letters. 2007 Apr;7(4):861-7.

[14] Raghavan D, Koczwara B, Javle M. Evolving strategies of cytotoxic chemotherapy for advanced prostate cancer. Eur J Cancer. 1997 Apr;33(4):566-74.

[15] Bharali DJ, Mousa SA. Emerging nanomedicines for early cancer detection and improved treatment: current perspective and future promise. Pharmacology & therapeutics. 2010 Nov;128(2):324-35.

[16] Xie J, Lee S, Chen X. Nanoparticle-based theranostic agents. Advanced Drug Delivery Reviews. 2010;62(11):1064-79.

[17] Bardhan R, Lal S, Joshi A, Halas NJ. Theranostic nanoshells: from probe design to imaging and treatment of cancer. Acc Chem Res. 2011 Oct 18;44(10):936-46.

[18] Babincova M, Babinec P. Magnetic drug delivery and targeting: principles and applications. Biomed Pap Med Fac Univ Palacky Olomouc Czech Repub. 2009 Dec;153(4):243-50.

[19] Bonnemain B. Superparamagnetic agents in magnetic resonance imaging: physicochemical characteristics and clinical applications. A review. Journal of drug targeting. 1998;6(3):167-74.

[20] Mornet S, Vasseur S, Grasset F, Duguet E. Magnetic nanoparticle design for medical diagnosis and therapy. Journal of Materials Chemistry. 2004;14(14):2161-75.

[21] Shubayev VI, Pisanic TR, 2nd, Jin S. Magnetic nanoparticles for theragnostics. Advanced drug delivery reviews. 2009 Jun 21;61(6):467-77.

[22] Strijkers GJ, Kluza E, Van Tilborg GA, van der Schaft DW, Griffioen AW, Mulder WJ, et al. Paramagnetic and fluorescent liposomes for target-specific imaging and therapy of tumor angiogenesis. Angiogenesis. 2010 Jun;13(2):161-73.

[23] Gupta AK, Wells S. Surface-modified superparamagnetic nanoparticles for drug delivery: preparation, characterization, and cytotoxicity studies. IEEE transactions on nanobioscience. 2004 Mar;3(1):66-73.

[24] Tassa C, Shaw SY, Weissleder R. Dextran-coated iron oxide nanoparticles: a versatile platform for targeted molecular imaging, molecular diagnostics, and therapy. Acc Chem Res. 2011 Oct 18;44(10):842-52.

[25] Tassa C, Shaw SY, Weissleder R. Dextran-Coated Iron Oxide Nanoparticles: A Versatile Platform for Targeted Molecular Imaging, Molecular Diagnostics, and Therapy. Accounts of Chemical Research. 2011 06/10
2012/05/01;44(10):842-52.

[26] Arami H, Stephen Z, Veiseh O, Zhang M. Chitosan-coated iron oxide nanoparticles for molecular imaging and drug delivery. *Advances in Polymer Science*: Springer Berlin / Heidelberg 2011:163-84.

[27] Schmid G. Syntheses and Characterizations. *Nanoparticles: From Theory to Application*. 2nd ed: Wiley-VCH 2010:284-5.

[28] Chattopadhyay P, Gupta RB. Supercritical CO2 based production of magnetically responsive micro- and nanoparticles for drug targeting. Ind Eng Chem Res. 2002 Oct 25;41(24):6049-58.

[29] Rahimi M, Meletis EI, You S, Nguyen K. Formulation and characterization of novel temperature sensitive polymer-coated magnetic nanoparticles. J Nanosci Nanotechnol. 2010 Sep;10(9):6072-81.

[30] Kumar A, Srivastava A, Galaev IY, Mattiasson B. Smart polymers: physical forms and bioengineering applications. Progress in Polymer Science. 2007;32(10):1205-37.

[31] Wadajkar A, Koppolu B, Rahimi M, Nguyen K. Cytotoxic evaluation of N-isopropylacrylamide monomers and temperature-sensitive poly(N-isopropylacrylamide) nanoparticles. Journal of Nanoparticle Research. 2009;11(6):1375-82.

[32] Hoffman AS, Stayton PS, Bulmus V, Chen G, Chen J, Cheung C, et al. Really smart bioconjugates of smart polymers and receptor proteins. J Biomed Mater Res. 2000;52(4):577-86.

[33] Yuan Q, Venkatasubramanian R, Hein S, Misra RDK. A stimulus-responsive magnetic nanoparticle drug carrier: Magnetite encapsulated by chitosan-grafted-copolymer. Acta Biomaterialia. 2008;4(4):1024-37.

[34] Fan L, Wu H, Zhang H, Li F, Yang T-h, Gu C-h, et al. Novel super pH-sensitive nanoparticles responsive to tumor extracellular pH. Carbohydrate Polymers. 2008;73(3):390-400.

[35] Kamaly N, Miller AD. Paramagnetic liposome nanoparticles for cellular and tumour imaging. Int J Mol Sci. 2010;11(4):1759-76.

[36] Namiki Y, Fuchigami T, Tada N, Kawamura R, Matsunuma S, Kitamoto Y, et al. Nanomedicine for cancer: lipid-based nanostructures for drug delivery and monitoring. Acc Chem Res. 2011 Oct 18;44(10):1080-93.

[37] Li X, Li H, Liu G, Deng Z, Wu S, Li P, et al. Magnetite-loaded fluorine-containing polymeric micelles for magnetic resonance imaging and drug delivery. Biomaterials. 2012;33(10):3013-24.

[38] Tada DB, Vono LL, Duarte EL, Itri R, Kiyohara PK, Baptista MS, et al. Methylene blue-containing silica-coated magnetic particles: a potential magnetic carrier for photodynamic therapy. Langmuir. 2007 Jul 17;23(15):8194-9.

[39] Yu F, Yang VC. Size-tunable synthesis of stable superparamagnetic iron oxide nanoparticles for potential biomedical applications. Journal of biomedical materials research. 2010 Mar 15;92(4):1468-75.

[40] Sun C, Lee JS, Zhang M. Magnetic nanoparticles in MR imaging and drug delivery. Adv Drug Deliv Rev. 2008 Aug 17;60(11):1252-65.

[41] Nath S, Kaittanis C, Ramachandran V, Dalal N, Perez JM. Synthesis, magnetic characterization and sensing applications of novel dextran-coated iron oxide nanorods. Chem Mater. 2009 Apr 28;21(8):1761-7.

[42] Reddy AM, Kwak BK, Shim HJ, Ahn C, Lee HS, Suh YJ, et al. In vivo tracking of mesenchymal stem cells labeled with a novel chitosan-coated superparamagnetic iron oxide nanoparticles using 3.0T MRI. J Korean Med Sci. 2010 Feb;25(2):211-9.

[43] Okassa LN, Marchais H, Douziech-Eyrolles L, Hervé K, Cohen-Jonathan S, Munnier E, et al. Optimization of iron oxide nanoparticles encapsulation within poly(d,l-lactide-co-glycolide) sub-micron particles. Eur J Pharm Biopharm. 2007 Aug;67(1):31-8.

[44] Rahimi M, Wadajkar A, Subramanian K, Yousef M, Cui W, Hsieh JT, et al. In vitro evaluation of novel polymer-coated magnetic nanoparticles for controlled drug delivery. Nanomedicine. 2010 Oct;6(5):672-80.

[45] Flesch C, Unterfinger Y, Bourgeat-Lami E, Duguet E, Delaite C, Dumas P. Poly(ethylene glycol) surface coated magnetic particles. Macromolecular Rapid Communications. 2005;26:1494–8.

[46] Wang C, Xu C, Zeng H, Sun S. Recent Progress in Syntheses and Applications of Dumbbell-like Nanoparticles. Adv Mater. 2009;21(30):3045-52.

[47] Bertorelle F, Wilhelm C, Roger J, Gazeau F, Ménager C, Cabuil V. Fluorescence-modified superparamagnetic nanoparticles: intracellular uptake and use in cellular imaging. Langmuir. 2006 Jun 6;22(12):5385-91.

[48] Sun P, Zhang H, Liu C, Fang J, Wang M, Chen J, et al. Preparation and characterization of Fe3O4/CdTe magnetic/fluorescent nanocomposites and their applications in immuno-labeling and fluorescent imaging of cancer cells. Langmuir. 2010 Jun 19;26(2):1278-84.

[49] Jiang T, Zhang C, Zheng X, Xu X, Xie X, Liu H, et al. Noninvasively characterizing the different alphavbeta3 expression patterns in lung cancers with RGD-USPIO using a clinical 3.0T MR scanner. Int J Nanomedicine. 2009;4:241-9.

[50] Lopez-Colon D, Jimenez E, You M, Gulbakan B, Tan W. Aptamers: turning the spotlight on cells. Wiley interdisciplinary reviews. 2011 Mar 15.

[51] Nie S, Xing Y, Kim GJ, Simons JW. Nanotechnology applications in cancer. Annual review of biomedical engineering. 2007;9:257-88.

[52] Danhier F, Feron O, Préat V. To exploit the tumor microenvironment: Passive and active tumor targeting of nanocarriers for anti-cancer drug delivery. J Control Release. 2010 Dec 1;148(2):135-46.

[53] Maeda H, Wu J, Sawa T, Matsumura Y, Hori K. Tumor vascular permeability and the EPR effect in macromolecular therapeutics: a review. Journal of Controlled Release. 2000;65(1-2):271-84.

[54] Yu MK, Jeong YY, Park J, Park S, Kim JW, Min JJ, et al. Drug-Loaded Superparamagnetic Iron Oxide Nanoparticles for Combined Cancer Imaging and Therapy In Vivo. Angewandte Chemie International Edition. 2008;47(29):5362-5.

[55] Cao Z-g, Zhou S-w, Liu J-h. Effects of carboxymethly dextran magnetic nanoparticles carrier system associated with external magnetic fields on killing tumor cells and gene transfection. Chinese Journal of Cancer Research. 2005;17(1):1-5.

[56] Gao X, Cui Y, Levenson RM, Chung LWK, Nie S. In vivo cancer targeting and imaging with semiconductor quantum dots. Nat Biotech. 2004;22(8):969-76.

[57] Cho K, Wang X, Nie S, Chen ZG, Shin DM. Therapeutic nanoparticles for drug delivery in cancer. Clin Cancer Res. 2008 Mar 1;14(5):1310-6.

[58] Marcucci F, Lefoulon F. Active targeting with particulate drug carriers in tumor therapy: fundamentals and recent progress. Drug Discovery Today. 2004;9(5):219-28.

[59] Yao V, Berkman CE, Choi JK, O'Keefe DS, Bacich DJ. Expression of prostate-specific membrane antigen (PSMA), increases cell folate uptake and proliferation and suggests a novel role for PSMA in the uptake of the non-polyglutamated folate, folic acid. Prostate. 2010 Feb 15;70(3):305-16.

[60] Kievit FM, Stephen ZR, Veiseh O, Arami H, Wang T, Lai VP, et al. Targeting of Primary Breast Cancers and Metastases in a Transgenic Mouse Model Using Rationally Designed Multifunctional SPIONs. ACS Nano. 2012 02/10 2012/04/27;6(3):2591-601.

[61] Blanco E, Kessinger CW, Sumer BD, Gao J. Multifunctional micellar nanomedicine for cancer therapy. Experimental biology and medicine (Maywood, NJ. 2009 Feb;234(2):123-31.

[62] Alexiou C, Arnold W, Klein RJ, Parak FG, Hulin P, Bergemann C, et al. Locoregional cancer treatment with magnetic drug targeting. Cancer research. 2000 Dec 1;60(23):6641-8.

[63] Chertok B, Moffat BA, David AE, Yu F, Bergemann C, Ross BD, et al. Iron oxide nanoparticles as a drug delivery vehicle for MRI monitored magnetic targeting of brain tumors. Biomaterials. 2008;29(4):487-96.

[64] Sunshine JC, Akanda MI, Li D, Kozielski KL, Green JJ. Effects of base polymer hydrophobicity and end-group modification on polymeric gene delivery. Biomacromolecules. 2011 Oct 10;12(10):3592-600.

[65] Tzeng SY, Guerrero-Cázares H, Martinez EE, Sunshine JC, Quiñones-Hinojosa A, Green JJ. Non-viral gene delivery nanoparticles based on poly(β-amino esters) for treatment of glioblastoma. Biomaterials. 2011 Aug;32(23):5402-10.

[66] Lin MM, Kim HH, Kim H, Dobson J, Kim do K. Surface activation and targeting strategies of superparamagnetic iron oxide nanoparticles in cancer-oriented diagnosis and therapy. Nanomedicine (London, England). 2010 Jan;5(1):109-33.

[67] Wang YX. Superparamagnetic iron oxide based MRI contrast agents: current status of clinical application. Quant Imaging Med Surg. 2011;1(1):35-40.

[68] Bae KH, Lee K, Kim C, Park TG. Surface functionalized hollow manganese oxide nanoparticles for cancer targeted siRNA delivery and magnetic resonance imaging. Biomaterials. 2011 Jan;32(1):176-84.

[69] Ahren M, Selegard L, Klasson A, Soderlind F, Abrikossova N, Skoglund C, et al. Synthesis and characterization of PEGylated Gd2O3 nanoparticles for MRI contrast enhancement. Langmuir. 2010 Apr 20;26(8):5753-62.

[70] Vymazal J, Spuentrup E, Cardenas-Molina G, Wiethoff AJ, Hartmann MG, Caravan P, et al. Thrombus imaging with fibrin-specific gadolinium-based MR contrast agent EP-2104R: results of a phase II clinical study of feasibility. Invest Radiol. 2009 Nov;44(11):697-704.

[71] Schellenberger EA, Sosnovik D, Weissleder R, Josephson L. Magneto/optical annexin V, a multimodal protein. Bioconjug Chem. 2004 Sep-Oct;15(5):1062-7.

[72] Medintz IL, Uyeda HT, Goldman ER, Mattoussi H. Quantum dot bioconjugates for imaging, labelling and sensing. Nature materials. 2005 Jun;4(6):435-46.

[73] Erathodiyil N, Ying JY. Functionalization of inorganic nanoparticles for bioimaging applications. Accounts of chemical research. 2011 Oct 18;44(10):925-35.

[74] Fan HM, Olivo M, Shuter B, Yi JB, Bhuvaneswari R, Tan HR, et al. Quantum dot capped magnetite nanorings as high performance nanoprobe for multiphoton fluorescence and magnetic resonance imaging. Journal of the American Chemical Society. 2010 Oct 27;132(42):14803-11.

[75] Koole R, van Schooneveld MM, Hilhorst J, Castermans K, Cormode DP, Strijkers GJ, et al. Paramagnetic lipid-coated silica nanoparticles with a fluorescent quantum dot core: a new contrast agent platform for multimodality imaging. Bioconjugate chemistry. 2008 Dec;19(12):2471-9.

[76] Devaraj NK, Keliher EJ, Thurber GM, Nahrendorf M, Weissleder R. 18F labeled nanoparticles for in vivo PET-CT imaging. Bioconjugate chemistry. 2009 Feb;20(2):397-401.

[77] Dutz S, Kettering M, Hilger I, Muller R, Zeisberger M. Magnetic multicore nanoparticles for hyperthermia--influence of particle immobilization in tumour tissue on magnetic properties. Nanotechnology. 2011 Jul 1;22(26):265102.

[78] Dobson J. Gene therapy progress and prospects: magnetic nanoparticle-based gene delivery. Gene Ther. 2006 Feb;13(4):283-7.

[79] Erten A, Wrasidlo W, Scadeng M, Esener S, Hoffman RM, Bouvet M, et al. Magnetic resonance and fluorescence imaging of doxorubicin-loaded nanoparticles using a novel in vivo model. Nanomedicine. 2010 Dec;6(6):797-807.

[80] McBain SC, Yiu HH, Dobson J. Magnetic nanoparticles for gene and drug delivery. Int J Nanomedicine. 2008;3(2):169-80.

[81] Tietze R, Schreiber E, Lyer S, Alexiou C. Mitoxantrone loaded superparamagnetic nanoparticles for drug targeting: a versatile and sensitive method for quantification of drug enrichment in rabbit tissues using HPLC-UV. J Biomed Biotechnol. 2010;2010:1-8.

[82] Nowicka AM, Kowalczyk A, Donten M, Krysinski P, Stojek Z. Influence of a magnetic nanoparticle as a drug carrier on the activity of anticancer drugs: Interactions of double stranded DNA and doxorubicin modified with a carrier. Analytical Chemistry. 2009 2012/02/03;81(17):7474-83.

[83] Xiang SD, Selomulya C, Ho J, Apostolopoulos V, Plebanski M. Delivery of DNA vaccines: an overview on the use of biodegradable polymeric and magnetic nanoparticles. Wiley Interdisciplinary Reviews: Nanomedicine and Nanobiotechnology. 2010;2(3):205-18.

[84] Mykhaylyk O, Sobisch T, Almstätter I, Sanchez-Antequera Y, Brandt S, Anton M, et al. Silica-iron oxide magnetic nanoparticles modified for gene delivery: A search for optimum and quantitative criteria. Pharm Res. 2012:1-22.

[85] Chertok B, David AE, Yang VC. Magnetically-enabled and MR-monitored selective brain tumor protein delivery in rats via magnetic nanocarriers. Biomaterials. 2011 Sept;32(26):6245-53.

[86] Tung CH, Mahmood U, Bredow S, Weissleder R. In vivo imaging of proteolytic enzyme activity using a novel molecular reporter. Cancer Res. 2000 Sep 1;60(17):4953-8.

[87] Gupta P, Vermani K, Garg S. Hydrogels: from controlled release to pH-responsive drug delivery. Drug Discov Today. 2002 May 15;7(10):569-79.

[88] Ito A, Shinkai M, Honda H, Kobayashi T. Medical application of functionalized magnetic nanoparticles. J Biosci Bioeng. 2005 Jul;100(1):1-11.

[89] Branca RT, Cleveland ZI, Fubara B, Kumar CS, Maronpot RR, Leuschner C, et al. Molecular MRI for sensitive and specific detection of lung metastases. Proceedings of the National Academy of Sciences of the United States of America. 2010 Feb 23;107(8):3693-7.

[90] Harisinghani MG, Barentsz J, Hahn PF, Deserno WM, Tabatabaei S, van de Kaa CH, et al. Noninvasive Detection of Clinically Occult Lymph-Node Metastases in Prostate Cancer. New England Journal of Medicine. 2003;348(25):2491-9.

[91] Widder KJ, Senyei AE, Ranney DF. In vitro release of biologically active adriamycin by magnetically responsive albumin microspheres. Cancer research. 1980 Oct;40(10):3512-7.

[92] Berry CC, Curtis ASG. Functionalisation of magnetic nanoparticles for applications in biomedicine. J Phys D: Appl Phys. 2003;36(13).

[93] Chen Y, Chen BA. Application and advancement of magnetic iron-oxide nanoparticles in tumor-targeted therapy. Chinese journal of cancer. 2010 Jan;29(1):125-8.

[94] Jordan A, Wust P, Fähling H, John W, Hinz A, Felix R. Inductive heating of ferrimagnetic particles and magnetic fluids: physical evaluation of their potential for hyperthermia. Int J Hyperthermia. 1993 Jan-Feb;9(1):51-68.

[95] Le Renard PE, Jordan O, Faes A, Petri-Fink A, Hofmann H, Rufenacht D, et al. The in vivo performance of magnetic particle-loaded injectable, in situ gelling, carriers for the delivery of local hyperthermia. Biomaterials. 2010 Feb;31(4):691-705.

[96] Tseng HY, Lee GB, Lee CY, Shih YH, Lin XZ. Localised heating of tumours utilising injectable magnetic nanoparticles for hyperthermia cancer therapy. IET Nanobiotechnol. 2009 Jun;3(2):46-54.

[97] Wang ZY, Song J, Zhang DS. Nanosized As2O3/Fe2O3 complexes combined with magnetic fluid hyperthermia selectively target liver cancer cells. World J Gastroenterol. 2009 Jun 28;15(24):2995-3002.

[98] Du Y, Zhang D, Liu H, Lai R. Thermochemotherapy effect of nanosized As2O3/Fe3O4 complex on experimental mouse tumors and its influence on the expression of CD44v6, VEGF-C and MMP-9. BMC Biotechnol. 2009;9:84.

[99] Puech P, Huglo D, Petyt G, Lemaitre L, Villers A. Imaging of organ-confined prostate cancer: functional ultrasound, MRI and PET/computed tomography. Curr Opin Urol. 2009 Mar;19(2):168-76.

[100] Brannon-Peppas L, Blanchette JO. Nanoparticle and targeted systems for cancer therapy. Adv Drug Deliv Rev. 2004 Sep 22;56(11):1649-59.

[101] Yang J, Zhang Y, Gautam S, Liu L, Dey J, Chen W, et al. Development of aliphatic biodegradable photoluminescent polymers. Proc Natl Acad Sci U S A. 2009 Jun 23;106(25):10086-91.

[102] Schmieder AH, Caruthers SD, Zhang H, Williams TA, Robertson JD, Wickline SA, et al. Three-dimensional MR mapping of angiogenesis with alpha5beta1(alpha nu beta3)-targeted theranostic nanoparticles in the MDA-MB-435 xenograft mouse model. FASEB J. 2008 Dec;22(12):4179-89.

[103] Santra S, Kaittanis C, Grimm J, Perez JM. Drug/dye-loaded, multifunctional iron oxide nanoparticles for combined targeted cancer therapy and dual optical/magnetic resonance imaging. Small. 2009 Aug 17;5(16):1862-8.

[104] Gu H, Zheng R, Zhang X, Xu B. Facile one-pot synthesis of bifunctional heterodimers of nanoparticles: a conjugate of quantum dot and magnetic nanoparticles. J Am Chem Soc. 2004 May 12;126(18):5664-5.

[105] Veiseh O, Sun C, Fang C, Bhattarai N, Gunn J, Kievit F, et al. Specific targeting of brain tumors with an optical/magnetic resonance imaging nanoprobe across the blood-brain barrier. Cancer Res. 2009 Aug 1;69(15):6200-7.

[106] Choi HS, Liu W, Liu F, Nasr K, Misra P, Bawendi MG, et al. Design considerations for tumour-targeted nanoparticles. Nat Nanotechnol. 2010 Jan;5(1):42-7.

[107] Rahimi M, Yousef M, Cheng Y, Meletis EI, Eberhart RC, Nguyen K. Formulation and characterization of a covalently coated magnetic nanogel. Journal of nanoscience and nanotechnology. 2009 Jul;9(7):4128-34.

[108] Gupta AK, Gupta M. Cytotoxicity suppression and cellular uptake enhancement of surface modified magnetic nanoparticles. Biomaterials. 2005 May;26(13):1565-73.

[109] Nam HY, Kwon SM, Chung H, Lee SY, Kwon SH, Jeon H, et al. Cellular uptake mechanism and intracellular fate of hydrophobically modified glycol chitosan nanoparticles. J Control Release. 2009 May 5;135(3):259-67.

[110] Michael A, Syrigos K, Pandha H. Prostate cancer chemotherapy in the era of targeted therapy. Prostate cancer and prostatic diseases. 2009;12(1):13-6.

[111] Koneracka M, Zavisova V, Timko M, Kopcansky P, Tomasovicova N, Csach K. Magnetic Properties of Encapsulated Magnetite in PLGA Nanospheres. Acta Physica Polonica A. 2008;113(1):595-8.

[112] Lin JJ, Chen JS, Huang SJ, Ko JH, Wang YM, Chen TL, et al. Folic acid-Pluronic F127 magnetic nanoparticle clusters for combined targeting, diagnosis, and therapy applications. Biomaterials. 2009 Oct;30(28):5114-24.

[113] Bumb A, Regino CA, Egen JG, Bernardo M, Dobson PJ, Germain RN, et al. Trafficking of a dual-modality magnetic resonance and fluorescence imaging superparamagnetic iron oxide-based nanoprobe to lymph nodes. Mol Imaging Biol. 2011 Dec;13(6):1163-72.

[114] Chen ZP, Zhang Y, Xu K, Xu RZ, Liu JW, Gu N. Stability of hydrophilic magnetic nanoparticles under biologically relevant conditions. Journal of nanoscience and nanotechnology. 2008 Dec;8(12):6260-5.

[115] He X, Wang K, Tan W, Liu B, Lin X, Huang S, et al. A novel gene carrier based on amino-modified silica nanoparticles. Chinese Science Bulletin. 2003;48(3):223-8.

[116] Ramirez LP, Landfester K. Magnetic polystyrene nanoparticles with a high magnetite content obtained by miniemulsion processes. Macromolecular Chemistry and Physics. 2003;204(1):22-31.

[117] Pouponneau P, Leroux J, Martel S. Magnetic nanoparticles encapsulated into biodegradable microparticles steered with an upgraded magnetic resonance imaging system for tumor chemoembolization. Biomaterials. 2009;30:6327-32.

[118] Bao H, Chen Z, Lin K, Wu P, Liu J. Preparation of magnetic nanoparticles modified by amphiphilic copolymers. Materials Letters. 2006;60:2167-70.

[119] Pinkernelle J, Teichgräber U, Neumann F, Lehmkuhl L, Ricke J, Scholz R, et al. Imaging of single human carcinoma cells in vitro using a clinical whole-body magnetic resonance scanner at 3.0 T. Magn Reson Med. 2005;53(5):1187-92.

[120] Gao X, Cui Y, Levenson RM, Chung LW, Nie S. In vivo cancer targeting and imaging with semiconductor quantum dots. Nat Biotechnol. 2004 Aug;22(8):969-76.

[121] Liu L, Zhang J, Su X, Mason RP. In vitro and In vivo Assessment of CdTe and CdHgTe Toxicity and Clearance. J Biomed Nanotechnol. 2008 Dec 1;4(4):524-8.

[122] Ferrati S, Mack A, Chiappini C, Liu X, Bean AJ, Ferrari M, et al. Intracellular trafficking of silicon particles and logic-embedded vectors. Nanoscale. 2010 Aug;2(8):1512-20.

[123] Villanueva A, Canete M, Roca AG, Calero M, Veintemillas-Verdaguer S, Serna CJ, et al. The influence of surface functionalization on the enhanced internalization of magnetic nanoparticles in cancer cells. Nanotechnology. 2009 Mar 18;20(11):115103.

[124] Shen S, Liu Y, Huang P, Wang J. In vitro cellular uptake and effects of Fe3O4 magnetic nanoparticles on HeLa cells. Journal of nanoscience and nanotechnology. 2009 May;9(5):2866-71.

[125] Pulukuri SM, Gondi CS, Lakka SS, Jutla A, Estes N, Gujrati M, et al. RNA interference-directed knockdown of urokinase plasminogen activator and urokinase plasminogen activator receptor inhibits prostate cancer cell invasion, survival, and tumorigenicity in vivo. J Biol Chem. 2005 Oct 28;280(43):36529-40.

[126] Gaumet M, Gurny R, Delie F. Interaction of biodegradable nanoparticles with intestinal cells: the effect of surface hydrophilicity. Int J Pharm. 2010 May 5;390(1):45-52.

[127] Narain R, Gonzales M, Hoffman AS, Stayton PS, Krishnan KM. Synthesis of monodisperse biotinylated p(NIPAAm)-coated iron oxide magnetic nanoparticles and their bioconjugation to streptavidin. Langmuir. 2007 May 22;23(11):6299-304.

[128] Graf N, Bielenberg DR, Kolishetti N, Muus C, Banyard J, Farokhzad OC, et al. alpha(V)beta(3) Integrin-Targeted PLGA-PEG Nanoparticles for Enhanced Anti-tumor Efficacy of a Pt(IV) Prodrug. ACS nano. 2012 May 22;6(5):4530-9.

[129] Zhao D, Zhao X, Zu Y, Li J, Zhang Y, Jiang R, et al. Preparation, characterization, and in vitro targeted delivery of folate-decorated paclitaxel-loaded bovine serum albumin nanoparticles. Int J Nanomedicine. 2010;5:669-77.

[130] Hsieh JT, Zhou J, Gore C, Zimmern P. R11, a novel cell-permeable peptide, as an intravesical delivery vehicle. BJU Int. 2011 Nov;108(10):1666-71.

[131] Bucci M, Gratton JP, Rudic RD, Acevedo L, Roviezzo F, Cirino G, et al. In vivo delivery of the caveolin-1 scaffolding domain inhibits nitric oxide synthesis and reduces inflammation. Nature medicine. 2000 Dec;6(12):1362-7.

[132] Rothbard JB, Jessop TC, Lewis RS, Murray BA, Wender PA. Role of membrane potential and hydrogen bonding in the mechanism of translocation of guanidinium-rich peptides into cells. Journal of the American Chemical Society. 2004 Aug 11;126(31):9506-7.

[133] Zhou J, Fan J, Hsieh JT. Inhibition of mitogen-elicited signal transduction and growth in prostate cancer with a small peptide derived from the functional domain of DOC-2/DAB2 delivered by a unique vehicle. Cancer research. 2006 Sep 15;66(18):8954-8.

[134] Rahimi M, Kilaru S, Sleiman GE, Saleh A, Rudkevich D, Nguyen K. Synthesis and Characterization of Thermo-Sensitive Nanoparticles for Drug Delivery Applications. J Biomed Nanotechnol. 2008 Dec 1;4(4):482-90.

[135] Fornari FA, Randolph JK, Yalowich JC, Ritke MK, Gewirtz DA. Interference by doxorubicin with DNA unwinding in MCF-7 breast tumor cells. Molecular pharmacology. 1994 Apr;45(4):649-56.

[136] Dromi S, Frenkel V, Luk A, Traughber B, Angstadt M, Bur M, et al. Pulsed-high intensity focused ultrasound and low temperature-sensitive liposomes for enhanced targeted drug delivery and antitumor effect. Clin Cancer Res. 2007 May 1;13(9):2722-7.

[137] Wu T, Hua MY, Chen JP, Wei KC, Jung SM, Chang YJ, et al. Effects of external magnetic field on biodistribution of nanoparticles: A histological study. Journal of Magnetism and Magnetic Materials. 2007 Apr;311(1):372-75.

[138] Hao G, Zhou J, Guo Y, Long MA, Anthony T, Stanfield J, et al. A cell permeable peptide analog as a potential-specific PET imaging probe for prostate cancer detection. Amino Acids. 2011 Nov;41(5):1093-101.

[139] Lim YT, Noh YW, Han JH, Cai QY, Yoon KH, Chung BH. Biocompatible polymer-nanoparticle-based bimodal imaging contrast agents for the labeling and tracking of dendritic cells. Small. 2008;4(10):1640-5.

[140] Liu TY, Huang TC. A novel drug vehicle capable of ultrasound-triggered release with MRI functions. Acta biomaterialia. 2011 Nov;7(11):3927-34.

BIOGRAPHICAL INFORMATION

Aniket Wadajkar grew up in a small town of Kandhar in Maharashtra, India. After his high school education, he pursued a bachelor's degree in Instrumentation and Control Engineering from the University of Pune. Driven by his career interests in research, he kicked off his research in nanoparticle development at the University of Pune. To explore this field more, he joined a Master of Science program in Biomedical Engineering at the University of Texas at Arlington. Under the guidance of Dr. Kytai T. Nguyen, he worked on nanoparticle and hydrogel-based drug delivery systems. After graduating with a master's degree in 2008, Aniket worked as a Research Scientist at Antibody Research Corp. in St. Louis, MO, where his work focused on antibody production and purification. Determined to pursue a Doctor of Philosophy, he went back to his alma mater in August 2009 and continued his research on the development of magnetic-based theranostic nanoparticles for prostate cancer management. He is a recipient of prestigious 'American Heart Association Predoctoral Fellowship', 'Who's Who among American Universities and Colleges award', and 'Alfred R. and Janet H. Potvin Outstanding Bioengineering Student award' to name a few. He has authored over 20 journal papers, 2 book chapters, and a patent application. He also played an active role in keeping the BMES student chapter vibrant at UTA. Aniket's research interest involves nanomaterials, drug delivery, and cell-material interactions. After graduation, he intends to pursue a career in academia as an independent researcher.